

Numerical Simulation of Flow-Induced Noise by Means of the Hybrid Method with LES and Aeroacoustic Analogy

Dissertation
zur Erlangung des akademischen Grades
DOKTOR-INGENIEUR

vorgelegt von
M.Sc. **Kefan Tang**
aus Shanghai

eingereicht dem
**Fachbereich Maschinentechnik
der Universität Siegen**

Referent: Univ.-Prof. Dr.-Ing. habil. W. Frank
Korreferent: Univ.-Prof. Dr.-Ing. Th. Carolus

Tag der mündlichen Prüfung
22. Juli 2004

urn:nbn:de:hbz:467-783

Acknowledgement

I would like to express my gratitude to the people who contributed over the last five years in making this work a success. Firstly, Prof. Dr.-Ing. habil. Wolfram Frank, my “Doktorvater”, who gave me the opportunity to finish this work in his Institute with his full support, from the financial and technical resources to the motivational and methodological guidance. Beside Prof. Frank, Dr.-Ing. Jörg Franke provided me with many useful comments and acted as a direct guide along the path of knowledge of numerical fluid mechanics. I am also very grateful to Prof. Dr.-Ing. Thomas Carolus for his advice, support and encouragement, and his acceptance as the co-referee. Many thanks should go to the previous and present colleagues at the Institute of Fluid- and Thermal Dynamics of the University of Siegen, Dr.-Ing. Johannes Alken, Dr.-Ing. Gabor Janiga, and Dipl.-Phys. Ing. Hermann Geppert for their friendly help. I would like to acknowledge the DAAD (German Academic Exchange Service) for their financial support at the beginning of this work. I thank Dr. Richard Harvey for his careful correction in the English language. I should thank my family which, in spite of the long distance between Germany and China, always encouraged me. Special gratitude goes to my wife, Xiang Wang; without her love and support, none of this would have been possible.

Zusammenfassung

Das Thema der vorliegenden Arbeit ist die Entwicklung von Berechnungswerkzeugen zur Vorhersage strömungsinduzierten Lärms. Aufgrund des großen Unterschieds zwischen den akustischen und hydrodynamischen Längenskalen, sowie den Energien bei Strömungen geringer MACH Zahlen, ist ein hybrider Ansatz die einzige Möglichkeit zur Simulation praktischer Probleme. Bei dem hybriden Ansatz wird das gesamte Problem in zwei oder mehrere Teilprobleme zerlegt, wobei mit einer Methode die nichtlineare Schallerzeugung und mit einer oder mehreren anderen Methoden die Schallabstrahlung berechnet wird. Der in dieser Arbeit untersuchte hybride Ansatz verwendet zur Berechnung des akustischen Fernfeldes zwei Schritte.

Im ersten Schritt wird das zeitabhängige, kompressible Strömungsfeld in einem Simulationsgebiet berechnet, welches die akustischen Quellterme beinhaltet. Für den untersuchten laminaren Strömungsfall werden dazu direkt die NAVIER-STOKES Gleichungen gelöst, während der turbulente Fall mit Hilfe einer Grobstruktursimulation auf Basis der räumlich gefilterten NAVIER-STOKES Gleichungen unter Verwendung eines Feinstrukturmodelles berechnet wird. In beiden Fällen werden die zur Bestimmung der akustischen Quellen erforderlichen Zeitreihen von Strömungsgrößen abgespeichert. Diese Informationen werden dann im zweiten Schritt des hybriden Verfahrens genutzt, um den Schalldruck im Fernfeld zu berechnen. Zu diesem Zweck wurden mehrere Programme erstellt, mit denen die Schallabstrahlung aus dem dynamischen Nahfeld in das akustische Fernfeld berechnet werden kann.

Die Programme basieren auf der von FLOWCS-WILLIAMS und HAWKINGS formulierten akustischen Analogie für durchströmte Kontrollflächen. Diese wurde in drei unterschiedlichen integralen Formulierungen implementiert. Zum einen in der 3D Formulierung von FARASSAT, zum anderen in der 2D Formulierung von GUO sowie der 2D Formulierung von LOCARD. Durch den Vergleich der aufwändigeren 3D Formulierung mit den 2D Formulierungen konnte nachgewiesen werden, daß die 2D Formulierungen eine effiziente Methode darstellen.

Die numerischen Parameter der erstellten Programme sind die Position der Kontrollfläche, die Kopierlänge der Kontrollfläche bei der 3D Formulierung, die räumliche und zeitliche Auflösung, sowie die verwendeten Approximationen zur zeitlichen Interpolation, zeitlichen Ableitung und räumlichen Integration. Diese Parameter wurden in dieser Arbeit ausführlich untersucht, um eine optimale Kombination zu finden. Dazu wurde eine Verifikation anhand mehrerer analytischer Lösungen durchgeführt. Die so verifizierten Programme wurden dann durch den Vergleich mit den Ergebnissen einer direkten akustischen Simulation der laminaren Umströmung eines Zylinders bei $Re_D = 150$, $Ma = 0.2$ von INOUE validiert. Alle verwendeten Formulierungen der akustischen Analogie liefern eine sehr gute bereinstimmung mit dem direkt berechneten akustischen Fernfeld von INOUE. Der so validierte hybride Ansatz wurde dann für die Grobstruktursimulation der turbulenten Umströmung eines Zylinders bei $Re_D = 3900$, $Ma = 0.2$ verwendet. Die berechneten Ergebnisse des Schalldruckes im Fernfeld wurden mit den experimentellen Ergebnissen von NORBERG und SZEPESSY verglichen. Auch hier zeigte sich eine gute Übereinstimmung für alle Formulierungen. Nach diesen Ergebnissen kann aus der Grobstruktursimulation einer turbulenten Strömung mit Periodizität in Spannweitenrichtung das akustische Fernfeld mit Hilfe einer 2D Formulierung der akustischen Analogie sehr effizient und ausreichend genau berechnet werden.

Summary

This work is written for the development of computational tools to predict flow-induced noise. Due to the large disparity in acoustic and hydrodynamic length scale, as well as energy levels in low MACH number flows, the aeroacoustic simulation for practical applications can only be carried out with the hybrid approach, which separates the problem into two or more parts, one describing the nonlinear generation of sound, the others describing the transmission of sound. The hybrid approach investigated in this work simulates the acoustic far-field using a two step procedure.

In the first step, the unsteady compressible flow field is computed in a computational domain comprising the acoustic sources under consideration via a compressible NAVIER-STOKES solver for the laminar flow case, and a large eddy simulation (LES) solver for the turbulent case. The time-dependent quantities of acoustic source information required in the second step are stored in a data base. In the second step, a post-processing computer program is used to extend the dynamic near-field to the acoustic far-field, namely to calculate the far-field sound pressure based on the acoustic source information provided by the first step simulation.

The FLOWCS-WILLIAMS and HAWKINGS (FW-H) approach with a permeable (porous) control surface is chosen to carry out the second step. Three integral formulations of the FW-H approach, namely the 3D FARASSAT, 2D GUO and 2D LOCARD formulations, are implemented into the computer program. Through the comparisons among the results of the 3D and 2D formulations of the FW-H approach, the 2D approaches are suggested be an efficient way to guide and augment full 3D calculations.

The computational parameters for the aeroacoustic simulations, such as the position of the control surface, copy length in the span direction of the cylindrical control surface, spatial and temporal resolutions, and accuracies of numerical interpolation, derivation and integration, are investigated in this work to obtain an optimization concept of the numerical calculation. The capacity of the computer program used in this work is investigated in detail with verification and validation examples. The verification examples are based on several analytical solutions. The simulated acoustic far-field generated by an unsteady flow around a circular cylinder at $Re_D = 150$, $Ma = 0.2$ (the laminar flow case) is compared with the direct acoustic simulation (acoustic DNS) of INOUE, and that at $Re_D = 3900$, $Ma = 0.2$ (the turbulent flow case) is compared with the experimental results of NORBERG and SZEPESSY. Both the comparisons give a good agreement. The 2D approaches are proven to be very efficient and accurate enough for the application of LES with a periodical condition in the span direction.

Contents

Acknowledgement	I
Zusammenfassung	II
Summary	III
Nomenclature	VI
1 Introduction	1
1.1 Background and Motivation	1
1.2 Status Quo and Methodology	3
1.3 Scope of This Work	9
2 Governing Equations	12
2.1 Governing Equations for Near-field CFD	12
2.1.1 Compressible NS Equations	13
2.1.2 Spatially Filtered NS Equations	14
2.2 Governing Equations for Far-field CAA	17
2.2.1 Differential Formulation	17
2.2.2 3D Integral Formulations	22
2.2.3 2D Integral Formulations	27
3 Numerical Approaches	30
3.1 Near-field CFD	31
3.1.1 Space Discretization: Finite-Volume-Method	31
3.1.2 Temporal Discretization: Explicit RK-Method	34
3.1.3 Boundary Conditions	34
3.2 Far-field CAA	37
3.2.1 Coupling between CFD and Aeroacoustic Solver	37
3.2.2 3D Integral Extension	38
3.2.3 2D Integral Extension	45

4	Verification and Validation	49
4.1	Verifications with Analytical Solutions	50
4.1.1	3D Mono-, Di- and Quadrupole	50
4.1.2	2D Mono- and Dipole	59
4.1.3	Co-rotating Line Vortices	63
4.1.4	2D Monopole in Flow	65
4.2	Validation with DNS Results	66
4.2.1	General Features of DNS	67
4.2.2	Computational Parameters	68
4.2.3	Dynamical Near-field	72
4.2.4	Acoustic Far-field	75
5	Noise from Flow around Cylinder at $Re_D = 3900$	81
5.1	Computational Parameters	81
5.2	Dynamical Near-field	83
5.3	Acoustic Far-field	83
5.3.1	Intensity of Far-field Noise	84
5.3.2	Directivity of Far-field Noise	90
5.3.3	Frequency Spectrum of Far-field Noise	91
6	Conclusions and Outlook	96
	Bibliography	99
	Appendix	106
A	Analytical Solutions for the Verifications	106
A.1	Governing Equation	106
A.2	3D Mono-, Di- and Quadrupole	109
A.3	2D Mono- and Dipole	112
A.4	Co-rotating Line Vortices	114
A.5	2D Monopole in Flow	116

Nomenclature

Latin Symbols:

A	amplitudes
c_0	undisturbed sound speed
C_p	pressure coefficient
C_p, C_v	specific heats
C_L, C_D	lift coefficient, drag coefficient
d	distance, diameter
E	specific total energy
e	specific internal energy
f	frequency
G	GREEN 's function, filter function
H	Heaviside function
$H_k^{(n)}$	HANKEL function of nth kind and kth order
I	intensity
K	thermal conduction coefficient
k	wave number, specific kinetic energy
L	spatial length
L_z	spanwise length of CFD domain
L_c	copy length, spanwise length of CS after copying
l	length scale of turbulence
p	pressure
Q	source term
q	heat conduction
R	specific gas constant

r radius, distance
 S surface area
 S_{ij} strain tensor
 s entropy
 T period
 T_{ij} Lighthill Tensor
 t time
 u_i velocity of fluid medium
 u, v, w velocity components
 v_i velocity of CS
 x_i observation position
 x, y, z coordinates
 y_i source position

Greek Symbols:

α coefficient
 β PRANDTL coefficient
 Γ circulation
 γ specific heat ratio
 Δ difference
 δ DIRAC delta function, KRONECKER symbol
 ϵ error
 η KOLMOGOROV length scale
 η_i EULERIAN coordinates fixed to CS
 θ polar angle, temperature
 λ wave length
 μ viscosity
 ρ density

σ correlation length
 τ_{ij} viscous stress tensor
 ϕ potential function
 ω angular frequency

Calligraphical Symbols:

\mathcal{L} wave operator
 \mathcal{O} order of magnitude

Superscripts:

les large eddy scale
rms root mean square
sgs subgrid scale

Subscripts:

ana analytical
num numerical
rms root mean square
sgs subgrid scale

Fluid Dynamic Numbers:

M, Ma MACH number
Pr PRANDL number
Re REYNOLDS number
St STROUHAL number

Abbreviations:

BEM	Boundary Element Method
CS	Control Surface
CV	Control Volume
2D	Two Dimensional
3D	Three Dimensional
CFD	Computational Fluid Dynamics
CAA	Computational AeroAcoustics
DNS	Direct Numerical Simulation
FVM	Finite Volume Method
FW-H	FFOWCS-WILLIAMS and HAWKINGS
LEE	Linearized EULER Equations
LES	Large Eddy Simulation
NS	NAVIER-STOKES
RK	RUNGE-KUTTA
SPARC	Structured PArallel Research Code

Chapter 1

Introduction

1.1 Background and Motivation

Aeroacoustics has become a very important discipline within aeronautics. In the modern air transport industry, navigation vehicles have to be larger and faster to satisfy commercial demands. But the environmental impacts of such kinds of airplanes and helicopters have been under more and more rigorous international and national aviation regulations. The design of quieter aircraft has been an essential condition for the continuous growth of air transport in the future. New noise reduction concepts are incredibly important for the air transport industry under intense market competition. The NASA (National Aeronautics and Space Administration) of the USA has committed one-third of its resources in aeronautics into the discipline of aeroacoustics in the last decade.

In general, the noise sources of a typical civil transport aircraft can be cataloged into three different groups [18]:

Engine noise (generated directly by the engines)

Installation noise (the modification of engine noise due to airframe interference)

Airframe noise

A large part of the above three kinds of noise sources are generated aerodynamically, such as turbine jet noise, impulsive noise due to unsteady flow around wings and rotors, broadband noise due to inflow turbulence and boundary layer separated flow, etc. During landing and taking-off of an airplane, the airframe noise, which is induced aerodynamically, plays the major role in acoustic environmental impact. In particular, flaps, slats and landing gears can be identified as the major noise producing parts of the airframe.

In addition to the air transport industry, there are also many machines in other industries with significant aeroacoustic problems. For example, within the last 10 years, an enormous number of wind turbines have been installed in Europe to bring renewable wind

energy into public awareness. However, their further development is restricted mainly by visual impact and noise [80]. The noise regulations of various countries urge turbine manufacturers to reduce the aerodynamical noise emission of their turbines. As another example, the flows around the car windscreen-wiper and outer driving mirror have been recognized as main noise sources on a high-speed running car. The automobile industry has a great interest in reducing such kinds of noise to improve the comfort of car drivers [15].

It is more and more important for modern industries to use noise reduction concepts during the design process to make their products comply with noise regulations, and succeed in market competition. Noise reduction concepts, such as the geometrical shape optimization of the aircraft airframe or wind turbine blade, are based on an accurate prediction of the aeroacoustic noise. Both theoretical and experimental studies are being conducted to make such predictions. Flight-test or wind-tunnel simulation tests can be used, but, in either case, difficulties are encountered, such as high costs, safety risks, and atmospheric variables, as well as acoustic reflection problems for wind-tunnel tests. Therefore, numerical tools are being more and more employed for the prediction, and then control, of aerodynamical noise, with the help of rapidly increasing computational availability and the successful experiences of CFD (Computational Fluid Dynamics) in the last few decades.

In principle, CAA (Computational AeroAcoustics) problems have the same basic governing equations as CFD, namely the time-dependent, compressible NS (NAVIER-STOKES) equations. But usually aerodynamical problems are related to statistically averaged or even time independent characteristics, whereas aeroacoustical problems are absolutely time dependent and computationally much more costly for a numerical simulation. Moreover, there are still some particular difficulties with respect to CAA researches [12]:

- Much larger acoustic radiation field in comparison with the dynamical source region

- Much smaller acoustic energy in comparison with the dynamical energy of flow

- Possible false acoustic sources caused by numerical discretization errors

- Possible false acoustic reflections caused by numerical boundary conditions

Because of the complexity and difficulty of the CAA simulations, special computational issues and methods should be applied. There is still much work to do to make the achievement of CAA comparable with the tremendous successes of CFD in aerodynamics and aircraft design over the past 30 years. This work is written as a contribution to improve the numerical methods of aeroacoustic prediction, in order to meet the challenge posed by the above practical problems.

1.2 Status Quo and Methodology

Continuum fluid motions are governed by the NS equations. But with Direct Numerical Simulation (DNS) based on this equation system, the acoustical field induced by an unsteady flow field can be accurately calculated only for the cases with very limited REYNOLDS numbers with current technical ability. The practical aeroacoustic problems are usually posed at high REYNOLDS number beyond the current capability of DNS.

As discussed by SARKAR and HUSSAINI [73], assuming the computational domain to be 6 times the integral length scale of turbulence, the number of spatial grid points required to solve the three-dimensional isotropic turbulent flow field is:

$$N_1 = 216\alpha Re_t^{9/4} \quad (1.1)$$

where α is a $\mathcal{O}(1)$ coefficient, Re_t is a REYNOLDS number based on the integral length scale, l , of turbulence, which is related to the KOLMOGOROV length scale, η , of turbulence via $l/\eta = \mathcal{O}(Re_t^{3/4})$. And by a DNS of the flow field, the spatial resolution is supposed to be sufficient to resolve the turbulence structures down to the KOLMOGOROV length scale, η , of turbulence.

Moreover, an aeroacoustic DNS contains not only the sound generating turbulent near-field, but also the acoustic far-field. The dominant wavelength, λ_s , of the radiated sound can be estimated as $\mathcal{O}(l/M_t)$, where M_t is the turbulent MACH number. Assuming the computational domain to be 4 times the sound wave length, λ_s , the number of spatial grid points required for both the turbulent near-field and acoustic far-field is:

$$N_2 = 64\alpha M_t^{-3} Re_t^{9/4} \quad (1.2)$$

Obviously, for a subsonic turbulent flow, an aeroacoustic DNS requires many more spatial grid points than an aerodynamic DNS. The number of the spatial grid points increases with an M_t^{-3} factor. In other words, the computationally achievable Reynolds number decreases with an $M_t^{4/3}$ factor. For $M_t = 0.01$, which is representative of low-speed jets and boundary layers, the resolution of both flow and acoustics, rather than only the flow, leads to a decrease in Re_t by a factor of 0.004! For higher MACH numbers, the disparity of the acoustic and flow scales becomes smaller. For high-speed jets with $M_t = 0.3$, the reduction in Re_t with the direct approach is by a factor of 0.3.

Furthermore, as discussed by CRIGHTON [13], there are gross energy density disparities between the hydrodynamic near-field and acoustic far-field. For a subsonic flow, even when spherical spreading effects have been removed, the energies in the far field are much smaller than those in the flow itself, by a factor of $O(M^4)$, where M is the MACH number of the mean flow. It is highly possible that the numerical noise due to the resolved hydrodynamic fluctuations may swamp the acoustic signal completely.

In order to overcome the above difficulties of an aeroacoustic DNS and extend the computationally achievable Reynolds number to meet practical requirements, the hybrid simulation is introduced, with which the computational problem is divided into two or more parts, one describing the nonlinear generation of sound, the others describing the transmission of sound. This strategy of hybrid simulation is schematized in Fig. 1.1.

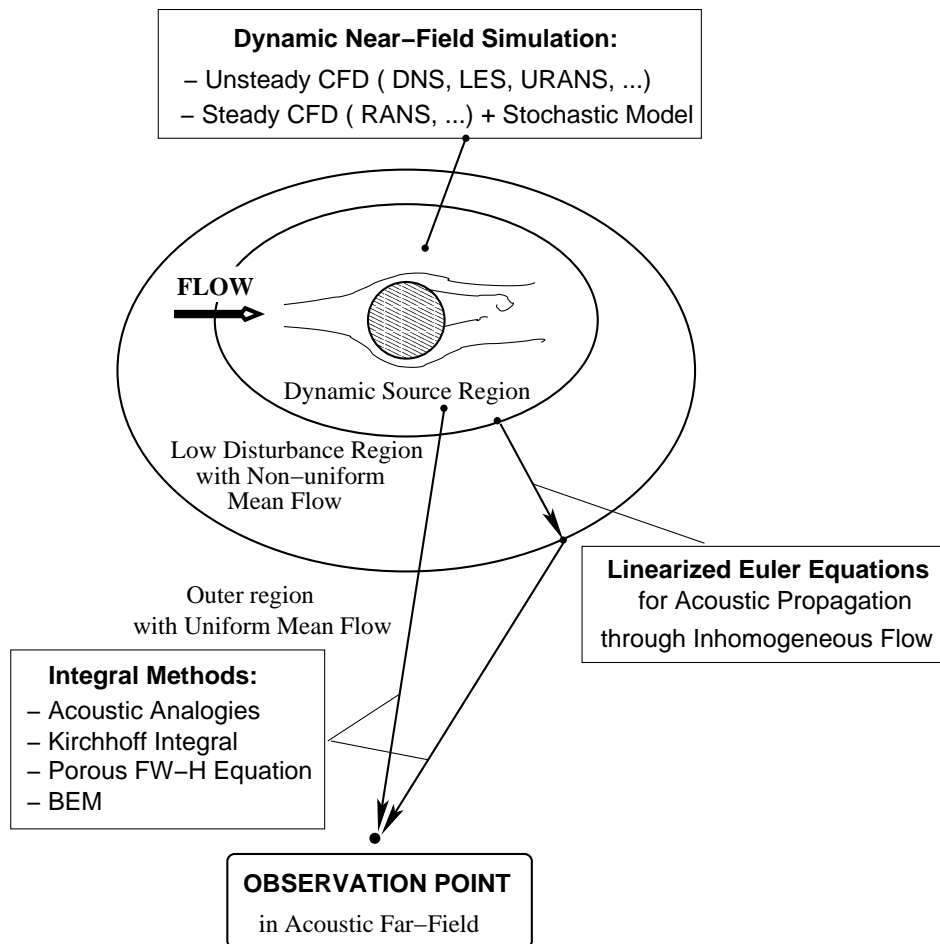


Figure 1.1: Methods of the Hybrid CFD/CAA Strategy

In Fig. 1.1, the alternatives for separating the computational domain are shown. There are three different regions shown in this scheme: dynamic source region, low disturbance region with non-uniform mean flow, and outer region with uniform mean flow. Through this separation, the NS equations have to be solved only in the relatively small dynamic source region. The dynamic source region is usually also called the dynamic near-field; CFD solvers are used in this region to calculate the source information of induced sound. In the other regions, CAA solvers are used to extend the near-field source information to the acoustic far-field.

The methods for extending the dynamic near-field to the acoustic far-field can now be described in two categories: integral methods (the acoustic analogies, Kirchhoff integral, porous FW-H equation and the boundary element methods (BEM)) and Linearized EULER Equations (LEE) methods (also called acoustic perturbation equation methods). The first category of integral methods have been developed for over 50 years, and successfully used to predict propeller and helicopter rotor noise [27, 21, 22, 9, 24], helicopter impulsive noise [8], airfoil noise [3, 2, 69], duct fan noise [68, 84] and jet noise [5, 7]. A comprehensive review of the integral methods has been concluded by LYRINTZIS [50]. The second category of LEE are newly emerged in CAA and have developed fast in recent years. A comprehensive review of the LEE methods has been given by TAM [75, 78] and LELE [44].

The approach of acoustic analogy was established by Lighthill. In his seminal papers of 1952 [46] and 1954 [47], he posed the problem of flow noise in terms of an inhomogeneous wave equation for a 'uniform medium at rest'. The actual flow was effectively incorporated into the right-side terms of the equation, which were interpreted as sources of sound. The source term on the right-side of the equation is a double divergence of the Lighthill stress defined as $T_{ij} = \rho u_i u_j + ((p - p_0) - c_0^2(\rho - \rho_0))\delta_{ij} - \tau_{ij}$. Through a dimensional analysis of his source term, Lighthill deduces the eighth-power law for the estimation of the sound power radiated from the turbulence. Although the famous Lighthill's equation is exact, approximations to solve these source terms with a free-space Green's function, referred to a stationary point source in a 'uniform medium at rest', have the effect of suppressing the interaction between the sound and inhomogeneous flow field (e.g. sound refraction and shielding in the inhomogeneous region).

The Lighthill analogy was followed by other acoustic analogies – Philips [61], Powell [65, 66], Lilley [48], Howe [34, 33], Moehring [57], etc. Of these, the Philips and Lilley analogy were posed to take account of the interaction between the sound and inhomogeneous flow field, and to identify the 'true' acoustic sources, by moving convection and refraction effects from the source term in the right-side of the equation to the wave operator terms in the left-side of the equation. The Powell, Howe and Moehring analogies are based on re-arrangements of Lighthill's source term into the form of an explicit dependence of vortex sound upon vorticity in flow. All the post-Lighthill analogies tried to identify the acoustic source terms more explicitly and purely, and thus predicted the acoustic far-field more accurately. Nevertheless, the majority of post-Lighthill analogies usually have complex wave operators, and thus have no, or a very complex, free space Green's function of the operator, so that the computational costs of these analogies are much higher than the original Lighthill analogy. The Lilley's equation received much attention and was developed into a quantitative predictive formalism for properties of jet noise, with the important flow-acoustic interaction effects: shielding, as well as the 'refractive cone of (relative) silence'. Nowadays, the flow-acoustic interaction effects can be well simulated by means of the LEE methods.

If the flow-acoustic interaction is important for the computational case, and the higher computational cost is not a problem, the LEE method is preferred rather than the LILLEY analogy.

As well as the turbulent jet, where the above acoustic analogies can be directly applied, the turbulent boundary of various engineering structures is another important noise source. CURLE [14] made an extension of Lighthill's analogy to incorporate the stationary solid boundary. The effects of the stationary solid boundary were posed as a distribution of monopolar sources on the boundary, representing the effect that the air, moving around the solid boundary volume, is displaced for a short period of time by the solid boundary volume and then moves back to its original position in the flow; and a distribution of dipolar sources on the boundary, representing the influence of the fluctuating forces acting from the solid boundary on the fluid. With Lighthill and Curle's theories as models, Ffowcs-Williams and Hawkings (FW-H) [82] introduced solid boundary effects as sound producers by considering the fluid dynamics around a moving closed control surface, with the concept of generalized functions. The Lighthill and Curle's theories were extended with the moving solid boundary effects through a Doppler factor $|1 - M_r|^{-1}$. After rewriting the integral solution of the FW-H equation based on the free-space Green's function formalism, with time derivatives and the additional assumption of compact acoustic sources, Farassat [19, 20] formulated easily applicable versions to apply the FW-H equation to sound generation from the arbitrary motion of bodies with complicated geometry, e.g. helicopter rotors. The further developments of the FW-H approach have been given on the evaluation methods in respect to the volume integration of turbulent quadrupolar sources [23, 36], and on the formulation for the supersonic moving solid boundary [25, 35] by Farassat et al. The 2D formulations for the FW-H approach have been recently developed by Guo [32] and Locard [49]. These 2D versions of the FW-H approach provide a very efficient way for numerical implementation with the FFT (Fast Fourier Transformation) technique, and reveal explicitly the features of the source mechanisms and characteristics of the acoustic far-field associated with 2D problems. Even for physically 3D problems, the 2D formulation can be used to guide and augment calculations. This possibility has been generally discussed by Monoha et al. [54].

The above achievements constituted the era of traditional aeroacoustic analogies. The major difficulties with this kind of method are that the sound source is not compact in supersonic flows, and that the volume integration of the quadrupolar source term is difficult to compute. The major shortcoming of this kind of method is that the usually used free space Green function neglects the interaction between acoustic propagation and inhomogeneous flow field. Tam [76, 77] discussed the limitations of aeroacoustic analogies in detail.

Another alternative to the integral methods is the Kirchhoff method [26, 51, 83],

which assumes that the sound transmission is governed by the linear wave equation. The main shortcoming of this approach is that the control surface has to be in the linear region. BRENTNER [10] has comprehensively compared the FW-H and Kirchhoff approaches. The conclusion of BRENTNER is that the FW-H method is analytically superior for aeroacoustics, because it is based on the conservation laws of fluid mechanics rather than on the wave equation. Thus, the FW-H equation is valid even if the control surface is in the nonlinear region. The disadvantage of the (impermeable control surface) FW-H approach against the KIRCHHOFF method, is the common problem of traditional acoustic analogies, namely, that the volume integration of the quadrupolar source term is difficult to compute.

A new alternative to the integral method is the use of the permeable (porous) surface FW-H equation. The usual practice is to assume that the FW-H integration surface corresponds to a solid body and is impenetrable. However, if the surface is assumed to be porous, a general equation can be derived, with more completed surface integration on the control surface. The acoustic far-field can be calculated based on the quantities on the control surface provided by a CFD code. If the control surface is large enough and encloses the main turbulent quadrupolar volume sources, the acoustic effects of these sources can be all concerned in the surface integration. Thus the very difficult computation of the turbulent quadrupolar volume sources is avoided. This is a large advantage for a robust and an efficient aeroacoustic approach. The calculations based on the (porous) FW-H approach have been carried out by SINGER [69], LOCARD [49], GLOERFELT [31] etc.

In the integral methods, usually only the GREEN's functions of point sources in an unbounded space are used. If the diffraction and scattering effects of a geometry have to be taken into account, the exact GREEN's function should be used to reduce the computational cost. The exact GREEN's function of an arbitrary geometry is usually unknown and must be computed with the boundary Element Methods (BEM) [54].

The LEE methods are based on two simplification conditions: the very small magnitude of acoustic fluctuations and negligible viscous effects with respect to the acoustic wave propagation. Under these two conditions, the general governing equations, namely NS equations, can be simplified to the acoustic perturbation equations, namely LEE equations. The LEE equations are the time-dependent partial differential equations. They are numerically solved with high order low-dispersion and low-dissipation discrete schemes and complex non-reflecting boundary conditions. Thus, the computational cost of the LEE approach is still very large, although smaller than the DNS and LES. The LEE can be efficiently used for supersonic cases, and is very promising with respect to the interaction effects between the acoustic and flow fields. Moreover, there are two general problems excited by source terms of the LEE equations [18]: convective or global instabilities and excited vorticity eigen-modes of flows. These two problems usually can be avoided by an integral method. The integral method can usually filter out the near-field hydrodynamic

fluctuations and has automatically the wave out-going far-field condition.

In a word, the LEE methods are more accurate than the integral ones in consideration of the sound-flow interaction, but it is still computationally costly with the LEE methods to carry out a practical simulation. The integral methods usually have a similar analytical feature of GREEN's function formalism, and the same limitation with respect to the interaction between the nonuniform mean flow and acoustic propagation. But in many practical applications without significant sound refraction by mean flows, the integral methods have their advantages over the LEE methods on the balance of accuracy and efficiency. Therefore, this work is carried out with the hybrid method in two steps: the first step of near-field CFD and the second step of far-field acoustic integral extension based on (porous) FW-H approach.

In the first step of near-field CFD, there are two main categories of methods, namely unsteady CFD (DNS, LES, and URANS) and steady CFD (RANS) plus stochastic models. The DNS is accurate but very computationally expensive, and available only for the flow at a limited REYNOLDS number. The Large Eddy Simulation (LES) is a good alternative to the DNS, which resolves directly only the important large scale of the turbulent structure through a filtering operation on the NS equations to remove the small spatial scales. The small scale structures of the flow are expressed by a subgrid scale model to obtain a closed equation system. The LES is carried out on a grid, which is small enough to resolve the smallest large scales, but still much larger than the KOLMOGOROV scale required by a DNS. The achievable REYNOLDS number of the simulated flow field can be extended by the LES, in comparison with the DNS. The hybrid aeroacoustic simulations based on the LES have been carried out by SPYROPOULOS [72], MANOHA [55], WANG [81] and EWERT [18]. The steady REYNOLDS-Averaged NAVIER-STOKES Simulation (RANS), in conjunction with stochastic models of wavenumber-frequency spectrum of turbulence [6, 4, 40], and unsteady RANS methods [69, 70] are the other alternatives to the DNS, for the first step of the hybrid aeroacoustic simulation. They can extend the achievable REYNOLDS number of the simulated flow further, but are less accurate than the DNS and LES. In an optimistic view of rapidly developing computer hardware capacity, the LES is adopted in this work as the tool to obtain the acoustic source information in the dynamical near-field. The near-field CFD is carried out by the CFD-solver, SPARC (Structured Parallel Research Code), whose source code is available in the institute.

The CFD-solver, SPARC, used for this work, was also used by PANTLE [59, 58, 60] to carry out aeroacoustic calculations. The work of PANTLE and the current work can be complemented with each other through their differences. The main differences between this work and that of PANTLE are:

PANTLE used the FW-H approach in the traditional meaning, and took the control surface on the solid boundary; she thus had to calculate the volume integration of quadrupolar sources. The current work is based on the (porous) FW-H approach,

and takes the control surfaces in a variety of positions in the source region, and thus the volume integration of quadrupolar sources is theoretically avoided.

PANTLE used only the 3D integral formulation with the free-space GREEN's function of the FW-H approach. In the current work, both the 3D and 2D formulations of the (porous) FW-H approach are implemented in the computer program. Through the comparisons among the results of the 3D and 2D formulations, the 2D approaches are proven to be an efficient way to guide and augment full 3D calculations. Moreover, one of the 2D formulations is based on a GREEN's function with the convective effect of a uniform mean flow.

The computational parameters for the aeroacoustic simulations, such as the position of the control surface, copy length in the span direction, spatial and temporal resolutions, and accuracies of numerical interpolation, derivation and integration, are investigated in this work to obtain an optimization concept of the numerical calculation.

In PANTLE's work, both the LES and URANS were used for the CFD computation; In the current work, only the LES is used. The acoustic far-field generated by an unsteady flow around a circular cylinder at $Re_D = 600$ and $Re_D = 14000$ are calculated in PANTLE's work, as well as, in the current work, at $Re_D = 150$ and $Re_D = 3900$. In PANTLE's work, the simulated acoustic far-field generated by the unsteady flow around a circular cylinder at $Re_D = 14000$ was compared with the experimental results of ETKIN; In the current work, the simulated acoustic far-field is compared in detail with the results of acoustic DNS of INOUE for $Re_D = 150$, and experimental results of NORBERG and SZEPESSY for $Re_D = 3900$. In PANTLE's work, the acoustic far-field generated by unsteady flow around a blade profile is calculated.

In PANTLE's work, the acoustic solver for the second step simulation was integrated with the CFD-solver together with the method of forward-time; in the current work, the acoustic solver is implemented as a postprocessor with the method of retarded-time.

1.3 Scope of This Work

As described in section 1.1 of this work, a disagreeable acoustic environment impact occurs when unsteady flows and their interactions with solid boundaries are produced by aerodynamic machines. In order to reduce the aerodynamic noise, both theoretical and experimental methods should be used to predict the aeroacoustic features of the aerodynamical machine in the early design phase. In theoretical methods, numerical tools have to be employed to solve the complex aeroacoustic problems modeled by analytical approaches. The general objective of this work is the development of computational tools

to simulate aerodynamically generated sound.

In section 1.2 of this work, the current status of analytical modeling concepts of aeroacoustic generation and transmission are shown, from the general governing equations for both the source and propagation mechanism, namely the NS equations, to the analogical equations or the linearized acoustic perturbation equations that split the sound generation and transmission in their strategic ways to simplify the problems, so that the complex aeroacoustic prediction can be carried out to obtain useful references for industrial design. A two-step hybrid approach is chosen to carry out the aeroacoustic simulation in this work, with which the computational domain is separated into two parts, namely the dynamic near-field and the acoustic far-field. The numerical computation is also divided into two steps: in the first step, a compressible NS solver is applied in the computational domain of the dynamic near-field to calculate the source information for the laminar case, and an compressible LES solver is used for the turbulent case. The numerical results of the first step are the required time-dependent quantities of dynamical fluctuations in the near-field, which is the source information for the radiated acoustic far-field, and these are stored in a data base. In the second step, a CAA solver implemented with the formulations of 3D FARASSAT II, 2D GUO, and 2D LOCARD of the (porous) FW-H approach is applied to extend the dynamic near-field to the acoustic far-field, namely, to calculate the far-field sound pressure on the basis of the source information stored in the data base by the first step. Through this data base and the averaging or copying in the span direction of the cylindrical control surface, the first and second steps are coupled.

The CFD-solver, SPARC [53], is applied for the first step simulation in the computational domain of dynamic near-field. This CFD-solver is used to solve the unsteady compressible NS equations for the laminar flow, and used to solve the unsteady compressible spatially filtered NS equations for the turbulent flow by means of LES. The governing equations solved by the CFD and CAA-solver in the first and second steps are presented in chapter 2, and the numerical approaches for the solution of these governing equations are presented in chapter 3.

When a new computer program system is implemented to solve the governing equation system for physical problems of interest, it should be verified and validated before it can be applied to obtain solutions in general cases. In chapter 4, the results of verification and validation of the computer program used in this work, especially new implemented codes for the integral extension from the dynamic near-field to the acoustic far-field, are presented. The verification is based on several analytical solutions, whose details are shown in appendix A. The verification results have given not only a confirmation of the capacity of the computer program, but also a possibility of numerical error estimation, as well as an optimization concept to computational parameters. The aeroacoustic DNS calculated by INOUE [38] is chosen as the benchmark for the validation. The validation results show a good agreement between the results of hybrid simulation of this work and

that of the aeroacoustic DNS of INOUE.

In chapter 5, a computational example of the acoustic far-field generated by unsteady flow around a circular cylinder at $Re_D = 3900$ and $Ma = 0.2$ is presented. The simulation is carried out with a hybrid simulation of an LES in the dynamic near-field and an integral extension from the dynamic near-field to the acoustic far-field based on the 3D and 2D formulations of the (porous) FW-H approach. The simulated directivity represents an acoustic far-field generated by a lift dipole and a drag dipole. The overall sound level is compared with the experimental result of NORBERG [11], and the frequency spectrum is compared with the experimental result of SZEPESSY [74]. The comparisons between numerical and experimental results give a good agreement.

In chapter 6, the robust and efficient features of the three integral extension formulations implemented into the computer program for the current work are concluded. The whole features of the acoustic far-field of flow around a circular cylinder can be well simulated by this computer program. The experiences by using this computer program in a series of verification and validation examples are concluded to a optimization concept of computational parameters, and are used to take an outlook for future researches.

The main goals of this work can be summarized as: Firstly, the computer program to calculate the acoustical far field of unsteady flow around solid structures is implemented on the bases of different 3D and 2D formulations of the FW-H equation with permeable (porous) control surface and coupled with the CFD-solver SPARC. Then this computer program system is verified with analytical solutions for the possible application conditions; and through these comprehensive verifications, an estimation of numerical errors and optimization concepts of the computational parameters are concluded. Finally, this aeroacoustic code is used to calculate the acoustic far field of the flow around a cylinder at different REYNOLDS numbers. The computational results of the case at a lower REYNOLDS number, corresponding to a laminar wake, is compared with the aeroacoustic DNS of INOUE [38] to validate the code. The computational results of the case at a higher REYNOLDS number, corresponding to a turbulent wake, give a good agreement with experimental results, and give a new knowledge over the efficient approach by using 2D formulations of FW-H equation to the application of LES with the periodical conditions in the span direction of a cylinder.

Chapter 2

Governing Equations

The goal of this work is to develop a computational tool to simulate flow-induced sound with the so-called first disciplines of physical laws, namely the general laws of classical continuum mechanics. Since the magnitude of acoustic fluctuations in the much larger propagation area is in general much smaller than that of dynamical fluctuations in the much smaller source region of unsteady flow, hybrid methods based on a decomposition of the computational field into two domains with different analytical and numerical treatments, namely the dynamical near-field and acoustic far-field, are rational. They allow that the complicated NS equations have to be only solved in the smaller near-field source region with fine spatial resolutions by a CFD-solver; the extension of near-field CFD results to the acoustic far-field is then given by special CAA-solvers with special treatments on small-scale acoustic fluctuations, such as LEE or acoustic-analogical-solvers. In this work, the integral extensions based on the FW-H equation are used.

2.1 Governing Equations for Near-field CFD

At time, t , and position, $x_i = (x_1, x_2, x_3)$, the state of a fluid is defined when the velocity, $u_i = (u_1, u_2, u_3)$, and any two thermodynamic variables such as pressure, p , density, ρ , temperature, θ , and so on, are specified. These quantities of a fluid are governed by the so-called basic equations of fluid mechanics, namely the continuity, momentum, and energy equations of a compressible, viscous fluid which are the statements of the conservation of mass, momentum and energy respectively. The momentum equations for a viscous fluid were derived by C.L.M.H. NAVIER (1823) and G.STOKES (1845) independently, and are called NAVIER-STOKES (NS) equations. Sometimes the equation system of continuity, NS and energy equations are called also the NS equation system, or simply NS equations. If more than two thermodynamic variables are used, the additional thermodynamic equations should be implemented to close the equation system, such as the state equation of an ideal gas, etc. Sometimes even the second law of thermodynamics is required to get a realizable solution of the basic equations of fluid mechanics.

2.1.1 Compressible NS Equations

In this section, the basic equations of fluid mechanics are presented as the analytical starting point for both the near-field CFD and far-field CAA. In this work, the volume (remote) force in the basic equations, namely the gravity for the simulated cases, is neglected, since it has little effect on the sound generation.

The velocity, u_i , and density, ρ , of the fluid must satisfy the continuity equation to fulfill the conservation of the fluid mass:

$$\frac{\partial \rho}{\partial t} + \frac{\partial \rho u_i}{\partial x_i} = 0 \quad (2.1)$$

The momentum equations, or so-called NS equations, express the rate of momentum change of a fluid particle in terms of the pressure gradient, $\frac{\partial p}{\partial x_i}$, and viscous stress gradient, $\frac{\partial \tau_{ij}}{\partial x_j}$:

$$\frac{\partial \rho u_i}{\partial t} + \frac{\partial \rho u_i u_j}{\partial x_j} = -\frac{\partial p}{\partial x_i} + \frac{\partial \tau_{ij}}{\partial x_j} \quad (2.2)$$

where the viscous stress, τ_{ij} , can be calculated from the strain rate, S_{ij} , by using the feature of Newton's fluid:

$$\tau_{ij} = \mu S_{ij} \quad (2.3)$$

$$S_{ij} = \frac{\partial u_i}{\partial x_j} + \frac{\partial u_j}{\partial x_i} - \frac{2}{3} \frac{\partial u_k}{\partial x_k} \delta_{ij} \quad (2.4)$$

In the full generality the energy equation must be introduced to solve the problems with thermodynamic processes. For a compressible solver used in this work, the energy equation has to be used to close the equation system, although the thermodynamic changes are small enough to be negligible for the sound generation. The energy equation represents the rate of total energy change of a fluid particle in terms of the power gradient of pressure, $\frac{\partial p u_k}{\partial x_k}$, the power gradient of viscous stress, $\frac{\partial \tau_{ij} u_j}{\partial x_i}$, and the heat flux gradient, $\frac{\partial q_k}{\partial x_k}$:

$$\frac{\partial \rho E}{\partial t} + \frac{\partial \rho E u_k}{\partial x_k} = -\frac{\partial p u_k}{\partial x_k} + \frac{\partial \tau_{ij} u_j}{\partial x_i} - \frac{\partial q_k}{\partial x_k} \quad (2.5)$$

where E is the specific total energy, and q_k is the heat flux:

$$E = e + k \quad (2.6)$$

$$q_k = -K \frac{\partial \theta}{\partial x_k} \quad (2.7)$$

where e is the specific internal energy:

$$e(\vec{x}, t) = C_v \theta(\vec{x}, t) \quad (2.8)$$

where C_v is the specific heat at constant volume, and k is the specific kinetic energy:

$$k = \frac{1}{2} u_k u_k \quad (2.9)$$

K is the thermal conduction coefficient and calculated as follows:

$$K = \frac{C_p}{Pr} \mu(\theta) \quad , \quad \theta = \theta(\vec{x}, t) \quad (2.10)$$

where C_p is the specific heat at constant pressure, and Pr is the PRANDTL number. The dynamical viscosity, μ , is given by Sutherland's formula for air:

$$\mu(\theta) = \mu(\theta_0) \frac{110.4 + \theta_0}{110.4 + \theta(\vec{x}, t)} \left(\frac{\theta(\vec{x}, t)}{\theta_0} \right)^{\frac{3}{2}} \quad (2.11)$$

where the normal temperature, θ_0 , is chosen as 273 (K).

Because three thermodynamic variables, namely p , ρ and θ are used, the state equation of an ideal gas is required:

$$\theta = \frac{1}{R} \frac{p}{\rho} \quad (2.12)$$

and the following relationships between the thermodynamic coefficients are also required:

$$\gamma = \frac{C_p}{C_v} \quad (2.13)$$

$$C_p - C_v = R \quad (2.14)$$

The ratio of the specific heats, γ , and the PRANDTL number, Pr , are given the values 1.4 and 0.72 for the air flow respectively.

2.1.2 Spatially Filtered NS Equations

Direct numerical simulation (DNS) to solve the NS equation system described in the above section 2.1.1 requires a very fine spatial resolution for high RENOLDS number flows. But in such an expensive DNS, a huge amount of information about the flow field is generated which is usually not required in practical usage. It is a clever compromise way to make a coarser resolution of the large scale needed for practical usage while modeling only the small ones. This approach is usually called Large Eddy Simulation (LES). Compared with the RENOLDS Averaged Navier-Stokes equation approach (RANS), the LES has the advantage for the solution of the instantaneous field of an unsteady flow with the frequency spectrum needed. The basic idea of LES can be also interpreted as a spatial average or filtering.

This spatial average or filtering is so formulated that the flow parameter, $\Phi(\vec{x}, t)$, is separated into two parts of the large and fine structural values:

$$\Phi(\vec{x}, t) = \overline{\Phi}(\vec{x}, t) + \Phi'(\vec{x}, t) \quad (2.15)$$

with the spatial averaged coarse structural value:

$$\overline{\Phi}(\vec{x}, t) = \int_{V(\vec{x}, t)} G(\vec{x} - \vec{x}', \Delta(\vec{x})) \Phi(\vec{x}', t) d\vec{x}'^3 \quad (2.16)$$

where $G(\vec{x} - \vec{x}', \Delta(\vec{x}))$ is a filter function. The most commonly used filter functions are the sharp Fourier cutoff, Gaussian and top-hat filters. In the current work, an implicit box filter is used.

For the compressible solver, the spatial average or filtering is usually defined through the so-called FAVRE filtering:

$$\Phi(\vec{x}, t) = \tilde{\Phi}(\vec{x}, t) + \Phi''(\vec{x}, t) \quad (2.17)$$

with the density weighted average term:

$$\tilde{\Phi}(\vec{x}, t) = \frac{\overline{\rho\Phi}(\vec{x}, t)}{\overline{\rho}} \quad (2.18)$$

The filtered basic equations after some simplifications are :

$$\frac{\partial \overline{\rho}}{\partial t} + \frac{\partial \overline{\rho u_i}}{\partial x_i} = 0 \quad (2.19)$$

$$\frac{\partial \overline{\rho u_i}}{\partial t} + \frac{\partial \overline{\rho u_i u_j}}{\partial x_j} + \frac{\partial \overline{\rho}}{\partial x_i} - \frac{\partial \widehat{\tau_{ij}}}{\partial x_j} = -\frac{\partial \tau_{ij}^{sgs}}{\partial x_j} \quad (2.20)$$

$$\frac{\partial \overline{\rho \hat{E}}}{\partial t} + \frac{\partial (\overline{\rho \hat{E}} + \overline{p}) \widetilde{u}_k}{\partial x_k} - \frac{\partial \widehat{\tau_{ij} u_i}}{\partial x_j} + \frac{\partial \widehat{q}_k}{\partial x_k} = -\frac{\partial q_k^{sgs}}{\partial x_k} \quad (2.21)$$

where the **bar**-symbol ' $\overline{}$ ' denotes a filtering operation, the **tilde**-symbol ' $\widetilde{}$ ' denotes a FAVRE filtering operation, and the **hat**-symbol ' $\widehat{}$ ' does not denote a filtering operation but indicates that the quantity is based on filtered variables.

The right-hand sides of the above filtered basic equations 2.19 to 2.21 contain the so-called subgrid-terms, which represent the effect of the unresolved subgrid-scales. In equations 2.19 to 2.21, only the subgrid terms arising from filtering the convective fluxes are retained. In principle, more SGS terms arise when filtering the compressible NS equations 2.1, 2.2 and 2.5. But the SGS terms resulting from nonlinearities of the viscous stress terms and the other terms in the energy equation are omitted in equations 2.19 to 2.21 because the contributions of these terms are negligible in the simulated low-MACH-number cases in this work. Therefore, only the modeling for the SGS stress tensor, τ_{ij}^{sgs} ,

in the filtered momentum equations and the SGS heat flux, q_{sgs} , in the filtered energy equation, are required to close the total governing equation system.

In equations 2.19 to 2.21, the viscous stress tensor, $\widehat{\tau}_{ij}$, after filtering, is defined as:

$$\widehat{\tau}_{ij} = \widehat{\mu} \left(\frac{\partial \widetilde{u}_i}{\partial x_j} + \frac{\partial \widetilde{u}_j}{\partial x_i} - \frac{2}{3} \frac{\partial \widetilde{u}_k}{\partial x_k} \delta_{ij} \right) \quad (2.22)$$

$$\widehat{\mu} = \mu(\theta_0) \frac{110.4 + \theta_0}{110.4 + \widetilde{\theta}} \left(\frac{\widetilde{\theta}}{\theta_0} \right)^{\frac{3}{2}} \quad (2.23)$$

And the filtered state equation of the ideal gas is:

$$\widetilde{\theta} = \frac{1}{R} \frac{\overline{p}}{\overline{\rho}} \quad (2.24)$$

The total energy density, \widehat{E} , and heat flux, \widehat{q}_k , of the filtered variables is calculated as follows:

$$\widehat{E} = C_v \widetilde{\theta} + \frac{1}{2} \widetilde{u}_i \widetilde{u}_i + k_{sgs} \quad (2.25)$$

$$\widehat{q}_k = -\widehat{K} \frac{\partial \widetilde{\theta}}{\partial x_k} \quad (2.26)$$

where the FAVRE filtered thermal conduction coefficient, \widehat{K} , is given by:

$$\widehat{K} = \frac{C_p}{Pr} \widehat{\mu} \quad (2.27)$$

and k_{sgs} is the SGS kinetic energy which is small for air and can be neglected for the calculation of \widehat{E} as LESIEUR and COMTE [45] have shown.

The SGS stress tensor, τ_{ij}^{sgs} , is defined as:

$$\tau_{ij}^{sgs} \equiv \overline{p} (\widetilde{u}_i \widetilde{u}_j - \widetilde{u}_i \widetilde{u}_j) \quad (2.28)$$

The SGS heat flux, q_i^{sgs} , is defined as:

$$q_i^{sgs} \equiv \overline{p} \left[(\widetilde{E} u_i - \widehat{E} \widetilde{u}_i) + \left(\frac{\widetilde{p}}{\rho} u_i - \frac{\overline{p}}{\overline{\rho}} \widetilde{u}_i \right) \right] \quad (2.29)$$

In this work, the eddy viscosity model of SMAGORINSKY [71] is used to calculate the SGS stress, τ_{ij}^{sgs} :

$$\tau_{ij}^{sgs} = \overline{p} \nu_{sgs} \widehat{S}_{ij} \quad (2.30)$$

$$\nu_{sgs} = (C_s \Delta)^2 \sqrt{\widehat{S}_{ij} \widehat{S}_{ij}} \quad (2.31)$$

where the constant value of $C_s = 0.1$ is used, and Δ is the filter width of an implicit box-filter, and can be calculated as following by the finite-volume-method:

$$\Delta = (V)^{\frac{1}{3}} \sqrt[3]{1 - \exp\left(\frac{-y^+}{25}\right)} \quad (2.32)$$

where V is the volume of the local grid cell, and y^+ is the local dimensionless distance to the solid wall:

$$y^+ = \frac{\rho y u_\tau}{\mu} \quad \text{with} \quad u_\tau = \sqrt{\frac{\tau_w}{\rho}} \quad (2.33)$$

If the computational position is far from the solid wall, it is obvious that:

$$\Delta = (V)^{\frac{1}{3}} \quad (2.34)$$

An eddy diffusivity model [30] is used to calculate the SGS heat flux, q_i^{sgs} :

$$q_k^{sgs} = -K_{sgs} \frac{\partial \tilde{\theta}}{\partial x_k} \quad (2.35)$$

$$K_{sgs} = \bar{\rho} \frac{C_p}{Pr_{sgs}} \nu_{sgs} \quad (2.36)$$

with a SGS PRANDTL number, $Pr_{sgs} = 0.7$.

2.2 Governing Equations for Far-field CAA

In the second step of the hybrid CFD/CAA method used in this work, the (porous) FLOWCS-WILLIAMS HAWKINGS (FW-H) approach is selected for the extension of the near-field CFD to the acoustic far-field prediction. The advantages and shortcomings of this approach have been discussed in section 1.2. In this section, at first, the differential formulation of the FW-H equation is introduced, and discussed about its acoustic source terms calculated by a DNS or LES. Then several three and two-dimensional integral formulations of the FW-H equation are presented, which are implemented into computer programs to calculate the acoustic far-field in this work.

2.2.1 Differential Formulation

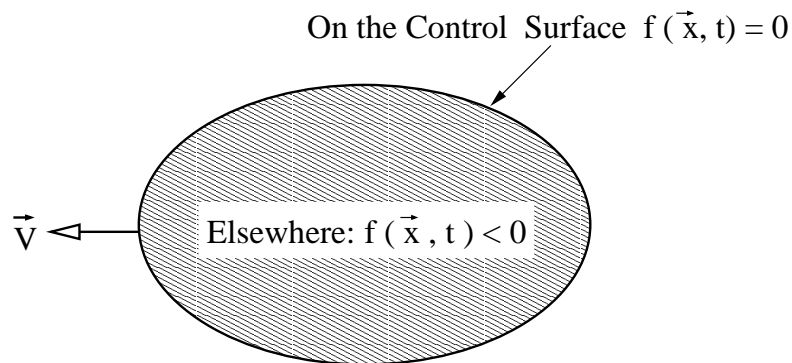
The differential form of the FW-H equation is an exact rearrangement of the continuity and NS equations into an inhomogeneous wave equation in unbounded space with the aid of the mathematical tool of generalized functions. In this work, the acoustic process is supposed to be homentropic, namely the specific entropy, s , of the acoustic medium is uniform and constant throughout the whole acoustic field, so that the energy equation becomes $s = \text{constant}$, for the acoustic propagation. Therefore, the acoustic pressure, p' is

only a function of density fluctuation, ρ' . The aeroacoustic process with heat effects, such as sound from combustion or frictional dissipation of sound, and highly nonlinear events, such as shock waves, are not treated in this work.

Originally the FW-H equation was derived to include the effects of solid surfaces in arbitrary motion. FFOWCS-WILLIAMS and HAWKINGS used general functions to describe flow quantities in this inhomogeneous wave equation in order to transport the exterior fluid field around the solid surface into an unbounded space, since an integral general solution of this wave equation can thus be obtained by convoluting it with a free-space Green function. They introduced a control surface enclosing the moving solid surface and then derived an inhomogeneous wave equation with two surface source terms on the control surface and a volume source term out of the control surface. From the original design by FFOWCS-WILLIAMS and HAWKINGS the control surface is just the solid surface which is impermeable, and the fluid velocity on the control surface is the same as that of the solid surface. But these impermeable and non-slip restrictions are not necessary for the derivation of the differential form of the FW-H equation.

If permeable and non-uniform fluid velocities on the control surface are defined, the permeable (porous) integral forms of the FW-H equation can also be implemented, which makes the FW-H approach more robust and efficient. In the present context the differential form of FW-H equation is presented. The three and two-dimensional integral general solutions based on the permeable control surface will be shown in the next two sections 2.2.2 and 2.2.3.

Let $f(\vec{x}, t)$ be an indicator function of the control surface in arbitrary motion (see Figure 2.1):



In the Fluid Field Concerned :
 $f(\vec{x}, t) > 0$

Figure 2.1: The Indicator Function about a Control Surface

$$f(\vec{x}, t) \begin{cases} > 0 & : \text{ in the fluid field concerned} \\ = 0 & : \text{ on the control surface} \\ < 0 & : \text{ elsewhere} \end{cases} \quad (2.37)$$

Then the Heaviside function is defined as:

$$H(f(\vec{x}, t)) = \begin{cases} 1 & : \text{ when } f(\vec{x}, t) > 0 \\ 0 & : \text{ when } f(\vec{x}, t) < 0 \end{cases} \quad (2.38)$$

And whether on the control surface or not:

$$\frac{dH}{dt} = \frac{\partial H}{\partial f} \left(\frac{\partial f}{\partial t} + \frac{\partial f}{\partial x_i} \frac{\partial x_i}{\partial t} \right) = \frac{\partial H}{\partial t} + \frac{\partial H}{\partial x_i} v_i = 0 \quad (2.39)$$

$$v_i = \frac{\partial x_i}{\partial t} \quad (\text{the velocity of control surface}) \quad (2.40)$$

A DIRAC's delta function is defined as:

$$\delta(f(\vec{x}, t)) = \frac{\partial H}{\partial f} = \begin{cases} 1 & : \text{ when } f(\vec{x}, t) = 0 \\ 0 & : \text{ when } f(\vec{x}, t) \neq 0 \end{cases} \quad (2.41)$$

Therefore:

$$\frac{\partial H}{\partial x_i} = \frac{\partial H}{\partial f} \frac{\partial f}{\partial x_i} = \delta(f) \cdot |\nabla f| n_i \quad (2.42)$$

where n_i is the local outer normal of the control surface:

$$n_i = \frac{\frac{\partial f}{\partial x_i}}{\sqrt{\frac{\partial f}{\partial x_j} \frac{\partial f}{\partial x_j}}} \quad (2.43)$$

Through the above generalized functions, the basic equations of aerodynamics can be transformed to the FW-H equation. First, multiply the NS equations 2.2 by $H(f)$ and rearrange into the form:

$$\begin{aligned} \frac{\partial}{\partial t} [H(f) \rho u_i] + \frac{\partial}{\partial x_i} [H(f) c_0^2 (\rho - \rho_0)] = \\ - \frac{\partial}{\partial x_j} [T_{ij} H(f)] + [\rho u_i (u_j - v_j) + (p - p_0) \delta_{ij} - \tau_{ij}] \frac{\partial H(f)}{\partial x_j} \end{aligned} \quad (2.44)$$

where u_i is the velocity of fluid, v_i is the local velocity of the control surface (see equation 2.40), and ρ_0 , p_0 , and c_0 are the density, static pressure and sound speed in the undisturbed medium. T_{ij} is the so-called Lighthill's stress:

$$T_{ij} = \rho u_i u_j + [(p - p_0) - c_0^2 (\rho - \rho_0)] \delta_{ij} - \tau_{ij} \quad (2.45)$$

Then, the same procedure applied to the continuity equation 2.1 and rearrange into:

$$\frac{\partial}{\partial t} [H(f) (\rho - \rho_0)] + \frac{\partial}{\partial x_i} [H(f) \rho u_i] = [\rho (u_i - v_i) + \rho_0 v_i] \frac{\partial H(f)}{\partial x_i} \quad (2.46)$$

The elimination of $H(f)\rho u_i$ between the above two equations yields the differential form of the FW-H equation, which is an exact rearrangement of the continuity and Navier-Stokes equations into a form of inhomogeneous wave equation:

$$\left(\frac{1}{c_0^2} \frac{\partial^2}{\partial t^2} - \frac{\partial^2}{\partial x_i^2}\right)[Hc_0^2(\rho - \rho_0)] = -\frac{\partial}{\partial x_i}[L_i | \nabla f | \delta(f)] + \frac{\partial}{\partial t}[\rho_0 U_n | \nabla f | \delta(f)] + \frac{\partial^2(HT_{ij})}{\partial x_i \partial x_j} \quad (2.47)$$

$$L_i = [(p - p_0) \delta_{ij} - \tau_{ij} + \rho u_i(u_j - v_j)] n_j \quad (2.48)$$

$$U_n = U_i n_i \quad , \quad U_i = \frac{\rho u_i}{\rho_0} + \left(1 - \frac{\rho}{\rho_0}\right) v_i \quad (2.49)$$

The equation 2.47 is called the differential form of the FW-H equation, and it was derived and published by J. E. FLOWERS-WILLIAMS and D. L. HAWKINGS in 1969 [82]. In the right side of the above differential form of the FW-H equation, there are three analogical source terms, which have physical meanings if the control surface is the same as the surface of a rigid body, namely:

the thickness noise: $\frac{\partial}{\partial t}[\rho_0 U_n | \nabla f | \delta(f)]$ (monopolar surface sources on $f(\vec{x}, t) = 0$);

the loading noise: $\frac{\partial}{\partial x_i}[L_i | \nabla f | \delta(f)]$ (dipolar surface sources on $f(\vec{x}, t) = 0$);

the T_{ij} noise: $\frac{\partial(HT_{ij})}{\partial x_i \partial x_j}$ (quadrupole volume sources in $f(\vec{x}, t) > 0$).

For the FW-H equation in the traditional meaning with impermeable (solid) control surface, the thickness noise is determined completely by the geometry and kinematics of the moving solid body. The loading noise is generated by the force that acts on the fluid as a result of the presence of the body. The quadrupole volume source term accounts for nonlinear effects, e.g. noise generated by shocks, turbulence and vorticity in the flow fields, nonlinear wave propagation and steepening, and variations of the local sound speed. The control surface, $f(\vec{x}, t) = 0$, may coincide with the surface of a moving solid body or mark a convenient interface between fluid regions which enclose the moving solid region (the source region). For a porous surface, the terms of the thickness and loading noise lose their original physical meanings, but the last term still denotes the quadrupoles outside the (porous) control surface, $f(\vec{x}, t) > 0$.

In their 1969 paper [82], FLOWERS-WILLIAMS and HAWKINGS utilized the powerful technique of generalized function theory to develop both the above FW-H equation and the governing equation of the KIRCHHOFF formulation for moving surfaces. In the derivation of the FW-H equation by FLOWERS-WILLIAMS and HAWKINGS, there was no assumption of an impermeable control surface. This means that the original FW-H equation derived in 1969 has allowed a porous (permeable) control surface. But it was P. di FRANCESCANTONIO who was the first to demonstrate that, for the far field

helicopter rotor noise prediction, the FW-H equation can be practically used on a fictitious permeable surface that does not correspond to a physical solid surface, just like the KIRCHHOFF approach [16]. The advantages of this application by FRANCESCANTONIO are both the advantages of the FW-H and KIRCHHOFF approach, namely, robust in the non-linear region like the FW-H approach and without the expensive volume integration of quadrupolar sources like the KIRCHHOFF approach. At the same time, PILON and LYRINTZIS also used the FW-H equation on a porous control surface [62].

In the source terms, L_i and U_n , defined by the equations 2.48 and 2.49, the flow velocity relative to the solid surface, u_i , vanishes by a traditional FW-H approach with an impermeable control surface on the physical body due to the viscous non-split boundary condition; as well, the u_i is usually not zero by a porous FW-H approach with a fictitious permeable control surface away from the solid body. The advantage of such an FW-H approach over the traditional FW-H approach is based on the fact that all the quadrupole volume sources enclosed by the control surface are accounted for by the surface sources of L_i and U_n . For a porous FW-H approach, it is important for the calculation of effects of quadrupole sources that the velocity fluctuation on the control surface should be precisely calculated on the control surface. In practice, if the control surface is large or near to the external boundary of the CFD domain, the velocity fluctuation may be difficult to be simulated very accurately. The error by the calculation of the velocity fluctuation may make both the simulation of deterministic tonal noise and statistic wide-band turbulent noise fail. Therefore, an accurate near field CFD is the necessary precondition for a successful porous FW-H approach. For the flow around a geometrically complex solid structure, a geometrically simple control surface can be used by the porous FW-H approach to improve efficiency and accuracy, since the spatial resolution on a complicated control surface with sharp corners should be much finer to obtain the required accuracy by the surface integrations of vector quantities.

The source terms, T_{ij} , L_i and U_n , in the FW-H equation 2.47 are calculated by the first step of the CFD/CAA method, namely from a near-field DNS or LES. While DNS yields a complete representation of these source terms on the strength and frequency of the whole spectrum, LES can only resolve a part of strength and frequency of the spectrum. To analyze the unresolved parts through an LES, the control surface, $f(\vec{x}, t) = 0$, can be assumed to be stationary: $v_i = 0$, and the viscous stress, τ_{ij} , can also be assumed to be negligible. Then the resolved parts of the source terms, which are denoted as T_{ij}^{les} , L_i^{les} and U_n^{les} , are:

$$T_{ij}^{les} = \overline{\rho \tilde{u}_i \tilde{u}_j} \quad (2.50)$$

$$L_i^{les} = [(\overline{p} - p_0) \delta_{ij} + \overline{\rho \tilde{u}_i \tilde{u}_j}] n_j \quad (2.51)$$

$$U_n^{les} = \hat{U}_i n_i \quad , \quad \hat{U}_i = \frac{\overline{\rho \tilde{u}_i}}{\rho_0} \quad (2.52)$$

Compared with the completely resolved source terms, T_{ij} , L_i and U_n , by a DNS, the

unresolved parts are shown as follows:

$$T_{ij} = T_{ij}^{les} + T_{ij}^{sgs} + T_{ij}'' \quad (2.53)$$

$$L_i = L_i^{les} + L_i^{sgs} + L_i'' \quad (2.54)$$

$$U_n = U_n^{les} + U_n'' \quad (2.55)$$

where the terms with the superscript, sgs, are the SGS terms modeled with the corresponding SGS models, which are defined as :

$$T_{ij}^{sgs} \equiv \bar{\rho} (\widetilde{u_i u_j} - \widetilde{u_i} \widetilde{u_j}) \quad (2.56)$$

$$L_i^{sgs} \equiv \bar{\rho} (\widetilde{u_i u_j} - \widetilde{u_i} \widetilde{u_j}) n_j \quad (2.57)$$

The values of T_{ij}^{sgs} and L_i^{sgs} are also calculated by an LES. But if the filter width of the LES is fine enough, e.g. $\Delta/\eta \leq 10$, T_{ij}^{sgs} and L_i^{sgs} are very small compared to T_{ij}^{les} , L_i^{les} and negligible. The totally unresolved terms, T_{ij}'' , L_i'' and U_n'' , are in very high frequencies and play little role in the overall sound level. The main problem by the use of LES is that the LES shifts the peak of the spectrum densities towards low frequencies and damps the spectrum densities in higher frequencies, because the LES changes the value of $\frac{\partial^2 T_{ij}}{\partial x_i \partial x_i}$, $\frac{\partial L_i}{\partial x_i}$ and $\frac{\partial U_n}{\partial t}$ relatively more than those of T_{ij} , L_i and U_n , where x_i is the observation position and in the acoustic far-field: $\frac{\partial}{\partial x_i} \approx \frac{1}{c_0} \frac{\partial}{\partial t}$. If T_{ij} , L_i or U_n take a value of $e^{i\omega t}$, the value of $\frac{\partial^2 T_{ij}}{\partial x_i \partial x_i}$, $\frac{\partial L_i}{\partial x_i}$ or $\frac{\partial U_n}{\partial t}$ after the numerical calculation will be:

$$\frac{\delta^2}{\delta t^2} e^{i\omega t} = -\omega'^2 e^{i\omega' t} \quad (2.58)$$

$$\frac{\delta}{\delta t} e^{i\omega t} = -\omega' e^{i\omega' t} \quad (2.59)$$

where $\omega' < \omega$. The amplitudes of the second or first derivatives of rapidly oscillating functions will thus be reduced substantially. For the porous FW-H approach, if the control surface encloses the main volume sources, only the first derivative terms need to be calculated, and then more accurate results than the traditional FW-H approach on this aspect can be obtained.

2.2.2 3D Integral Formulations

As discussed in the above section of this work, the differential formulation of the FW-H equation is an exact rearrangement of the continuity and NS equations into a form of inhomogeneous wave equation in an unbounded space. The purposes of this rearrangement are not only to display the analogic source terms on the right-hand side of the equation, but also to get a formal solution of this inhomogeneous wave equation by the mean of GREEN functions.

The often used Green function is the free-space GREEN's function, $G(\vec{x}, \vec{y}; t, \tau)$, which is a causal solution of the wave solution generated by an impulsive point source, $\delta(\vec{x} - \vec{y})\delta(t - \tau)$, located at the point $\vec{x} = \vec{y}$ at the time $t = \tau$ in an unbounded space at rest. In other words, the free-space GREEN's function, $G(\vec{x}, \vec{y}; t, \tau)$, is the outgoing wave solution of the following equation:

$$\left(\frac{1}{c_0^2} \frac{\partial^2}{\partial t^2} - \frac{\partial^2}{\partial x_i \partial x_i} \right) G(\vec{x}, \vec{y}; t, \tau) = \delta(\vec{x} - \vec{y})\delta(t - \tau) \quad (2.60)$$

And it is easy to obtain the solution of this free-space GREEN's function as:

$$\begin{aligned} G(\vec{x}, t; \vec{y}, \tau) &= \frac{1}{4\pi r} \delta\left(t - \tau - \frac{r}{c_0}\right) , \\ r &= |\vec{x} - \vec{y}| . \end{aligned} \quad (2.61)$$

where (\vec{x}, t) denotes the observation position and time, and (\vec{y}, τ) denotes source position and time. The reference frame in space and time is shown in figure 2.2 (see page 24).

By using a free-space GREEN's function to write down an outgoing wave solution of the differential form of the FW-H equation, the integral form of the FW-H equation can be derived.

Let $Q(\vec{y}, \tau)$ denote the sum of three source terms in the right-hand side of the differential form of the FW-H equation (equation 2.47):

$$Q(\vec{y}, \tau) = \frac{\partial^2 (HT_{ij})}{\partial x_i \partial x_j} - \frac{\partial}{\partial x_i} [L_i |\nabla f| \delta(f)] + \frac{\partial}{\partial t} [\rho_0 U_n |\nabla f| \delta(f)] \quad (2.62)$$

Assuming that the source region is compact, namely the characteristic sound wavelength is much larger than the characteristic source region scale, and that the interaction between the sound and flow field is negligible, the following formal solution of the differential form of the FW-H equation can be obtained:

$$Hc_0^2(\rho - \rho_0) = \int_{-\infty}^{+\infty} \oint_{f(\vec{y}, \tau) \geq 0} Q(\vec{y}, \tau) G(\vec{x}, t; \vec{y}, \tau) d^3 \vec{y} d\tau \quad (2.63)$$

With the following identical relationships:

$$\begin{aligned} & \oint_{f(\vec{y}, \tau) \geq 0} \frac{\partial^n F(\vec{y}, \tau)}{\partial y_i \partial y_j \cdots \partial y_n} G(\vec{x}, t; \vec{y}, \tau) d^3 \vec{y} \\ &= \frac{\partial^n}{\partial x_i \partial x_j \cdots \partial x_n} \oint_{f(\vec{y}, \tau) \geq 0} F(\vec{y}, \tau) G(\vec{x}, t; \vec{y}, \tau) d^3 \vec{y} \end{aligned} \quad (2.64)$$

$$|\nabla f| d^2 \vec{y} = dS(\vec{y}) \quad , \quad d^3 \vec{y} = dV(\vec{y}) \quad (2.65)$$

$$Hc_0^2(\rho - \rho_0) = H(p - p_0) = Hp' \quad (2.66)$$

the formal solution of the differential form of the FW-H equation can be written as:

$$Hp'(\vec{x}, t) = Hp_Q'(\vec{x}, t) + Hp_T'(\vec{x}, t) + Hp_L'(\vec{x}, t) \quad (2.67)$$

$$Hp_Q'(\vec{x}, t) = \frac{\partial^2}{\partial x_i \partial x_j} \int_{-\infty}^{+\infty} \oint_{f(\vec{y}, \tau) > 0} \frac{T_{ij}(\vec{y}, \tau) \delta(t - \tau - \frac{r}{c_0})}{4\pi r} dV(\vec{y}) d\tau \quad (2.68)$$

$$Hp_L'(\vec{x}, t) = -\frac{\partial}{\partial x_i} \int_{-\infty}^{+\infty} \oint_{f(\vec{y}, \tau) = 0} \frac{L_i(\vec{y}, \tau) \delta(t - \tau - \frac{r}{c_0})}{4\pi r} dS(\vec{y}) d\tau \quad (2.69)$$

$$Hp_T'(\vec{x}, t) = \frac{\partial}{\partial t} \int_{-\infty}^{+\infty} \oint_{f(\vec{y}, \tau) = 0} \frac{\rho_0 U_n(\vec{y}, \tau) \delta(t - \tau - \frac{r}{c_0})}{4\pi r} dS(\vec{y}) d\tau \quad (2.70)$$

where the source strengths, T_{ij} , L_i and U_n , are defined in equation 2.45 and 2.47. In the above formulation, the \vec{x} and \vec{y} are respectively the observation and source positions represented in the Eulerian coordinates fixed to the undisturbed rest (see figure 2.2).

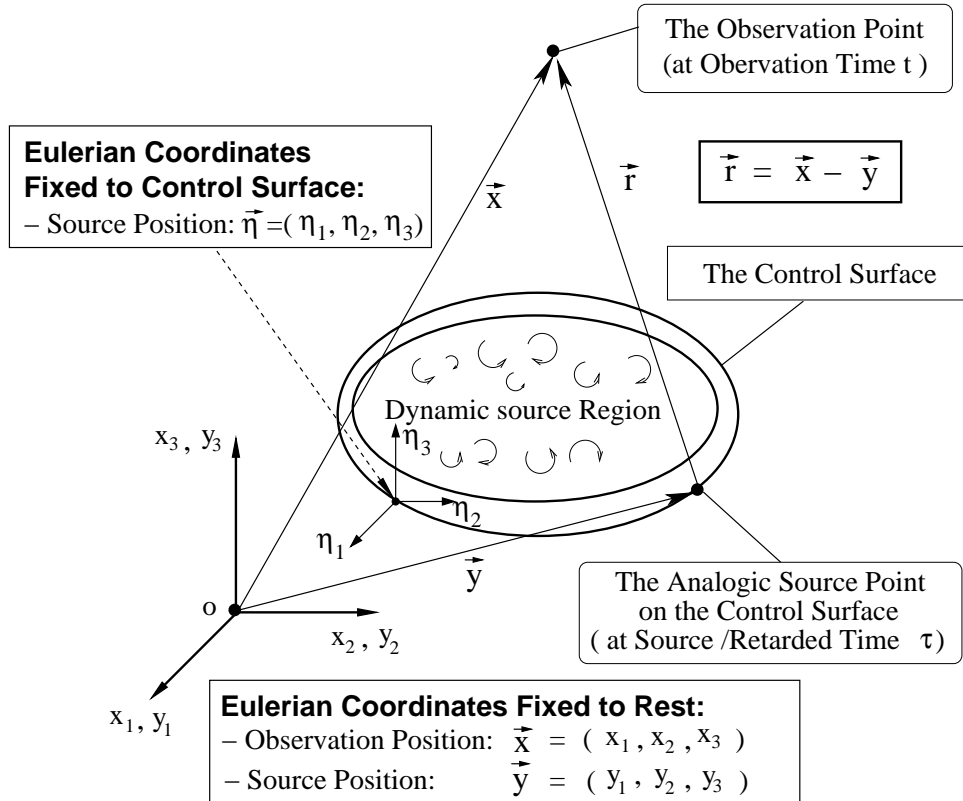


Figure 2.2: The Reference Frame with Source and Observation Positions

If the derivatives of the observation position, $\frac{\partial}{\partial x_i}$, are transformed into the derivatives of observation time, $\frac{\partial}{\partial t}$, and the quadrupole volume term is neglected under the assumption of a permeable (porous) control surface which is large enough to enclose the main

volume sources, the integral form of the FW-H equation can be written as the so-called FARASSAT's formulation I [20]:

$$Hp'(\vec{x}, t) = Hp_T'(\vec{x}, t) + Hp_L'(\vec{x}, t) \quad (2.71)$$

$$4\pi p_T'(\vec{x}, t) = \frac{\partial}{\partial t} \oint_{f(\vec{y}, \tau)=0} \left[\frac{\rho_0 U_n}{r|D|} \right]_{\tau=t-\frac{r}{c_0}} dS(\vec{y}) \quad (2.72)$$

$$\begin{aligned} 4\pi p_L'(\vec{x}, t) &= \frac{1}{c_0} \frac{\partial}{\partial t} \oint_{f(\vec{y}, \tau)=0} \left[\frac{L_r}{r|D|} \right]_{\tau=t-\frac{r}{c_0}} dS(\vec{y}) \\ &+ \oint_{f(\vec{y}, \tau)=0} \left[\frac{L_r}{r^2|D|} \right]_{\tau=t-\frac{r}{c_0}} dS(\vec{y}) \end{aligned} \quad (2.73)$$

where $\frac{1}{|D|}$ is the so-called Doppler factor:

$$D = 1 - M_r \quad (2.74)$$

$$M_r = v_i r_i / c_0, \quad r_i = x_i - y_i \quad (2.75)$$

where v_i is the local velocity component of the control surface, r_i is the vector component between the observation and source positions, and c_0 is the undisturbed sound speed.

An alternative to the FARASSAT's formulation I is to move the temporal derivative inside the integral, which is more robust for a moving control surface since taking the temporal derivative inside could prevent some instabilities [50]. This formulation of the integral FW-H equation is called FARASSAT's formulation II [21]:

$$Hp'(\vec{x}, t) = Hp_T'(\vec{x}, t) + Hp_L'(\vec{x}, t) \quad (2.76)$$

$$\begin{aligned} 4\pi p_T'(\vec{x}, t) &= \oint_{f(\vec{y}, \tau)=0} \left[\frac{\rho_0 (\dot{U}_n + U_{\dot{n}})}{rD^2} \right]_{\tau=t-\frac{r}{c_0}} dS(\vec{y}) \\ &+ \oint_{f(\vec{y}, \tau)=0} \left[\frac{\rho_0 U_n (r_i \dot{M}_i + c_0 (M_r - M^2))}{r^2 D^3} \right]_{\tau=t-\frac{r}{c_0}} dS(\vec{y}) \end{aligned} \quad (2.77)$$

$$\begin{aligned} 4\pi p_L'(\vec{x}, t) &= \frac{1}{c_0} \oint_{f(\vec{y}, \tau)=0} \left[\frac{\dot{L}_r}{rD^2} \right]_{\tau=t-\frac{r}{c_0}} dS(\vec{y}) \\ &+ \oint_{f(\vec{y}, \tau)=0} \left[\frac{L_r - L_M}{r^2 D^2} \right]_{\tau=t-\frac{r}{c_0}} dS(\vec{y}) \\ &+ \frac{1}{c_0} \oint_{f(\vec{y}, \tau)=0} \left[\frac{L_r (r \dot{M}_r + c_0 (M_r - M^2))}{r^2 D^3} \right]_{\tau=t-\frac{r}{c_0}} dS(\vec{y}) \end{aligned} \quad (2.78)$$

The source terms in FARASSAT's formulations I and II are defined as:

$$\dot{U}_n = \frac{\partial U_i}{\partial \tau} n_i \quad (2.79)$$

$$U_{\dot{n}} = v_i \frac{\partial n_i}{\partial \tau} \quad (2.80)$$

$$\dot{M}_i = \frac{1}{c_0} \frac{\partial v_i}{\partial \tau} \quad (2.81)$$

$$M^2 = \frac{v_i v_i}{c_0^2} \quad (2.82)$$

$$M_r = v_i r_i / c_0 \quad (2.83)$$

$$\dot{M}_r = \dot{M}_i \frac{r_i}{r} \quad (2.84)$$

$$L_r = L_i \frac{r_i}{r} \quad (2.85)$$

$$\dot{L}_r = \frac{\partial L_i}{\partial \tau} \frac{r_i}{r} \quad (2.86)$$

$$L_M = L_i \frac{v_i}{c_0} \quad (2.87)$$

For a stationary control surface, FARASSAT's formulation I reduces to:

$$4\pi p_T'(\vec{x}, t) = \frac{\partial}{\partial t} \oint_{f(\vec{y}, \tau)=0} \left[\frac{\rho_0 U_n}{r} \right]_{\tau=t-\frac{r}{c_0}} dS(\vec{y}) \quad (2.88)$$

$$4\pi p_L'(\vec{x}, t) = \frac{1}{c_0} \frac{\partial}{\partial t} \oint_{f(\vec{y}, \tau)=0} \left[\frac{L_r}{r} \right]_{\tau=t-\frac{r}{c_0}} dS(\vec{y}) \\ + \oint_{f(\vec{y}, \tau)=0} \left[\frac{L_r}{r^2} \right]_{\tau=t-\frac{r}{c_0}} dS(\vec{y}) \quad (2.89)$$

and FARASSAT's formulation II becomes:

$$4\pi p_T'(\vec{x}, t) = \oint_{f(\vec{y}, \tau)=0} \left[\frac{\rho_0 \dot{U}_n}{r} \right]_{\tau=t-\frac{r}{c_0}} dS(\vec{y}) \quad (2.90)$$

$$4\pi p_L'(\vec{x}, t) = \frac{1}{c_0} \oint_{f(\vec{y}, \tau)=0} \left[\frac{\dot{L}_r}{r} \right]_{\tau=t-\frac{r}{c_0}} dS(\vec{y}) \\ + \oint_{f(\vec{y}, \tau)=0} \left[\frac{L_r}{r^2} \right]_{\tau=t-\frac{r}{c_0}} dS(\vec{y}) \quad (2.91)$$

There are two very good reviews about the 3D FW-H approach by BRENTNER [10] (1998) and LYRINTZIS [50] (2002). All the 3D integral FW-H formulations introduced in this work, the equations 2.72, 2.73, 2.77, 2.78, 2.88, 2.89, 2.90, and 2.91, are also introduced and discussed at least in one of these two review articles.

2.2.3 2D Integral Formulations

Two-dimensional (2D) formulations have already been developed in recent years by GUO [32] and LOCARD [49]. These formulations of the FW-H equation not only provide a very efficient way for numerical implementation but also reveal explicitly the features of the source mechanisms and the characteristics of the far-field noise associated with 2D problems. The cylindrical spreading of 2D waves and their far-field directivity become apparent in these 2D formulations. The 2D formulation is numerically very efficient, because the domains of the integration are reduced by one from the three-dimensional (3D) formulation. The quadrupole integrals are now in a planar domain and the dipole and monopole integrals are along the contours of 2D bodies. The calculations of the retarded-time interpolation of the integrands, a time-consuming but necessary step in the three-dimensional formulation, are completely avoided by making use of Fourier transformation.

Under the assumptions of a compact source region and negligible interaction between sound and flow, the 2D formulation of integral formal solutions of the FW-H equation can be derived through GREEN's function method. But the 2D GREEN's functions are different from the 3D ones: the 2D GREEN's functions are in accordance with cylindrical wave spreading, and the 3D ones correspond to spherical wave spreading.

Formulation of GUO

GUO [32] used the following 2D free-space GREEN's function:

$$G(\vec{x} - \vec{y}; t - \tau) = \frac{c_0(t - \tau) - r}{2\pi c_0 \sqrt{c_0^2(t - \tau)^2 - r^2}} \quad (2.92)$$

$$r = |\vec{x} - \vec{y}| \quad (2.93)$$

where \vec{x} and \vec{y} are the observation position and source position respectively. This GREEN's function can be represented in the frequency space as:

$$G(\vec{x}, \vec{y}; \omega) = \frac{i}{8\pi} \int_{\omega} H_0^{(1)}(kr) e^{-i\omega(t-\tau)} d\omega \quad (2.94)$$

where H_0 denotes the zeroth-order Hankel function of first kind.

Symbolically, the solution of a 2D FW-H equation is:

$$p(\vec{x}, t) = \int_{\vec{y}} \int_{\tau} Q(\vec{y}, \tau) G(\vec{x} - \vec{y}; t - \tau) d^2\vec{y} d\tau \quad (2.95)$$

The following 2D formal solution of the FW-H equation in the frequency domain is derived by using equation 2.94 in equation 2.95 and the far-field condition:

$$\tilde{p}'(\vec{x}, \omega) = e^{ik|\vec{x}|} \left(\frac{1}{8i\pi k|\vec{x}|} \right)^{\frac{1}{2}} \left\{ -ik^2 \frac{x_i x_j}{|\vec{x}|^2} \int \int \tilde{T}_{ij}(\vec{y}, \omega_D) e^{-ik y_i \frac{x_i}{|\vec{x}|}} d^2\vec{y} \right.$$

$$\begin{aligned}
& + k \frac{x_i}{|\vec{x}|} \int n_j \tilde{P}_{ij}(\vec{y}, \omega_D) e^{-iky_i \frac{x_i}{|\vec{x}|}} dl \\
& + i \int \rho_0 n_i \tilde{u}_i(\vec{y}, \omega_D) e^{-iky_i \frac{x_i}{|\vec{x}|}} dl \} \quad (2.96)
\end{aligned}$$

where the tilde-superscripts denote a Fourier transformation defined as:

$$\tilde{f}(\vec{y}, \omega) = \int_{-\infty}^{+\infty} f(\vec{y}, \tau) e^{i\omega\tau} d\tau \quad (2.97)$$

and k is the wave number, ω_D is the Doppler shifted circular frequency, T_{ij} is the Lighthill's stress, P_{ij} is the surface stress, \dot{u}_i is the local acceleration of fluid, and N_i is the vector component of the outer normal of the control surface (namely control curve for 2D):

$$k = \frac{\omega}{c_0} \quad (2.98)$$

$$\omega_D = \omega \left(1 - \frac{v_i x_i}{c_0 |\vec{x}|} \right) \quad (2.99)$$

$$P_{ij} = (p - p_0) \delta_{ij} + \rho u_i (u_j - v_j) \quad (2.100)$$

$$\dot{u}_i = \frac{\partial u_i}{\partial \tau} \quad (2.101)$$

where v_i is the local velocity of the control surface. In the published paper of GUO [32], in the last term on the right side of equation 2.96 the imaginary sign, “ i ”, was omitted due to carelessness in print. Through the verification examples described in the next chapter, this mistake is found and corrected.

For the porous FW-H approach, only the curve integrations in the above equation 2.96 are necessary if the control surface is large enough to enclose all the quadrupole sources.

The acoustic pressure, $p'(\vec{x}, t)$, in the time-domain can be calculated through the following inverse Fourier transformation from $\tilde{p}'(\vec{x}, \omega)$:

$$f(\vec{x}, t) = \int_{-\infty}^{+\infty} \tilde{f}(\vec{x}, \omega) e^{-i\omega t} d\omega \quad (2.102)$$

Formulation of LOCARD

LOCARD [49] used the following GREEN's function in the frequency domain for a uniform mean flow space:

$$G(\vec{x}, \vec{y}; \omega) = \frac{i}{4\beta} e^{Mk\bar{\xi}/\beta^2} H_0^{(2)} \left(\frac{k}{\beta^2} \sqrt{\bar{\xi}^2 + \beta^2 \bar{\eta}^2} \right) \quad (2.103)$$

$$\bar{\xi} = (x_1 - y_1) \cos \theta + (x_2 - y_2) \sin \theta \quad (2.104)$$

$$\bar{\eta} = -(x_1 - y_1) \sin \theta + (x_2 - y_2) \cos \theta \quad (2.105)$$

$$\tan \theta = V/U \quad (2.106)$$

where k denotes the wave number: $k = \omega/c_0$; β is the PRANDTL number: $\beta = \sqrt{1 - M^2}$, $M = \sqrt{U_1^2 + U_2^2}/c_0$; (U_1, U_2) is the uniform velocity of mean flow.

Then the following 2D formal solution of the FW-H equation can be derived:

$$Hp'(\vec{x}, \omega) = Hp_Q'(\vec{x}, \omega) + Hp_L'(\vec{x}, \omega) + Hp_T'(\vec{x}, \omega) \quad (2.107)$$

$$Hp_Q'(\vec{x}, \omega) = - \oint_{f>0} \tilde{T}_{ij}(\vec{y}, \omega) H \frac{\partial^2 G(\vec{x}; \vec{y})}{\partial y_i \partial y_j} d\vec{y}^2 \quad (2.108)$$

$$Hp_L'(\vec{x}, \omega) = - \oint_{f=0} \tilde{F}_i(\vec{y}, \omega) \frac{\partial G(\vec{x}; \vec{y})}{\partial y_i} dl \quad (2.109)$$

$$Hp_T'(\vec{x}, \omega) = - \oint_{f=0} i\omega \tilde{Q}(\vec{y}, \omega) G(\vec{x}; \vec{y}) dl \quad (2.110)$$

$$F_i(\vec{y}, \tau) = [(p - p_0)\delta_{ij} + \rho(u_i - U_i)(u_j + U_j) + \rho_0 U_i U_j] n_j \quad (2.111)$$

$$Q(\vec{y}, \tau) = [\rho(u_i + U_i) - \rho_0 U_i] n_i \quad (2.112)$$

where H is the Heaviside function, u_i is the local flow velocity, U_i is the uniform velocity of mean flow, and the first and second derivatives of the GREEN's function can be calculated analytically. For the porous FW-H approach used in this work, only the first derivatives are required, because the quadrupole sound pressure, Hp_Q' , is not required to be resolved. The required first derivatives are calculated as:

$$\frac{\partial G(\vec{x}; \vec{y})}{\partial y_1} = -A(r_1) \left[\frac{iMk}{\beta^2} H_0^{(2)} \left(\frac{kr_\beta}{\beta^2} \right) - \frac{k}{\beta^2} \frac{r_1}{r_\beta} H_1^{(2)} \left(\frac{kr_\beta}{\beta^2} \right) \right] \quad (2.113)$$

$$\frac{\partial G(\vec{x}; \vec{y})}{\partial y_2} = A(r_1) \left[\frac{kr_2}{r_\beta} H_1^{(2)} \left(\frac{kr_\beta}{\beta^2} \right) \right] \quad (2.114)$$

where $r_i = x_i - y_i$, and $A(r_1) = \frac{i}{4\beta} \exp(\frac{iMkr_1}{\beta^2})$. $H_k^{(n)}$ denotes a HANKEL function of the n th kind and the k th order.

The governing equations for the LOCARD approach, 2.107 to 2.114, were first derived by LOCARD [49] and applied to cavity flow noise by GLOERFELT [31].

The 3D formulation II of FARASSAT, 2D formulation of GUO and 2D formulation of LOCARD have been implemented as a computer program used to carry out the second step of the hybrid CFD/CAA simulations in this work. The implemented approximations for the numerical solution are described in the next chapter.

Chapter 3

Numerical Approaches

In this chapter, the numerical algorithms, namely spatial and temporal discretization and approximation, for the near-field CFD simulation and far-field acoustical simulation are presented. The details of the numerical approaches of the CFD-solver, SPARC, can also be seen in the PhD theses of FRANKE [28] and that of ALKEN [1]. The data coupling methods between the CFD simulation and the acoustical solver, namely the averaging and copying of the source information on the control surface and the searching of the retarded time, are also presented.

The accuracy and efficiency of the aeroacoustic prediction depends on both the correctness of the input data of the dynamic near-field and the numerical approach for acoustic integrals from the near-field to the acoustic far-field. The aeroacoustic prediction is in the form of vibrated small disturbances. The directivity patterns of the acoustic far-field are not so sensitive, but the acoustic pulse amplitudes, the peak values in the acoustic spectrum, are very sensitive and may vary more than 3 dB among different numerical treatments of the acoustic integrals with the same input data of the near-field. The practical formulations and numerical implementations of the acoustic integrals based on the (porous) FW-H approach have to be carefully chosen, and the effects of different formulations and numerical implementations should be given sufficient attention. The consideration and optimization of the numerical implementation of the acoustic integrals can improve the accuracy, efficiency and robustness of the aeroacoustic predictions. The different integral formulations of FW-H have been already discussed analytically in the previous chapter. In this chapter, the details of numerical implementations of the chosen formulations of FARASSAT, GUO and LOCARD will be given and discussed.

3.1 Near-field CFD

3.1.1 Space Discretization: Finite-Volume-Method

The NS equations shown in section 2.1 of chapter 2 are solved by a cell centered Finite Volumes Method (FVM). The FVM uses the integral conservation form of the NS equations as the starting point. This form of the NS equations can be written as:

The continuity equation:

$$\frac{\partial}{\partial t} \int_V \rho dV + \int_S \rho u_k n_k dS = 0 \quad (3.1)$$

The momentum equations:

$$\frac{\partial}{\partial t} \int_V \rho u_i dV + \int_S \rho u_i (u_k n_k) dS - \int_S (\tau_{ij} n_j - p n_i) dS = 0 \quad (3.2)$$

The energy equation:

$$\frac{\partial}{\partial t} \int_V \rho E dV + \int_S \rho E (u_k n_k) dS - \int_S [\tau_{ij} (u_i n_j) - p (u_k n_k)] dS - \int_S q_k n_k dS = 0 \quad (3.3)$$

where V denotes the control volume and S denotes the surface of the control volume. Through the FVM, the solution domain is subdivided into a finite number of small control volumes (CVs). In one such CV, the above equations are spatially discretised to the following equations:

The continuity equation:

$$\frac{\partial}{\partial t} [{}^v \bar{\rho} V(t)] + \sum_{l=1}^6 S_k^l(t) ({}^l \bar{\rho} u_k - {}^l \bar{\rho} v_k) = 0 \quad (3.4)$$

The momentum equations:

$$\frac{\partial}{\partial t} [{}^v \bar{\rho} u_i V(t)] + \sum_{l=1}^6 S_k^l(t) ({}^l \bar{u}_k \bar{\rho} u_i - {}^l \bar{v}_k \bar{\rho} u_i) - \sum_{l=1}^6 S_j^l(t) ({}^l \bar{\tau}_{ij} - {}^l \bar{p} \delta_{ij}) = 0 \quad (3.5)$$

The energy equation:

$$\frac{\partial}{\partial t} [{}^v \bar{\rho} E V(t)] + \sum_{l=1}^6 S_k^l(t) ({}^l \bar{u}_k \bar{\rho} E - {}^l \bar{v}_k \bar{\rho} E) - \sum_{l=1}^6 S_j^l(t) ({}^l \bar{\tau}_{ij} u_i - {}^l \bar{p} \delta_{ij}) + \sum_{l=1}^6 S_k^l(t) {}^l \bar{q}_k = 0 \quad (3.6)$$

where v_k denotes the velocity of the control surface constituting the control volume which is assumed to be constant on a such surface. The bar-superscript with v denotes the average value for the control volume 'v', and the bar-superscript with l denotes the average value for the control surface 'l'. ${}^l\bar{\tau}_{ij}$, ${}^l\bar{q}_k$ and ${}^l\bar{p}$ are calculated as follows:

$${}^l\bar{\tau}_{ij} = {}^l\overline{\mu S_{ij}} \quad (3.7)$$

$$S_{ij} = \frac{\partial u_i}{\partial x_j} + \frac{\partial u_j}{\partial x_i} - \frac{2}{3} \frac{\partial u_k}{\partial x_k} \delta_{ij} \quad (3.8)$$

$${}^l\bar{p} = R {}^l\overline{\rho\theta} \quad (3.9)$$

$${}^l\bar{q}_k = -\frac{C_p}{Pr} \mu {}^l\overline{\frac{\partial\theta}{\partial x_k}} \quad (3.10)$$

In order to obtain a closed equation system, the following equation is needed:

$${}^v\bar{p} = (\gamma - 1) \left({}^v\overline{\rho E} - \frac{1}{2} {}^v\overline{\rho u_k u_k} \right) \quad (3.11)$$

For the DNS approach, the following equation system can be derived:

$$\frac{\partial}{\partial t} [({}^v\tilde{w})(t)V(t)] = (f)_c(t) + (f)_d(t) \quad (3.12)$$

And for the LES approach, one term, namely $(f)_m(t)$, more than that for the DNS approach is needed:

$$\frac{\partial}{\partial t} [({}^v\tilde{w})(t)V(t)] = (f)_c(t) + (f)_d(t) + (f)_m(t) \quad (3.13)$$

where the conservative solution variables, $({}^v\tilde{w})(t)$, the convective flux, $(f)_c(t)$, diffusive flux, $(f)_d(t)$, and subgrid flux, $(f)_m(t)$, are defined as follows:

$$({}^v\tilde{w})(t) = \begin{pmatrix} {}^v\bar{\rho}(t) \\ {}^v\overline{\rho u_1}(t) \\ {}^v\overline{\rho u_2}(t) \\ {}^v\overline{\rho u_3}(t) \\ {}^v\bar{\rho}(t) \quad {}^v\tilde{E}(t) \end{pmatrix} \quad (3.14)$$

$$(f)_c(t) = -\sum_{l=1}^6 S_k^l(t) [\tilde{u}_k(t) - v_k(t)] \begin{pmatrix} \bar{\rho}(t) \\ \overline{\rho u_1}(t) \\ \overline{\rho u_2}(t) \\ \overline{\rho u_3}(t) \\ \bar{\rho}(t) \tilde{E}(t) \end{pmatrix} \quad (3.15)$$

$$(f)_d(t) = \sum_{l=1}^6 S_k^l(t) \begin{pmatrix} 0 \\ \tilde{\tau}_{k1}(t) - \bar{p}(t)\delta_{k1} \\ \tilde{\tau}_{k2}(t) - \bar{p}(t)\delta_{k2} \\ \tilde{\tau}_{k3}(t) - \bar{p}(t)\delta_{k3} \\ [\tilde{\tau}_{ij}(t) - \bar{p}(t)\delta_{ij}] \tilde{u}_i(t) + \tilde{\kappa}(t) \frac{\partial\tilde{\theta}(t)}{\partial x_k} \end{pmatrix} \quad (3.16)$$

$$(f)_m(t) = \sum_{l=1}^6 S_k^l(t) \begin{pmatrix} 0 \\ 2\tilde{\mu}_{SGS}(t)\tilde{S}_{k1}(t) \\ 2\tilde{\mu}_{SGS}(t)\tilde{S}_{k2}(t) \\ 2\tilde{\mu}_{SGS}(t)\tilde{S}_{k3}(t) \\ [\tilde{\tau}_{ij}(t) - \bar{p}(t)\delta_{ij}] \tilde{u}_i(t) + \tilde{\kappa} \frac{\partial \tilde{\theta}(t)}{\partial x_k} \end{pmatrix} \quad (3.17)$$

All the surface integrals for the flux terms are approximated by the midpoint rule with a second order accuracy. The numerical treatments for these flux terms are as follows:

Convective Flux $(f)_c(t)$:

For the convective terms, $(f)_c(t)$, the high resolution scheme of JAMESON, which is developed by JAMESON, SCHMIDT and TURKEL [39] for the solver of EULER equations, has been applied in the formulation of MARTINELLI [56]. This scheme is a central scheme of the second order supplemented with an artificial viscosity term, consisting of second or fourth order viscosity, and switching between these two accuracy artificial viscosities on the dependence of the local discontinuities. While the second order term is only activated when a shock is detected, which is not the case for the flow studied here, the fourth order viscosity serves as a background dissipation to suppress odd-even decoupling. The magnitude of this artificial viscosity term is controlled by a factor which is normally set to 1/64 for the computation of steady flows. But in the aeroacoustic simulation, this factor is reduced to $7.8125 \cdot 10^{-5}$ to keep the dissipation character of this scheme as small as possible.

Diffusive Flux $(f)_d(t)$:

The viscous fluxes, $(f)_d(t)$, are also obtained from numerical integration using the midpoint rule. The values of the Cartesian components of the pressure stress tensor, $P_{ij} = \tau_{ij} - p\delta_{ij}$, and the heat flux vector in the centers of the CV surfaces are obtained in the following way: (1)The gradients of the velocity components and the temperature are calculated at the four vertices of the face, with the aid of an auxiliary control volume constructed around the vertices and using the Gauss elimination method. (2)The Cartesian components of the pressure stress tensor and heat flux vector are calculated at the vertices through these gradients. The dynamic and subgrid scale viscosities needed at the vertices are linearly interpolated from the cell centers, where they are calculated. The components of the pressure stress tensor and heat flux vector on the center point of the surface are finally obtained by arithmetically averaging the four values at the vertices.

Subgrid Flux $(f)_m(t)$:

While the dynamic viscosity is directly computed from the temperature in the CV, the subgrid scale viscosity depends on the derivatoric part of the deformation tensor: $\nu_{SGS} = (C_s \bar{\Delta})^2 \sqrt{2\tilde{S}_{ij}\tilde{S}_{ij}}$. There are two subgrid stresses leading to the subgrid scale fluxes: (1) at the central points of the CV surfaces, which is calculated by the above

method described for the diffusive flux. (2)at the CV center, which is calculated by approximating the velocity gradients with central differences at the CV center.

3.1.2 Temporal Discretization: Explicit RK-Method

A stable time stepping method, namely the explicit RUNGE-KUTTA-Method is used. If the cell volume, V_{ijk} , is independent of time, the semi-discretised NS equations can be written as:

$$\frac{\partial w}{\partial t} + R(w) = 0 \quad (3.18)$$

where $R(w)$ is the residual.

Let $w^{(n)}$ be the value of the solution variable w after n time steps. The general m stage hybrid scheme to advance a time step, Δt , can be written as:

$$\begin{aligned} w^{(0)} &= w^{(n)} \\ w^{(1)} &= w^{(0)} - \alpha_1 \Delta t R^{(0)} \\ &\vdots \\ w^{(m-1)} &= w^{(0)} - \alpha_{m-1} \Delta t R^{(m-2)} \\ w^{(m)} &= w^{(0)} - \alpha_m \Delta t R^{(m-1)} \\ w^{(n+1)} &= w^{(m)} \end{aligned} \quad (3.19)$$

where appropriate coefficients, α_m , can extend the stability region, and $n=3$ or 4 are used, namely 3-stage or 4-stage explicit Runge-Kutta-Method with 3rd or 4th order accuracy. The temporal interval, Δt , is calculated through the COURANT, FRIEDRICHS and LEVY (CFL) number. In the current work, the CFL number is chosen as 2.2 for the laminar flow, and 1.0 for the turbulent flow.

3.1.3 Boundary Conditions

There are six primitive variable components: the velocity vector, u_i ($i=1,2,3$), density, ρ , temperature, θ , and pressure p . To implement the boundary conditions into the computer program, ghost CVs are used. The boundary surface is the surface between the CV in the solution domain and the first ghost CV. Setting the boundary condition on the boundary surface of the solution domain is achieved through setting the solution variables in the ghost CV. There are five solution variables: ρ , ρu_i , and ρE , whose boundary values are required to be settled.

The following boundary conditions are used:

Solid Wall

The condition of no slip for viscous flow is imposed by setting the flow velocity to the same as that for the solid surface.

$$u_i = u_{wi} \quad (3.20)$$

The solid wall is isothermal:

$$\theta_w = \text{const.} \quad (3.21)$$

There is no pressure gradient in the normal direction on the wall:

$$\frac{\partial p}{\partial n}|_w = 0 \quad (3.22)$$

And the density is calculated through the state equation of the ideal gas:

$$\rho_w = \frac{p_w}{R\theta_w} \quad (3.23)$$

where the subscript 'w' denotes the value on the solid wall surface.

The values of solution variables of the first ghost CV are:

$$\bar{\rho}_g = 2\frac{\bar{p}_1}{R\theta_w} - \bar{\rho}_1 \quad (3.24)$$

$$(\bar{\rho}\tilde{u}_i)_g = -(\bar{\rho}\tilde{u}_i)_1 \quad (3.25)$$

$$(\bar{\rho}\tilde{E})_g = \frac{\bar{p}_g}{\gamma - 1} + \frac{1}{2}\bar{\rho}_g(\tilde{u}_i)_g(\tilde{u}_i)_g \quad (3.26)$$

where the subscript 'g' denotes the first ghost CV, the subscript '1' denotes the nearby CV in the solution domain, and the subscript 'w' denotes the wall surface.

Pressure Outlet

This boundary condition is used for the outlet boundary, where the static pressure distribution, \bar{p}_b , is assumed to be known. The values of the solution variables of the first ghost CV are:

$$\bar{\rho}_g = \bar{\rho}_1 \quad (3.27)$$

$$(\bar{\rho}\tilde{u}_i)_g = (\bar{\rho}\tilde{u}_i)_1 \quad (3.28)$$

$$(\bar{\rho}\tilde{E})_g = \frac{\bar{p}_b}{\gamma - 1} + \frac{1}{2}\bar{\rho}_g(\tilde{u}_i)_g(\tilde{u}_i)_g \quad (3.29)$$

where the subscript 'g' denotes the first ghost CV, the subscript '1' denotes the nearby CV in the solution domain, and the subscript 'b' denotes the boundary surface.

Far-field

The far field boundary condition is a numerical treatment to limit the computational domain. This boundary condition is used for the external boundaries of the computational domain, where the compatibility relations associated with the acoustic waves are fulfilled, namely where the outgoing information goes out and ingoing information comes in, without the resistance from the boundary condition.

The five solution variables in the computation ($\bar{\rho}$, $\bar{\rho}\tilde{u}_i$, $\bar{\rho}\tilde{E}$) are specified on the boundary through the Riemann invariants, R_{nb}^+ and R_{nb}^- , and the tangential velocity component on the boundary surface, $\vec{V}_{t\infty}$, of the free-stream. The subsonic far field boundary condition contains two parts: the inflow conditions and the outflow conditions.

The density on the boundary, $\bar{\rho}_b$, is calculated as:

$$\bar{\rho}_b = \left(\frac{\tilde{s}_b c_b^2}{\gamma} \right)^{\frac{1}{\gamma-1}} \quad (3.30)$$

where the entropy, \tilde{s}_b , and the sound speed, c_b , are calculated as:

$$\tilde{s}_b = \tilde{s}_{in/out} = \tilde{s}_{\infty/I} = \frac{\bar{p}_{\infty/I}^\gamma}{p_{\infty/I}} \quad (3.31)$$

$$c_b = \frac{\gamma-1}{4} (R_{nb}^+ - R_{nb}^-) \quad (3.32)$$

where R_{nb}^+ and R_{nb}^- are the RIEMANN invariants, which are calculated as:

$$R_{nb}^+ = -|V_{n\infty}| + \frac{2\bar{c}_{\infty}}{\gamma-1} \quad (3.33)$$

$$R_{nb}^- = |V_{nI}| - \frac{2\bar{c}_I}{\gamma-1} \quad (3.34)$$

$$\bar{c}_{\infty/I} = \sqrt{\gamma R \tilde{\theta}_{\infty/I}} \quad (3.35)$$

where the subscript ' ∞ ' denotes the free stream value, and the subscript 'I' refers to a value at an internal mesh point along the outer normal direction of the boundary surface which is denoted with the subscript 'n'.

Then the boundary values of the velocity component along the normal direction of the boundary surface, V_{nb} , can be calculated as:

$$V_{nb} = \frac{R_{nb}^+ + R_{nb}^-}{2} \quad (3.36)$$

The boundary values of the velocity component along the tangential direction of the boundary surface, V_{tb} , are associated to the physical free-stream values:

$$V_{tb} = V_{t\infty} \quad (3.37)$$

Therefore the three components of the velocity boundary values, $(\tilde{u}_i)_b$, are calculated as:

$$(\tilde{u}_1)_b \vec{i} + (\tilde{u}_2)_b \vec{j} + (\tilde{u}_3)_b \vec{k} = V_{nb} \vec{n}_b + V_{tb} \vec{t}_b \quad (3.38)$$

where the \vec{i} , \vec{j} , and \vec{k} are the unit direction vectors of a CARTESIAN frame. The \vec{n}_b and \vec{n}_t are the outer normal and tangential direction vectors of the boundary surface respectively.

The energy density on the boundary, $(\bar{\rho}\tilde{E})_b$, is calculated as:

$$(\bar{\rho}\tilde{E})_b = \frac{\bar{p}_b}{\gamma - 1} + \frac{1}{2}\bar{\rho}_b(\tilde{u}_i)_{\infty/I}(\tilde{u}_i)_{\infty/I} \quad (3.39)$$

$$\bar{p}_b = \frac{\bar{\rho}_{\infty/I}c_b^2}{\gamma} \quad (3.40)$$

Periodic

This boundary condition is used between two external boundary surfaces, where the flow quantities are the same. The values of solution variables of the first ghost CV are:

$$\bar{\rho}_g = \bar{\rho}_b \quad (3.41)$$

$$(\bar{\rho}\tilde{u}_i)_g = (\bar{\rho}\tilde{u}_i)_b \quad (3.42)$$

$$(\bar{\rho}\tilde{E})_g = (\bar{\rho}\tilde{E})_b \quad (3.43)$$

3.2 Far-field CAA

The integral method based on the permeable (porous) surface FW-H equation allows the acoustic pressure signal to be calculated by the quantities on the porous control surface provided by a CFD code. For three dimensional aeroacoustical generation and propagation, the integral form can be written as two formulations – the formulation I: the time derivation outside the integral which is good for a stationary control surface; the formulation II: the time integral inside the integral which is also good for a moving control surface. There are two methods to treat the relationship between the source and observation time of the integral form: retarded and forward time. The retarded time method is chosen for the subsonic aeroacoustic computation in this dissertation. For the two dimensional problems, namely the cylindrical spreading acoustic waves, the FOURIER transformed formulation based on a two dimensional Green function is much more efficient and reveals explicitly the source mechanisms and characteristics of the acoustic far-field. The numeric schemes of the three and two dimensional integral extension from the CFD near-field data to the acoustic far-field are described in this section.

3.2.1 Coupling between CFD and Aeroacoustic Solver

The required aeroacoustic source information on the control surface is calculated by the CFD solver at the first step. For the turbulent cases, such kinds of time-dependent source information are very computationally expensive. Making the computational domain as

small as possible is a good way to reduce the computational costs. In the dynamical near field, fortunately, the periodicity of the aeroacoustic source terms exists in the span direction for the flow around a cylindrical structure. Therefore, in practice, the unsteady CFD (LES or DNS) is only carried out with a relative small span length, L_z , of the cylindrical structure. In such cases, the input for the aeroacoustic solver has to be manipulated to meet the acoustic laws. In this work, 2D and 3D formulations of the integral extension based on the FW-H equation are implemented in the aeroacoustic solver. There are two ways to manipulate the aeroacoustic source information calculated by the CFD solver in order to meet the requirement of the aeroacoustic solver, which are shown in figure 3.1:

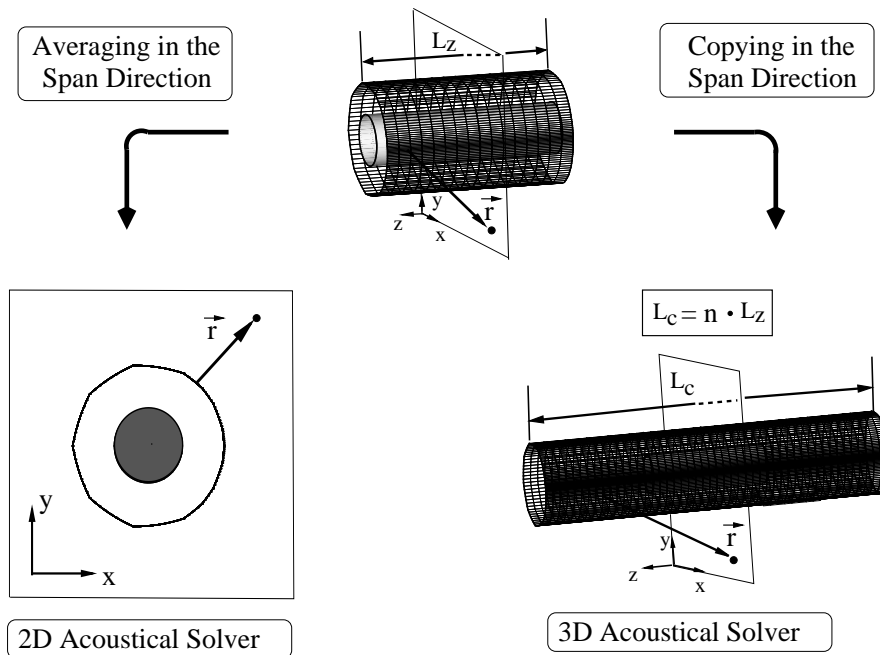


Figure 3.1: Coupling between CFD and Aeroacoustic Solver

In figure 3.1, L_z denotes the span length of the CFD domain, and L_c denotes the span length of the cylindrical control surface for the 3D acoustic solver. In this work, L_c is also called the copy length. This is due to the fact that L_c is the span length after a number of copies of source information of the span length L_z calculated by CFD. A spatial averaging in the span direction is carried out to obtain the input for the 2D acoustic solver.

3.2.2 3D Integral Extension

The FARASSAT's 3D formulations (see equations 2.77 and 2.78) are chosen for the three dimensional cases, i.e. with the time derivation inside the integral. And the retarded time approach is chosen to calculate the relationship between the source and observation

time. The quadrature on the control surface, the interpolation at retarded-time, and the temporal derivation of source terms are required and compose the main algorithms. The general mathematical form of the integrals is:

$$4\pi\phi(\vec{x}, t) = \int \int_{[f]_{ret=0}} \left[\frac{Q(\vec{y}, \tau)}{4\pi r^{N_1} |1 - M_r|^{N_2}} \right]_{ret} dS(\vec{y}) \quad (3.44)$$

where Q is the known source strength, which is a function of the source position and time, (\vec{y}, τ) ; N_1 and N_2 are integers. Normally the predicted acoustic pressure, $p'(\vec{x}, t)$, is a sum of these types of integrals based on a series of source terms. The interpretation of the above general retarded-time formulation is easy to understand, which means that the integration occurs over the control surface chosen, with the integrand evaluated at the emission, or retarded time, $\tau = t - r/c_0$. Note that this formulation requires that the observation position and time, (\vec{x}, t) , are fixed during the evaluation of the integral. Therefore the total computation consists of three loops, in which the outer two loops are over all the observation positions and times, and the inner loop is over all the source positions on the control surface chosen. Numerical implementation of this formula is very robust and efficient and commonly used for the aeroacoustic prediction of subsonic flows.

The retarded-time integral can be approximated with the method of midpanel quadrature as following:

$$4\pi\phi(\vec{x}, t) \approx \sum_{m=1}^M \frac{Q_m(\vec{y}_{mc}, t - r_{mc}/c_0)}{[r_{mc}^{N_1} |1 - M_r|^{N_2}]_{ret}} \Delta S_m \quad (3.45)$$

Here, the control surface, S , is divided into M panels, and the integrand is evaluated at the center of each panel, \vec{y}_{mc} , and at the retarded time of this center point, $\tau_{mc} = t - r_{mc}/c_0$, ($r_{mc} = |\vec{x} - \vec{y}_{mc}|$). If the source is in motion, the source position is a function of retarded time, $\vec{y}_{mc}(\tau)$, but unless the source motion is simple, the retarded time cannot be determined explicitly. Even when the source motion is complex, such as the motion of a helicopter main rotor, the retarded time can be found numerically as the root of the equation $t - \tau - r_{mc}(\tau)/c_0 = 0$, with a standard root-finding algorithm. Because the source strength, Q_m , is evaluated at the retarded time of the center of the panel, temporal interpolations of the input data are required. After the two outer loops of all the required observation positions and times, the time histories of the acoustic pressures at every observation point can be calculated, whether the observation points are also in motion, or not.

The accuracy of the above algorithm can be improved by replacing the single point evaluation of the integrand at the panel center with multi-point methods as the following:

$$4\pi\phi(\vec{x}, t) \approx \sum_{m=1}^M \left\{ \sum_{i=1}^{M_i} \alpha_i \frac{Q(\vec{y}_i, t - r_i/c_0)}{[r_i^{N_1} |1 - M_r|^{N_2}]_{ret}} |J|_i \right\} \Delta S_m \quad (3.46)$$

$$M_i(M_r, \Delta S_m) \propto \frac{\Delta S_m}{|1 - M_r|_i^{N_2}} \quad (3.47)$$

where α_i and $|J|_i$ are the quadrature weight coefficient and determinant of the Jacobian of the transformation, respectively, for the i^{th} point in the panel quadrature algorithm. The full benefit of a high-accuracy quadrature can be realized when a solution-adaptive quadrature scheme is utilized. This adaptive method is by means of selecting the number of quadrature points, M_i , used for m^{th} panel with some parameters related to the integrand, which means, a larger number of quadrature points are used only when the integrand variation over the panel requires them. An adaptive-quadrature scheme can provide high accuracy and minimize the computational effort.

According to the above approach, the detailed numerical schemes are described as follows:

(1) Choice of control surface:

For a porous FW-H formulation, the results are not sensitive to the choice of the control surface when the spatial resolutions and the impact of the numerical boundary conditions are at the same accuracy level. The choice of the control surface for the porous FW-H approach is flexible and robust. One can even use an open control surface or a control surface with a part solid, part porous surface.

(2) Quadrature:

As an example, the spatial discretization of a cylindrical control surface is shown in figure 3.2 (page 41). The surface integration over the control surface is numerically the sum of the integrations on the panels. The integration on each panel is numerically carried out with the 2nd order midpanel quadrature or the 4th order SIMPSON's quadrature in this work. For the midpanel quadrature on the panel m , the source information on the central point 'mc' are required; as well as for the SIMPSON's quadrature on the same panel, the source information on nine points, namely, $m1, m2, \dots, m8$ and mc , are required. The SIMPSON's quadrature is more accurate but computationally expensive. Usually an adaptive multi-point quadrature is recommended: the midpanel quadrature approximation is used in non-sensitive regions, and the SIMPSON's is only used in sensitive regions on the control surface. The general formations of the numerical quadratures have been shown in equations 3.45 and 3.46. The details of the midpanel and SIMPSON's quadrature used in this work are presented as follows:

Under the midpanel quadrature approximation, the general numeric discrete formation of the quadrature is:

$$\sum_{m=1}^M Q(\vec{y}_{mc}, t_n - r_{mc}/c_0) \Delta S_m \quad (3.48)$$

where t_n denotes one observation time, and:

$$\vec{y}_{mc} = 0.25(\vec{y}_{m1} + \vec{y}_{m2} + \vec{y}_{m3} + \vec{y}_{m4}) \quad (3.49)$$

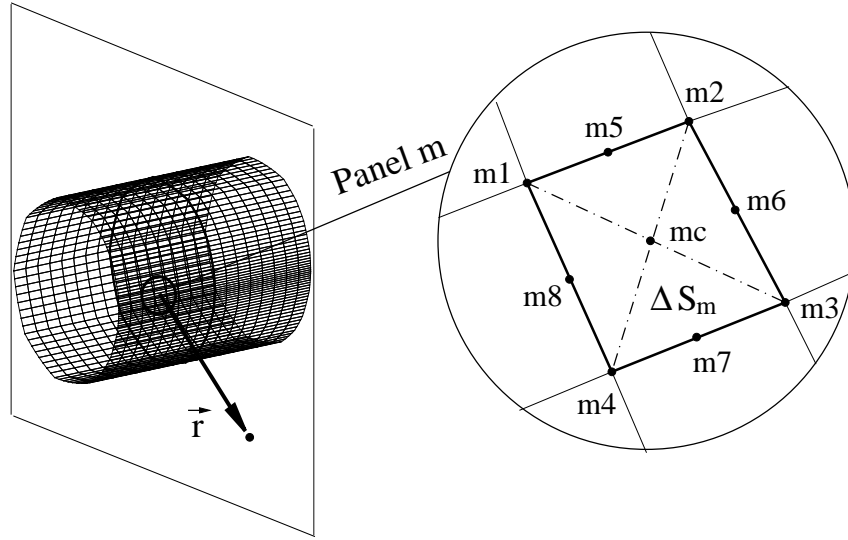


Figure 3.2: The Spatial Discretion of Control Surface

$$r_{mc} = |\vec{x} - \vec{y}_{mc}| \quad (3.50)$$

where \vec{x} denotes the observation position.

Under the SIMPSON's quadrature approximation, the general numeric discrete formation of the quadrature is:

$$\sum_{m=1}^M \sum_{i=1}^9 \alpha_i Q(\vec{y}_{mi}, t_n - r_{mi}/c_0) \frac{\Delta S_m}{\sum_{i=1}^9 \alpha_i} \quad (3.51)$$

where t_n denotes one observation time, and:

$\vec{y}_{m1}, \vec{y}_{m2}, \vec{y}_{m3}, \vec{y}_{m4}$: Corner Positions of the Quadrilateral Panel

$$\vec{y}_{m5} = \frac{1}{2} (\vec{y}_{m1} + \vec{y}_{m2}) \quad (3.52)$$

$$\vec{y}_{m6} = \frac{1}{2} (\vec{y}_{m2} + \vec{y}_{m3}) \quad (3.53)$$

$$\vec{y}_{m7} = \frac{1}{2} (\vec{y}_{m3} + \vec{y}_{m4}) \quad (3.54)$$

$$\vec{y}_{m8} = \frac{1}{2} (\vec{y}_{m4} + \vec{y}_{m1}) \quad (3.55)$$

$$\begin{aligned} \vec{y}_{m9} &= \vec{y}_{mc} \\ &= \frac{1}{4} (\vec{y}_{m1} + \vec{y}_{m2} + \vec{y}_{m3} + \vec{y}_{m4}) \end{aligned} \quad (3.56)$$

$$\alpha_1 = \alpha_2 = \alpha_3 = \alpha_4 = 1 \quad (3.57)$$

$$\alpha_5 = \alpha_6 = \alpha_7 = \alpha_8 = 4 \quad (3.58)$$

$$\alpha_9 = 16 \quad (3.59)$$

$$r_{mi} = |\vec{x} - \vec{y}_{mi}| \quad (3.60)$$

where \vec{x} denotes the observation positions.

(3) Interpolation and Temporal Derivation at Retarded-time:

In the general formulations of equations 3.48 and 3.51, the integrand $Q(\vec{y}_{mi}, \tau_n)$ ($\tau_n = t_n - r_{mi}/c_0$) is calculated through the interpolation with the values of $Q(\vec{y}_{mi}, \tau_m)$ ($m = m_1, \dots, m_2$), where τ_m is the source time calculated by the CFD. In general, $\tau_n \neq \tau_m$. Moreover, the source information stored in the data base as the inputs for the acoustic solver are the time histories of density, ρ , flow velocity, u_i and pressure, p . To calculate the surface integrations shown in equations 2.77 and 2.78, temporal derivations are required for the calculations of \dot{L}_i , \dot{U}_i and \dot{M}_i based on the inputs of ρ , u_i and p . The second and fourth order non-equidistant interpolations and derivations are used in this work. In figure 3.3, the interpolation from the source time, τ_m , calculated by the CFD, to the source time, τ_n , required by the acoustic integrals, is sketched.

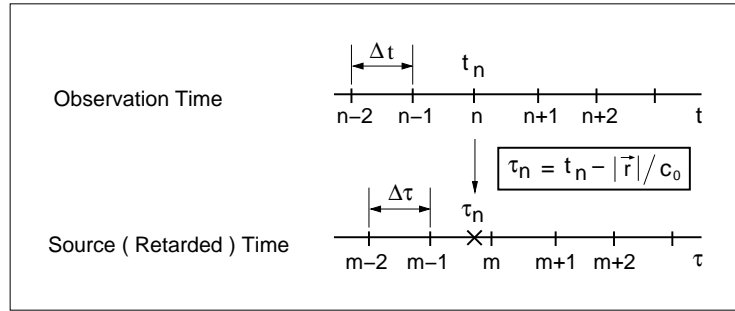


Figure 3.3: Non-equidistant Interpolation at the Source (Retarded) Time

The 2nd order linear temporal interpolation from τ_m to τ_n has the following general form:

$$\Phi(\tau_n) = \Phi(\tau_m) \frac{\tau_n - \tau_{m-1}}{\tau_m - \tau_{m-1}} + \Phi(\tau_{m-1}) \frac{\tau_m - \tau_n}{\tau_m - \tau_{m-1}} \quad (3.61)$$

The 2nd order temporal derivation at τ_n has the following general form:

$$\left(\frac{\partial \Phi}{\partial \tau} \right)_n = \frac{\Phi_m(\tau_n - \tau_{m-1})^2 - \Phi_{m-1}(\tau_m - \tau_n)^2}{(\tau_m - \tau_n)(\tau_n - \tau_{m-1})(\tau_m - \tau_{m-1})} + \frac{\Phi_n [(\tau_m - \tau_n)^2 - (\tau_n - \tau_{m-1})^2]}{(\tau_m - \tau_n)(\tau_n - \tau_{m-1})(\tau_m - \tau_{m-1})} \quad (3.62)$$

The 4th order temporal interpolation from τ_m to τ_n is calculated with the polynomial development as follows:

$$\Phi(\tau_n) = a_0 + a_1\tau_n + a_2\tau_n^2 + a_3\tau_n^3 \quad (3.63)$$

$$\Delta = \begin{vmatrix} 1 & \tau_{i-1} & \tau_{i-1}^2 & \tau_{i-1}^3 \\ 1 & \tau_i & \tau_i^2 & \tau_i^3 \\ 1 & \tau_{i+1} & \tau_{i+1}^2 & \tau_{i+1}^3 \\ 1 & \tau_{i+2} & \tau_{i+2}^2 & \tau_{i+2}^3 \end{vmatrix}$$

$$= 12 (\Delta\tau)^6 \quad (3.64)$$

$$\begin{aligned} \Delta_0 &= \begin{vmatrix} \Phi_{i-1} & \tau_{i-1} & \tau_{i-1}^2 & \tau_{i-1}^3 \\ \Phi_i & \tau_i & \tau_i^2 & \tau_i^3 \\ \Phi_{i+1} & \tau_{i+1} & \tau_{i+1}^2 & \tau_{i+1}^3 \\ \Phi_{i+2} & \tau_{i+2} & \tau_{i+2}^2 & \tau_{i+2}^3 \end{vmatrix} \\ &= (2\tau_i\tau_{i+1}\tau_{i+2}\Delta\tau^3)\Phi_{i-1} - (b\tau_{i-1}\tau_{i+1}\tau_{i+2}\Delta\tau^3)\Phi_i + \\ &\quad (b\tau_{i-1}\tau_i\tau_{i+2}\Delta\tau^3)\Phi_{i+1} - (2\tau_{i-1}\tau_i\tau_{i+1}\Delta\tau^3)\Phi_{i+2} \end{aligned} \quad (3.65)$$

$$\begin{aligned} a_0 &= \frac{\Delta_0}{\Delta} \\ &= \frac{\tau_i\tau_{i+1}\tau_{i+2}}{6(\Delta\tau)^3}\Phi_{i-1} - \frac{\tau_{i-1}\tau_{i+1}\tau_{i+2}}{2(\Delta\tau)^3}\Phi_i + \\ &\quad \frac{\tau_{i-1}\tau_i\tau_{i+2}}{2(\Delta\tau)^3}\Phi_{i+1} - \frac{\tau_{i-1}\tau_i\tau_{i+1}}{6(\Delta\tau)^3}\Phi_{i+2} \end{aligned} \quad (3.66)$$

$$\begin{aligned} \Delta_1 &= \begin{vmatrix} 1 & \Phi_{i-1} & \tau_{i-1}^2 & \tau_{i-1}^3 \\ 1 & \Phi_i & \tau_i^2 & \tau_i^3 \\ 1 & \Phi_{i+1} & \tau_{i+1}^2 & \tau_{i+1}^3 \\ 1 & \Phi_{i+2} & \tau_{i+2}^2 & \tau_{i+2}^3 \end{vmatrix} \\ &= -2(\Delta\tau)^3 \left[3\tau_i^2 + 6\tau_i\Delta\tau + 2(\Delta\tau)^2 \right] \Phi_{i-1} + \\ &\quad 6(\Delta\tau)^3 \left[3\tau_i^2 + 4\tau_i\Delta\tau - (\Delta\tau)^2 \right] \Phi_i - \\ &\quad 6(\Delta\tau)^3 \left[3\tau_i^2 + 2\tau_i\Delta\tau - 2(\Delta\tau)^2 \right] \Phi_{i+1} + \\ &\quad 2(\Delta\tau)^3 \left[3\tau_i^2 - (\Delta\tau)^2 \right] \Phi_{i+2} \end{aligned} \quad (3.67)$$

$$\begin{aligned} a_1 &= \frac{\Delta_1}{\Delta} \\ &= -\frac{3\tau_i^2 + 6\tau_i(\Delta\tau) + 2(\Delta\tau)^2}{6(\Delta\tau)^3}\Phi_{i-1} + \frac{3\tau_i^2 + 4\tau_i(\Delta\tau) - (\Delta\tau)^2}{2(\Delta\tau)^3}\Phi_i - \\ &\quad \frac{3\tau_i^2 + 2\tau_i(\Delta\tau) - 2(\Delta\tau)^2}{2(\Delta\tau)^3}\Phi_{i+1} + \frac{3\tau_i^2 - (\Delta\tau)^2}{6(\Delta\tau)^3}\Phi_{i+2} \end{aligned} \quad (3.68)$$

$$\begin{aligned}
\Delta_2 &= \begin{vmatrix} 1 & \tau_{i-1} & \tau_{i-1}^2 & \Phi_{i-1} \\ 1 & \tau_i & \tau_i^2 & \Phi_i \\ 1 & \tau_{i+1} & \tau_{i+1}^2 & \Phi_{i+1} \\ 1 & \tau_{i+2} & \tau_{i+2}^2 & \Phi_{i+2} \end{vmatrix} \\
&= 6(\Delta\tau)^3 (\tau_i + \Delta\tau) \Phi_{i-1} - 6(\Delta\tau)^3 (3\tau_i + 2\Delta\tau) \Phi_i + \\
&\quad 6(\Delta\tau)^3 (3\tau_i + \Delta\tau) \Phi_{i+1} - 6(\Delta\tau)^3 \tau_i \Phi_{i+2}
\end{aligned} \tag{3.69}$$

$$\begin{aligned}
a_2 &= \frac{\Delta_2}{\Delta} \\
&= \frac{\tau_i + \Delta\tau}{2(\Delta\tau)^3} \Phi_{i-1} - \frac{3\tau_i + 2\Delta\tau}{2(\Delta\tau)^3} \Phi_i + \\
&\quad \frac{3\tau_i + \Delta\tau}{2(\Delta\tau)^3} \Phi_{i+1} - \frac{\tau_i}{2(\Delta\tau)^3} \Phi_{i+2}
\end{aligned} \tag{3.70}$$

$$\begin{aligned}
\Delta_3 &= \begin{vmatrix} 1 & \tau_{i-1} & \tau_{i-1}^2 & \Phi_{i-1} \\ 1 & \tau_i & \tau_i^2 & \Phi_i \\ 1 & \tau_{i+1} & \tau_{i+1}^2 & \Phi_{i+1} \\ 1 & \tau_{i+2} & \tau_{i+2}^2 & \Phi_{i+2} \end{vmatrix} \\
&= -2(\Delta\tau)^3 \Phi_{i-1} + 6(\Delta\tau)^3 \Phi_i - \\
&\quad 6(\Delta\tau)^3 \Phi_{i+1} + 2(\Delta\tau)^3 \Phi_{i+2}
\end{aligned} \tag{3.71}$$

$$\begin{aligned}
a_3 &= \frac{\Delta_3}{\Delta} \\
&= -\frac{\Phi_{i-1}}{6(\Delta\tau)^3} + \frac{\Phi_i}{2(\Delta\tau)^3} - \frac{\Phi_{i+1}}{2(\Delta\tau)^3} + \frac{\Phi_{i+2}}{6(\Delta\tau)^3}
\end{aligned} \tag{3.72}$$

The 4th order temporal derivation is calculated through the polynomial development as follows:

$$\left(\frac{\partial \Phi}{\partial \tau} \right)_{\tau=\tau_n} = a_1 + 2a_2\tau_n + 3a_3\tau_n^2 \tag{3.73}$$

where a_1 , a_2 and a_3 are calculated by equations 3.68, 3.70 and 3.72 respectively.

(4) Flow Chart of Computer Program

The main structure of the 3D acoustic solver is shown in figure 3.4 (page 47). In figure 3.4(a), the main structure is divided into the pre-process, main process and post process; and in figure 3.4(b), the main loops of the main process are presented.

3.2.3 2D Integral Extension

The numerical approaches for the 2D integral extension will be represented with the example of the formulation of LOCARD. The numerical treatment for the formulation of GUO is similar; only the GREEN's function used is different.

The first step is the storage of the aerodynamic quantities of aeroacoustic source informations, namely, the time history of variables (ρ, u_1, u_2, p) are recorded on the control surface. If the storage of the aerodynamic quantities are on a 3D cylindrical control surface, an averaging in the span direction should be carried to obtain the 2D input for the 2D aeroacoustic solver.

Secondly, the source terms, F_i and Q , in equations 2.109 and 2.110 are calculated and transformed into the frequency domain by a forward FFT defined as:

$$\begin{aligned}\tilde{\Phi}(J, k) &= \Delta\tau \sum_{m=0}^{N_t-1} \Phi(J, m) e^{-i2\pi km/N_t} \quad , \quad J = 1, 2, \dots, N_y \\ \tau &= m\Delta\tau \quad , \quad m = 0, 1, \dots, N_t - 1 \\ \omega &= \frac{2\pi k}{N_t\Delta\tau} \quad , \quad k = 0, 1, \dots, N_t - 1\end{aligned}\tag{3.74}$$

where N_y is the number of source panels, N_t is the number of the time steps, and $\Delta\tau$ is the time step.

Then the surface integrations are evaluated for each observation point in the frequency domain with the midpoint quadrature:

$$\begin{aligned}p'(I, \omega) &= \sum_{J=1}^{N_y} \left\{ \tilde{L}_1(J, \omega) \frac{\partial G}{\partial y_1}(I, J; \omega) + \tilde{L}_2(J, \omega) \frac{\partial G}{\partial y_2}(I, J; \omega) \right. \\ &\quad \left. - i\omega \tilde{Q}(J, \omega) G(I, J; \omega) \right\} \Delta l(J) \quad , \\ I &= 1, 2, \dots, N_x\end{aligned}\tag{3.75}$$

$$G(I, J; \omega) = A(r_1(I, J), \omega) H_0^{(2)}(I, J; \omega)\tag{3.76}$$

$$\begin{aligned}\frac{\partial G}{\partial y_1}(I, J; \omega) &= -A(r_1(I, J), \omega) \left\{ \frac{iM\omega}{\beta^2 c_0} H_0^{(2)}(I, J; \omega) \right. \\ &\quad \left. - \frac{\omega}{\beta^2 c_0} \frac{r_1(I, J)}{r_\beta(I, J)} H_1^{(2)}(I, J; \omega) \right\}\end{aligned}\tag{3.77}$$

$$\frac{\partial G}{\partial y_2}(I, J; \omega) = A(r_1(I, J), \omega) \left\{ \frac{\omega}{c_0} \frac{r_2(I, J)}{r_\beta(I, J)} H_1^{(2)}(I, J; \omega) \right\}\tag{3.78}$$

where:

$$r_\alpha(I, J) = x_\alpha(I) - y_\alpha(J) \quad , \quad \alpha = 1, 2\tag{3.79}$$

$$r_\beta(I, J) = \sqrt{(x_1(I) - y_1(J))^2 + \beta^2(x_2(I) - y_2(J))^2} \quad (3.80)$$

$$\beta^2 = 1 - M^2 \quad (3.81)$$

$$A(r_1(I, J), \omega) = \frac{i}{4\beta} \exp\left(\frac{iM\omega r_1(I, J)}{\beta^2 c_0}\right) \quad (3.82)$$

And $H_k^{(n)}$ is a HANKEL function of the n th kind and the k th order.

Lastly, an inverse FFT is used to recover the acoustic signal into the time domain if required:

$$\begin{aligned} \Phi(I, m) &= \Delta\tau \sum_{k=0}^{N_t-1} \tilde{\Phi}(I, k) e^{i2\pi mk/N_t}, \quad I = 1, 2, \dots, N_x \\ \tau &= m\Delta\tau, \quad m = 0, 1, \dots, N_t - 1 \\ \omega &= \frac{2\pi k}{N_t\Delta\tau}, \quad k = 0, 1, \dots, N_t - 1 \end{aligned} \quad (3.83)$$

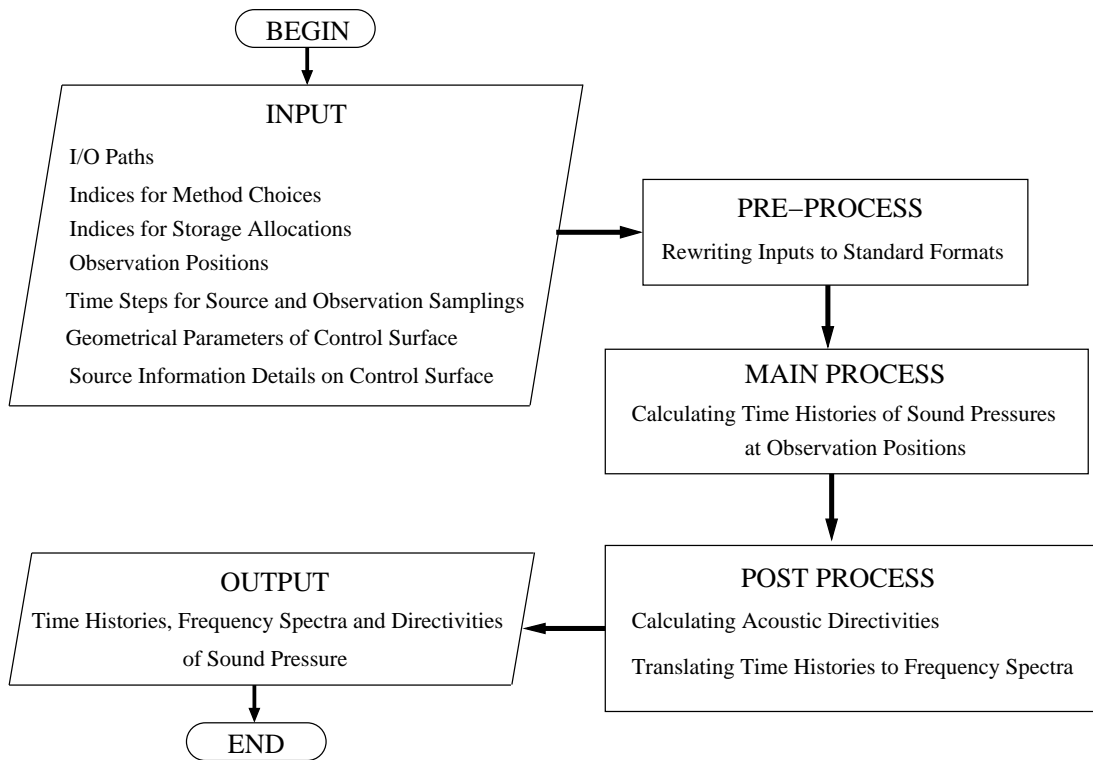
where N_x is the number of observation points, N_t is the number of the time steps, and $\Delta\tau$ is the time step.

The source terms are calculated through the CFD and usually cannot be perfectly periodic in time. Thus error is introduced into the presentation of the sources at a particular frequency. For turbulent flow, the sound pressure consists of two parts: the deterministic impulse noise and non-deterministic (stochastic, broadband) noise. To calculate the non-deterministic noise part, windowing techniques and averaging transforms of individual (overlapping) segments of the sampled data can be used to increase the accuracy of the transform. In the current work, a HANNING window is used by the Fourier transform of equation 3.74 to obtain the turbulent noise spectrum:

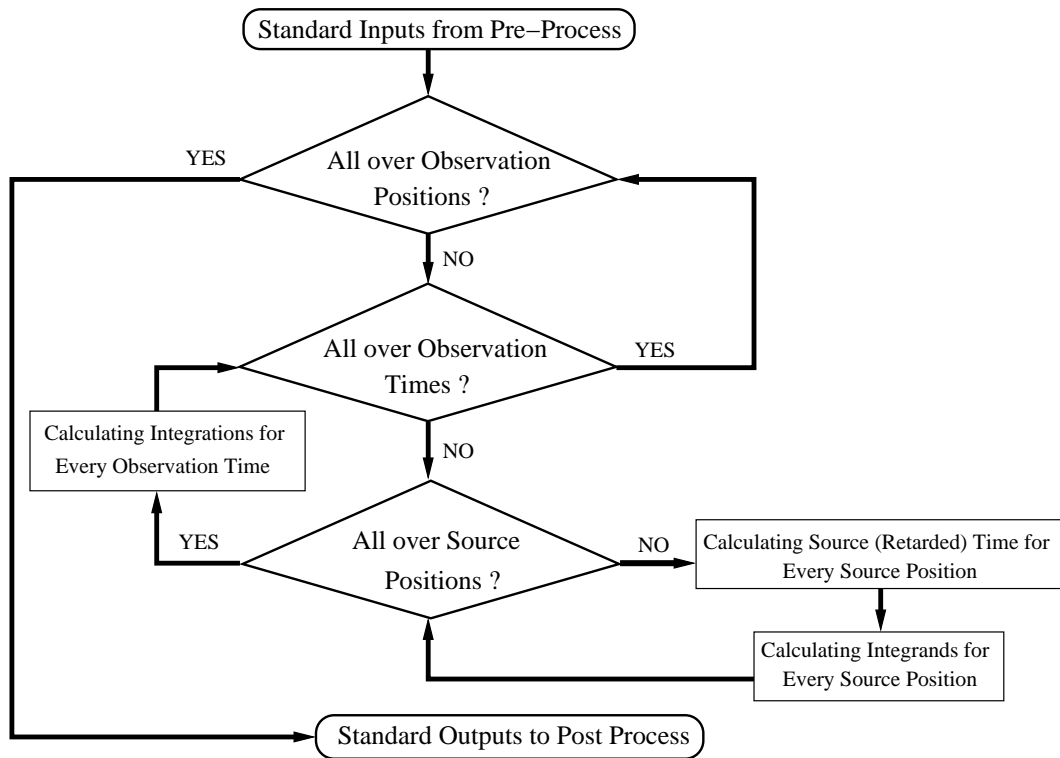
$$\tilde{\Phi}(J, k) \Leftarrow 0.5\tilde{\Phi}(J, k) - 0.25\tilde{\Phi}(J, k - 1) - 0.25\tilde{\Phi}(J, k + 1) \quad (3.84)$$

where J is the index of the source position and k is the index of the frequency. By the acoustic analogy approach, the acoustic far field prediction may be very sensitive to small changes in the description of the source. Therefore, the improvement of accuracy of the treatment of acoustic sources is necessary.

The main structure of the 2D acoustic solver is shown in figure 3.5 (page 48). In figure 3.5(a), the main structure is divided into the pre-process, main process and post process; and in figure 3.5(b), the main loops of the main process are presented.

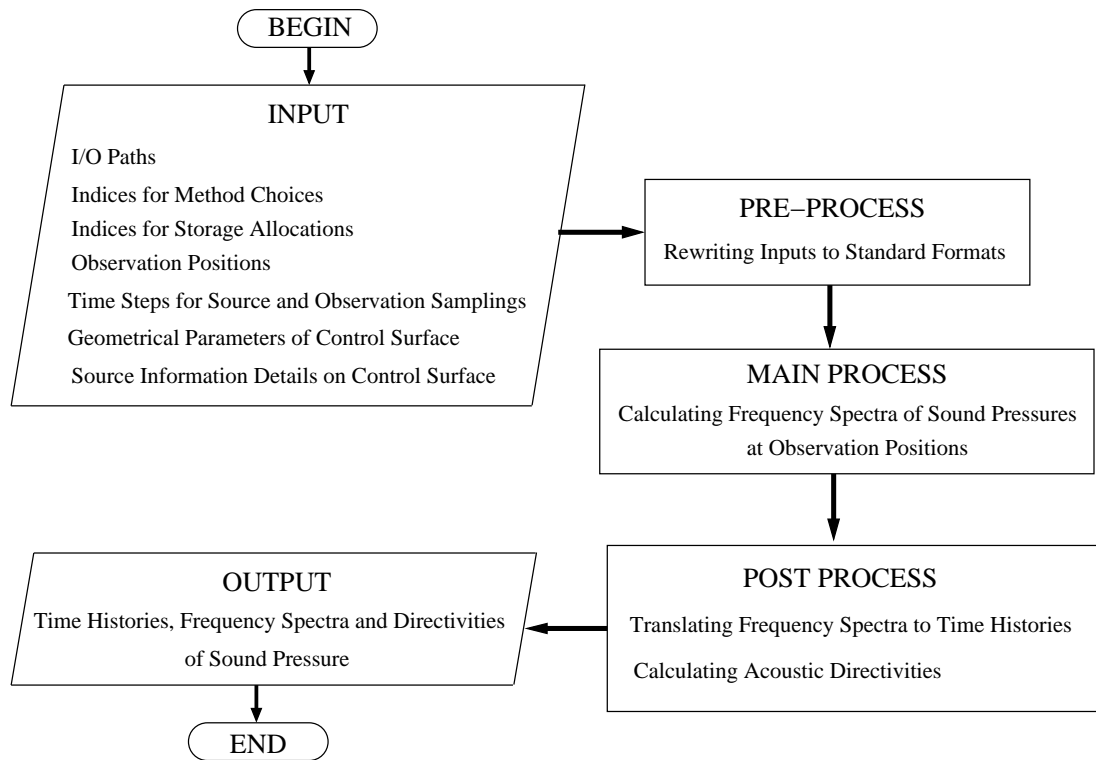


(a) The Main Structure

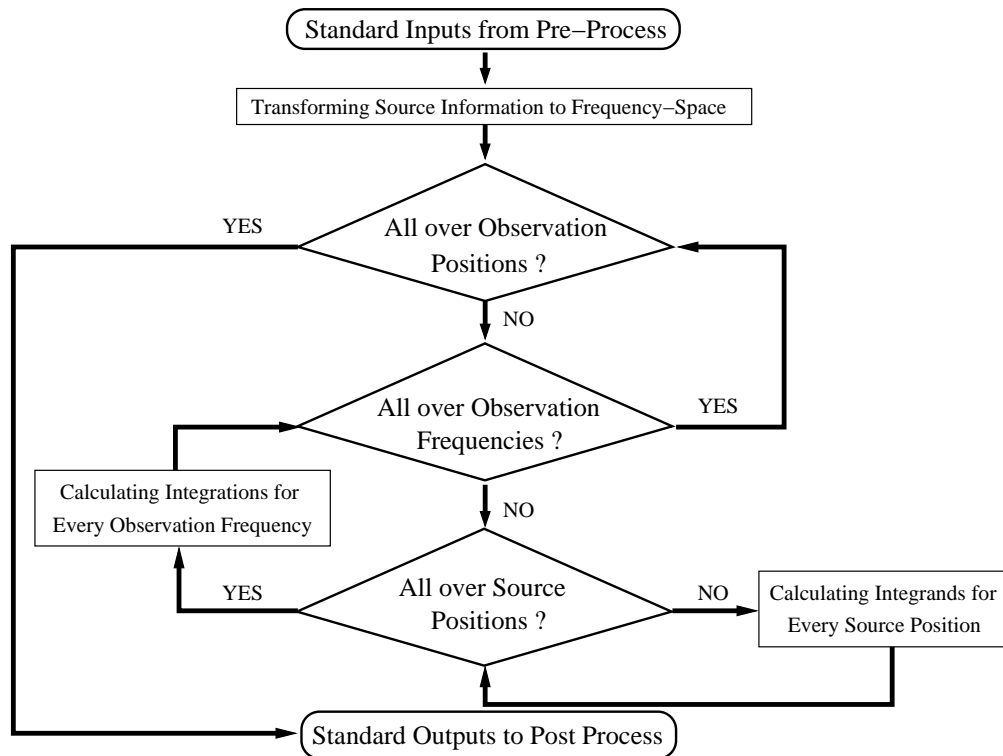


(b) The Main Loops of the Main Process

Figure 3.4: The Main Structure of the 3D Acoustic Solver



(a) The Main Structure



(b) The Main Loops of the Main Process

Figure 3.5: The Main Structure of the 2D Acoustic Solver

Chapter 4

Verification and Validation

When a new computer program is implemented to solve the governing equation system for a physical problem of interest, it should be verified and validated before it can be applied to obtain solutions in general cases. Following the widely accepted definitions of ROACHE [67], **verification** means to confirm if the code *solves the governing equations right*, and **validation** means to check whether the code *solves the right equations*.

A **verification** is a confirmation of the numerical errors by solving the governing equations numerically. The **verification** can be ideally carried out with the aid of analytical solutions of the governing equations, because the numerical errors are easy to be calculated through the comparison between the numerical and analytical solutions. In the present context, several special analytical solutions of aerodynamically generated sound fields are chosen to verify the code, which are based on the 3D retarded-time integral formulation of FARASSAT and 2D Fourier-transformed integral formulation of GUO and LOCARD for the solution of the FW-H equation. The verification results are presented in the first section of this chapter.

In the second section of this chapter, the **validation** results are presented. A **validation** is a confirmation of the modeling errors by establishing the related governing equations for the physical problem of interest. The physical problem of interest to the author is aeroacoustic sound generation by a flow past a bluff body. The code used is based upon a CFD/(porous)FW-H approach. The modeling errors of this approach can be identified through comparison with a comprehensive database of the dynamic near-field and acoustic far-field measured when a flow passes a bluff body. In the present work a numerical database from the aeroacoustic DNS of a flow around a circular cylinder at $Re_D = 150$ by INOUE [38] is adopted as a benchmark for the validation, under the premise that this DNS is accurate enough to simulate the physical phenomena. In practice, the experimental database available for aeroacoustic validation is very limited, because of the difficulties of carrying out such kinds of experiments. It is an acceptable way that the simplified analogical approach, such as the (porous) FW-H integral extension, be validated through a DNS database.

4.1 Verifications with Analytical Solutions

In the present verification, the analytical solutions of a point 3D monopolar, dipolar or quadrupolar source, as well as a linear two-dimensional monopolar and dipolar source, are chosen to confirm the numerical errors due to the numerical approximations described in chapter 3. The asymptotic solutions of three co-rotating line vortices are used to verify the ability of the program to simulate sound generation by an unsteady flow with a control surface in the dynamically non-linear flow region. An acoustic monopole in a uniform flow is used to confirm the ability of the code based on the formulation of LOCARD to simulate the acoustic propagation in a uniformly moving medium.

4.1.1 3D Mono-, Di- and Quadrupole

A source which produces a 3D omnidirectional volume flux in the near-field and 3D omnidirectional sound pressure wave in the far-field, such as a pulsating sphere, is called a 3D monopolar source. If this 3D monopolar source is compact, it can be regarded as a monopolar point source, or a monopole. A compact oscillating sphere, which is equivalent to two very closely positioned monopole point sources with opposite fluctuation phases, is denoted as a dipolar point source or 3D dipole. A dipole has a axis which is the line connecting the centers of two nearby monopoles. A compact combination of two very closely positioned dipolar point sources forms a quadrupolar point source or 3D quadrupole. There are two kinds of quadrupoles – lateral and longitudinal quadrupoles. For a longitudinal quadrupole, the separation between the dipoles is in the direction of their axes. For a lateral quadrupole, the separation is perpendicular to the dipole axis. A lateral quadrupolar source is used as the verification example. According to the aeroacoustical analogy, the mono-, di- and quadrupoles are caused respectively by the fluctuations of matter flux, force and stress in the unsteady flow field. The mono-, di-, and quadrupoles can be regarded as basic components for a complicated aerodynamical source. If the particle displacement of the fluid near the source is much smaller than the wavelength of the fluctuation propagation, the source is called a linear source. In the present verification, only the linear 3D mono-, di- and quadrupolar sources are used.

The corresponding analytical solutions are presented in appendix A.2. These analytical solutions are the special solutions of the governing equations presented in appendix A.1. The tested parameters of these sources are :

$$\begin{aligned} r_a &= 0.01 \text{ (m)} ; d = 0.025 \text{ (m)} ; U_n = 6.8 \text{ (m/s)} ; \\ \omega &= 3\pi , 6\pi , 12\pi , \dots , 3k\pi , 6k\pi \text{ (rad/s)} . \end{aligned}$$

The $U_n/c_0 = 0.0198$ (c_0 is the undisturbed sound speed) ensures the source is a linear

source, and simultaneously the fact that U_n is a similar size to the temporal velocity fluctuation investigated in the following cases of a flow past a circular cylinder at $Re_D = 150$ and 3900 .

The 3D mono-, di-, and quadrupolar sources with the above parameters are used to verify the code based on the 3D retarded-time formulation of FARASSAT. The most important criterion for the verification is the numerical error. The following relative average error, ε_{av} , is used as a measure:

$$\varepsilon_{av} = \frac{\sum_{i=1}^{N_s} \sum_{j=1}^{N_t} |p_{num}(\vec{x}_i, t_j) - p_{ana}(\vec{x}_i, t_j)|}{\sum_{i=1}^{N_s} \sum_{j=1}^{N_t} |p_{ana}(\vec{x}_i, t_j)|} \quad (4.1)$$

where $p_{num}(\vec{x}_i, t_j)$ and $p_{ana}(\vec{x}_i, t_j)$ denote respectively the numerical solution of sound pressure at the observation point, \vec{x}_i , and at the observation time, t_j . N_s and N_t are respectively the total number of the observation points and times. This ε_{av} is a relative error averaging over all the observation positions ($\vec{x}_i \in (\vec{x}_1, \vec{x}_2, \dots, \vec{x}_{N_s})$) and all the observation times ($t_j \in (t_1, t_2, \dots, t_{N_t})$).

The FW-H integral formulations satisfy automatically the non-reflecting outgoing far-field boundary condition. The numerical errors of such kinds of integral extension from the near-field CFD data to the acoustic far-field are mainly the so-called spatial and temporal discretization errors, which should be convergent to zero if the spatial and temporal resolutions are up to ∞ . These two kinds of errors are confirmed separately in the present verification through the following procedures.

At first, all the integrands, which are dependent on the spatial position and retarded time, are calculated analytically without any numerical approximations at every panel position and retarded time required for the numerical quadrature, even the temporal derivations in the integrands are also calculated analytically. This means the input information on the control surface is still continuous in time, and the surface integrations are calculated only with the spatial approximation of a numerical quadrature over the discrete panels. The error calculated through the comparison between the numerical and analytical solutions is a pure numerical quadrature error due to the spatial approximation, which is denoted as the spatial discretization error, $\varepsilon_{av,s}$.

After the spatial discretization error is confirmed, the total error, ε_{av} , due to both the spatial and temporal discretizations can be calculated if the near-field input is a flow information at a series of discrete times. The discrete times of input are not the same as the require retarded times. The integrands have to be calculated with numerical interpolations at the retarded times and with numerical temporal derivations. Then the temporal discretization error, $\varepsilon_{av,t}$, can be calculated by the subtraction of $\varepsilon_{av,s}$ from ε_{av} .

By the confirmation of the spatial discretization error, the control surface is discretized through a computational grid, which is well-distributed on a sphere. Four computational grids with different spatial resolutions are used. The total panel numbers of these grids are: 150, 486, 1734 and 6534. The panels are well-distributed on the spherical control surface, namely, most panels have similar areas. The computational grids are generated with the mesh-generator ICEMCFD. Through different scalings, the computational grid can have the required radius, r_c , as one of the following:

$$r_c = 0.5 , 0.6 , 1.2 , 2.4 , 4.8 \text{ (m)}$$

For the quantification of the resolution of the grid, there are three characteristic dimensionless quantities, namely the largest panel angle, $\Delta\theta_{max}$, which is proportional to the discontinuity scale of the panel direction between nearby panels; the largest dimensionless panel diagonal length, $\Delta l_{max}/\lambda$, which is nominated with the characteristic wavelength of the source, λ ; and the dimensionless radius of the control surface, r_c/λ , which is also nominated with the characteristic wavelength, λ . The definition of the panel angle, $\Delta\theta$, panel diagonal length, Δl , and control surface radius, r_c , are shown in figure 4.1. Only two of these three dimensionless values are independent.

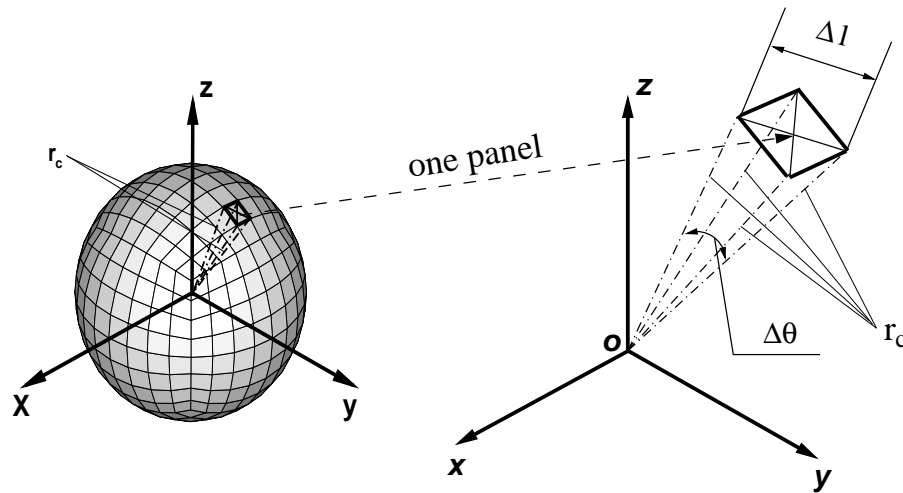


Figure 4.1: The Characteristic Values of Spatial Discretion

The $\Delta\theta_{max}$ for the four computational grids are:

$$\begin{aligned} \Delta\theta_{max} &= 0.05 , 0.10 , 0.20 , 0.39 \text{ (radian)} ; \text{ or} \\ &= 2.88 , 5.76 , 11.45 , 22.33 \text{ (degree)} . \end{aligned}$$

With these four grids for different source frequencies, ω , and different control surface radii, r_c , shown in the above context, a wide range of values of $\Delta l_{max}/\lambda$ and r_c/λ are tested:

$$\Delta l_{max}/\lambda = 0.00105 , 0.0021 , 0.0042 , 0.0084 , 0.0168 , 0.0337 ,$$

$$r_c/\lambda = \begin{matrix} 0.0675, 0.135, 0.27, 0.54, 1.06; \\ 0.0053, 0.0105, 0.021, 0.042, 0.084, 0.168, \\ 0.337, 0.675, 1.35, 2.7, 5.4. \end{matrix}$$

The observation positions chosen for the present verification are at 72 homogeneously distributed points on a circle with a radius, r_0 , from the center of the source in the plane of the di- and quadrupolar sources:

$$r_0 = 50.0 \text{ (m)} .$$

The verification results of the spatial discretization errors by the numerical simulation of a 3D monopole are shown in figures 4.2 to 4.5 (see pages 54 to 55). As described in chapter 3, the quadratures are calculated with two methods – the 2nd order midpoint and 4th order SIMPSON's schemes. Figures 4.2(a), 4.3(a), 4.4(a) and 4.5(a) show the simulation results of a 3D monopolar source based on the 2nd order midpoint quadrature, and figures 4.2(b), 4.3(b), 4.4(b) and 4.5(b) show those based on the 4th order SIMPSON's quadrature.

Figures 4.2(a) and 4.2(b) (page 54) present the directivity patterns of root mean square sound pressure at the observation positions based on two kinds of quadratures. In these two figures, one can see that both 2nd and 4th order quadrature give a very good agreement with the analytical solution if the spatial resolution is fine enough, e.g. $\Delta\theta_{max} = 2.88^\circ$ and $\Delta l_{max}/\lambda = 0.0675$, but the result of 4th order quadrature is better than that of 2nd order if the spatial resolution is coarse, e.g. $\Delta\theta_{max} = 22.33^\circ$ and $\Delta l_{max} = 0.54$. More details about the spatial discretization error are presented in figure 4.3 to figure 4.5.

In figures 4.3(a) and 4.3(b) (page 54) the relative error, $\varepsilon_{av,s}$, is depicted against $\Delta l_{max}/\lambda$ and grouped with $\Delta\theta_{max}$. In figure 4.3(a) for the 2nd order quadrature, the $\varepsilon_{av,s}$ reduces continuously until a minimum, depending on the $\Delta\theta_{max}$, if the $\Delta l_{max}/\lambda$ goes down from the largest $\Delta l_{max}/\lambda \approx 1.0$ to the smallest $\Delta l_{max}/\lambda \approx 0.0003$ and $\Delta\theta_{max}$ is fixed at one value. This minimum of $\varepsilon_{av,s}$ is proportional to the value of $\Delta\theta_{max}$. After the $\varepsilon_{av,s}$ reaches this minimum, it changes little, even if $\Delta l_{max}/\lambda$ goes down further. The value of $\Delta l_{max}/\lambda$ to reach the error minimum is in inverse proportion to $\Delta\theta_{max}$. In figure 4.3(b) for the 4th order quadrature, the similar features of $\varepsilon_{av,s}$ are shown, with the small difference that the error minimum for the 4th order scheme is somewhat lower and the $\Delta l_{max}/\lambda$ to reach this minimum is also smaller. From these two figures, 4.3(a) and 4.3(b), the following conclusions can be inferred:

For every $\Delta\theta_{max}$ there is a limit value of $\Delta l_{max}/\lambda$, which decides the limit of the accuracy improvement by decreasing $\Delta l_{max}/\lambda$. Reducing $\Delta l_{max}/\lambda$ to a value smaller than this value brings no benefit for the accuracy, because the absolute dominant error is, in the case, the error due to the resolution of the panel angle, $\Delta\theta$. The limit

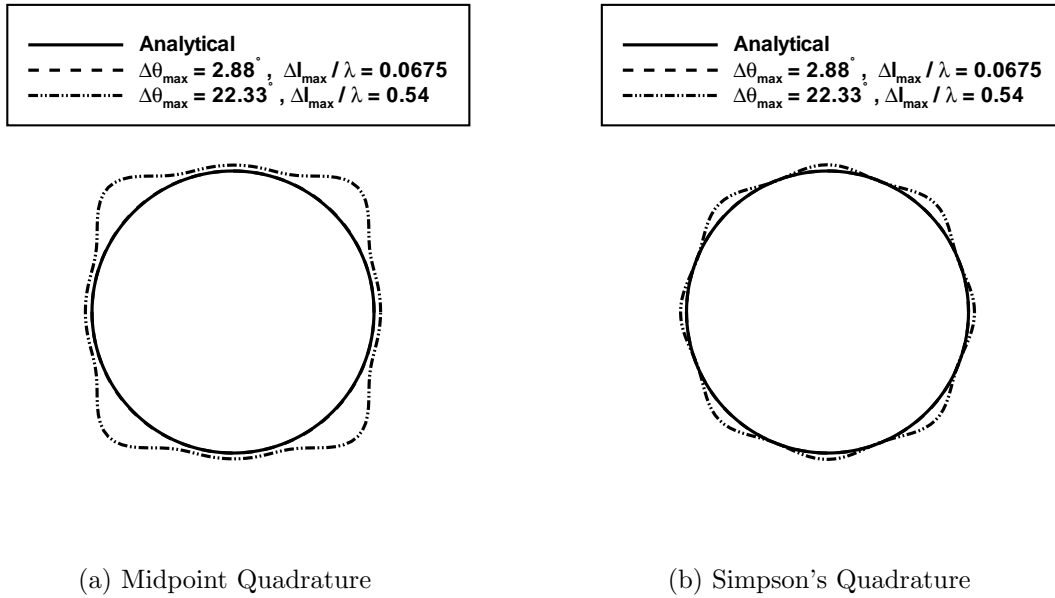


Figure 4.2: Simulated Directivity of Sound Pressure (3D-Monopole)

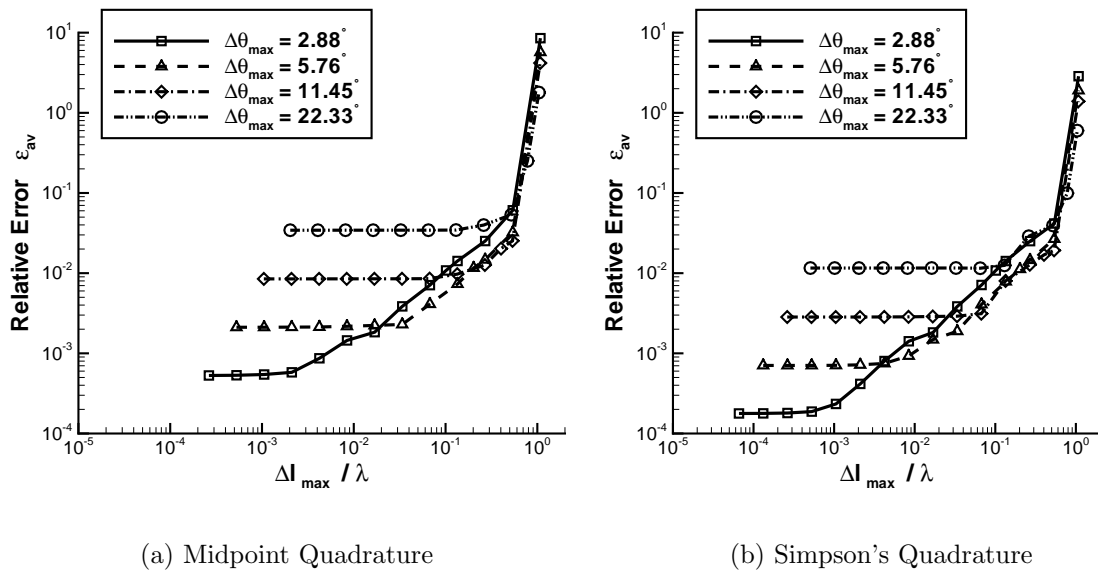


Figure 4.3: Spatial Discretization Error vs $\Delta l_{\max}/\lambda$ (3D-Monopole)

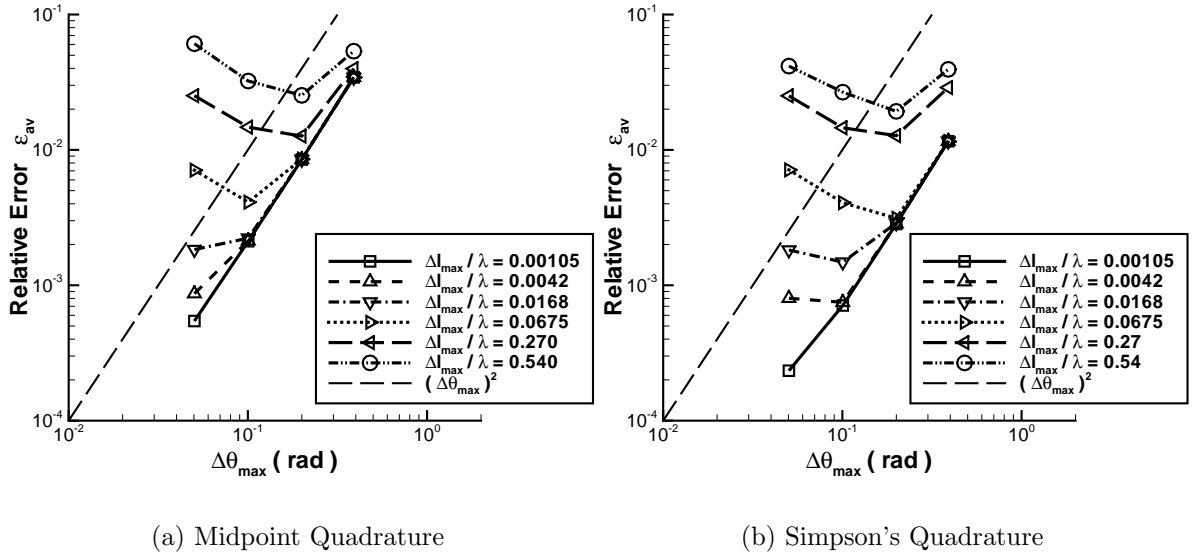


Figure 4.4: Spatial Discretization Error vs $\Delta\theta_{max}$ (3D-Monopole)

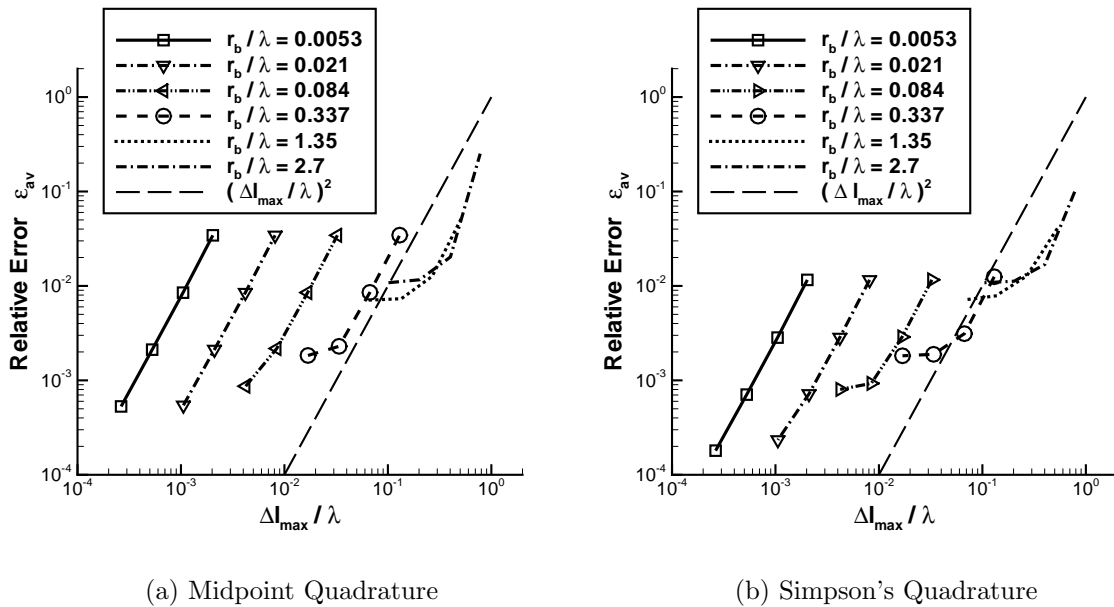


Figure 4.5: Spatial Discretization Error of Same r_b/λ (3D-Monopole)

values of $\Delta l_{max}/\lambda$ against the tested $\Delta\theta_{max}$ for the 2nd and 4th order quadratures are shown in table 4.1.

$\Delta\theta_{max}$	2.88°	5.76°	11.45°	22.33°
$\Delta l_{max}/\lambda$ (2nd order)	0.0021	0.0337	0.0675	0.135
$\Delta l_{max}/\lambda$ (4th order)	0.000675	0.0042	0.0375	0.135

Table 4.1: Critical Spatial Resolution Parameters

For every $\Delta l_{max}/\lambda$ there is an optimal $\Delta\theta_{max}$. A lower value than this optimal value brings no benefit.

In figures 4.4(a) and 4.4(b) (page 55), the relative error, $\varepsilon_{av,s}$, is plotted against $\Delta\theta_{max}$ and grouped with $\Delta l_{max}/\lambda$. In figure 4.4(a) for the 2nd order quadrature, if $\Delta\theta_{max}$ is in the range of 22.33° (0.39 rad) down to 11.45° (0.20 rad), the values of $\varepsilon_{av,s}$ for $\Delta l_{max}/\lambda$ in the range of 0.00105 up to 0.27 are almost the same and reduce with 2nd order of rate against $\Delta\theta_{max}$. But if $\Delta\theta_{max}$ is in the range of 11.45° (0.20 rad) down to 5.76° (0.10 rad), only the values of $\varepsilon_{av,s}$ for the smaller $\Delta l_{max}/\lambda$ in the range of 0.00105 up to 0.0337 are almost the same and reduce with 2nd order of rate against $\Delta\theta_{max}$. The values of $\varepsilon_{av,s}$ for the relatively large $\Delta l_{max}/\lambda$ in the range of 0.0675 up to 0.54 are different and proportional to $\Delta l_{max}/\lambda$. And if $\Delta\theta_{max}$ goes down from 5.76° (0.10 rad) to 2.88° (0.05 rad), only for $\Delta l_{max}/\lambda$ smaller than 0.0042, the error reduces still with 2nd order of rate. For the relatively large $\Delta l_{max}/\lambda$, the error even increases when $\Delta\theta_{max}$ decreases from a small value to a smaller one. For example, for $\Delta l_{max}/\lambda = 0.0337$, the error increases when $\Delta\theta_{max}$ decreases from 5.76° (0.10 rad) to 2.88° (0.05 rad). In figure 4.4(b) for the 4th order quadrature, similar features can be seen. The small distinction here is that the value of the error is smaller in case of $\Delta\theta_{max}$ smaller than 5.76° (0.10 rad) and $\Delta l_{max}/\lambda$ smaller than 0.0337. In the coarse resolution cases of $\Delta\theta_{max}$ larger than 11.45° (0.20 rad) and $\Delta l_{max}/\lambda$ larger than 0.35, the error even increases when $\Delta\theta_{max}$ decreases from a small value to a smaller one.

In figures 4.5(a) and 4.5(b) (page 55), the relative error, $\varepsilon_{av,s}$, is plotted against $\Delta l_{max}/\lambda$ and grouped with r_b/λ . The above dependencies of the spatial discretization error are shown again. Because the surface integrations shown in equations 2.77 and 2.78 are the vector integration, depending upon the direction of the local surface direction and the direction from every source position to the observation position. The scalar 4th order SIMPSON's scheme brings no 4th order of the accuracy against the linear spatial resolution, $\Delta l_{max}/\lambda$, without a change of the angle resolution, $\Delta\theta_{max}$.

The features of the numerical error versus spatial resolutions in the case of 3D point dipole and quadrupole simulation are similar to that of the monopole. The features in the case of a dipole are shown in figures 4.6(a) and 4.6(b) (page 57). The features in the

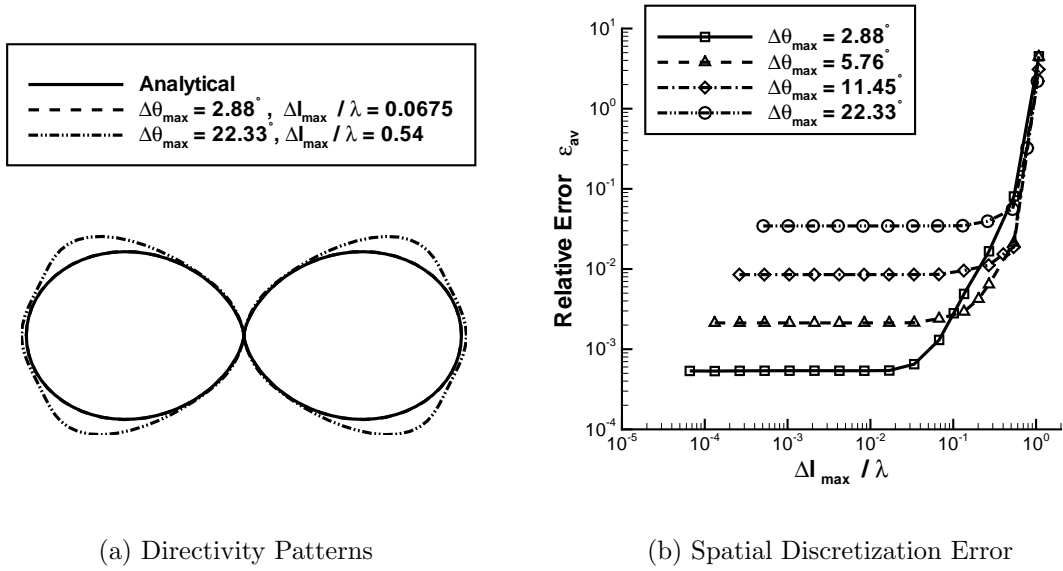


Figure 4.6: Simulation of 3D-Dipole (Midpoint Quadrature)

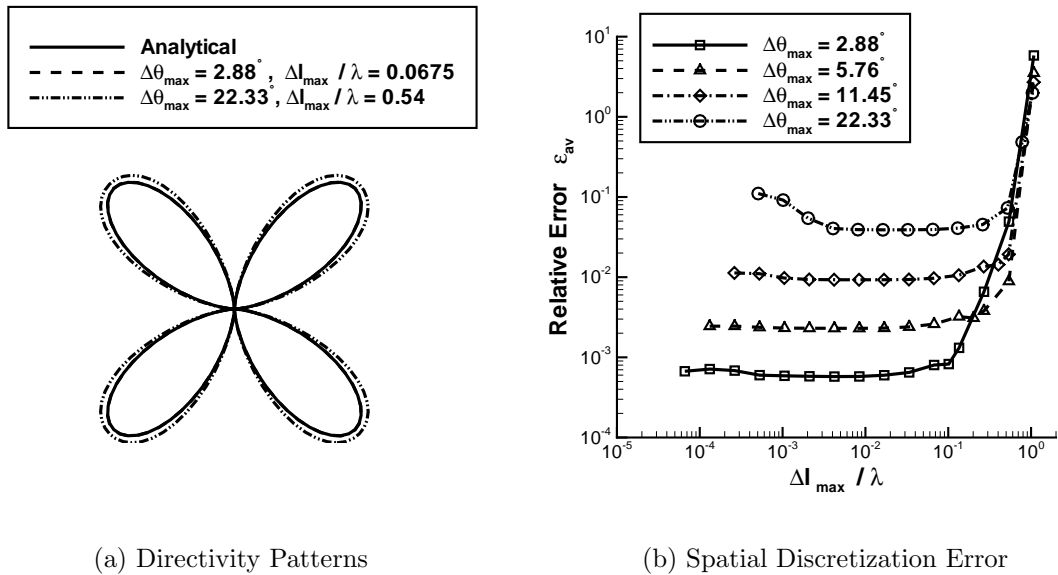


Figure 4.7: Simulation of 3D-Quadrupole (Midpoint Quadrature)

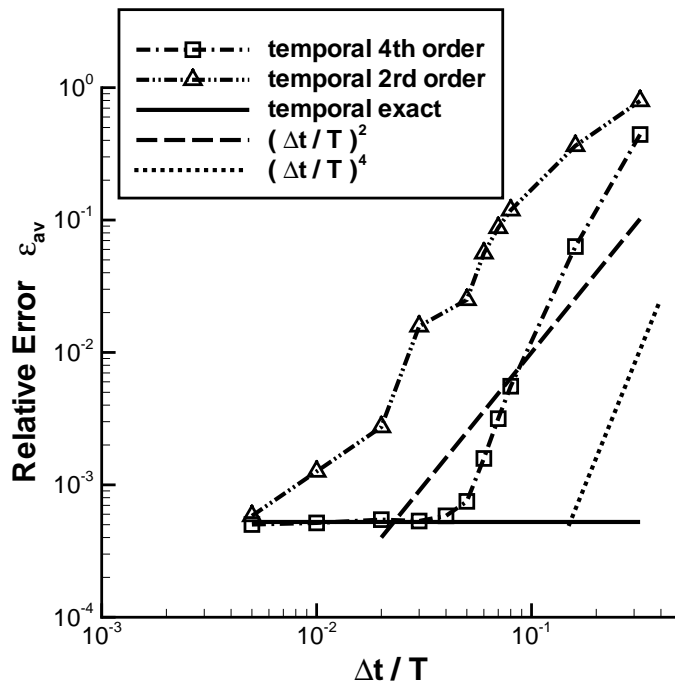


Figure 4.8: Temporal Discretization Errors of 3D-Monopole Simulation

case of a quadrupole are shown in figures 4.7(a) and 4.7(b) (page 57). The critical spatial resolution parameters, shown in table 4.1 (page 56), are also approximately valid for the cases of a dipole and a quadrupole.

The numerical error versus temporal resolution is shown in figure 4.8. The convergent rates of the numerical results based on the 2nd and 4th order schemes are also 2nd and 4th order respectively. If the temporal resolution is fine enough, namely $\Delta t/T$ is smaller than 0.02 for the 2nd order scheme or $\Delta t/T$ is smaller than 0.07 for the 4th order scheme, the numerical error due to the temporal resolution, $\epsilon_{av,t}$, is smaller than 0.5%. The part of the computer program related to the temporal discretization is therefore verified.

From the above details about the numerical error, the following conclusions about the total numerical error, ϵ_{av} ($\epsilon_{av} = \epsilon_{av,s} + \epsilon_{av,t}$), can be obtained:

The capacity of the code is confirmed by the verification examples. The relative error can be under 0.5% under the optimal parameters.

Because the 4th order Simpson's quadrature is only about 2nd order accuracy for the end effect with respect to a vector integration required in the current work, it is suggested to use the 2nd order midpoint quadrature. The midpoint quadrature is sufficient when the spatial resolution is not too coarse, namely $\Delta l_{max}/\lambda < 0.2$ and $\Delta\theta_{max} < 22^\circ$, compared with the SIMPSON's quadrature.

The angular resolution, $\Delta\theta_{max}$, should be paid more attention to, to ensure that it is not more than 6° for a 0.5% numerical error, namely not less than about 60 panels per circle or 1800 panels per sphere.

The simulated acoustic far-field is usually not so sensitive to the linear resolution, $\Delta l_{max}/\lambda$. If $\Delta l_{max}/\lambda$ is less than 0.2, the relative error can already be under 5%; For a $\Delta l_{max}/\lambda$ of less than 0.02, the relative error is under 0.5%.

If $\Delta t/T$ is smaller than 0.02 for the 2nd order temporal approximations, namely one pseudo-period 50 points, or $\Delta t/T$ is smaller than 0.07 for the 4th order temporal approximations, the relative error due to the temporal approximation can be under 0.5%. It is suggested to choose the 4th order numerical temporal interpolation and derivation schemes when $\Delta t/T$ is more than 0.02. If $\Delta t/T$ is less than 0.02, the 2nd order numerical approximation gives a good result.

4.1.2 2D Mono- and Dipole

A compact source which produces a 2D omnidirectional volume flux in the near-field and 2D omnidirectional sound pressure wave in the far-field, such as a compact pulsating circular cylinder, is called a monopolar line source or 2D monopole. A compact oscillating cylinder, which is equivalent to two very closely positioned monopole line sources with opposite fluctuation phases, is denoted as a dipolar line source or 2D dipole. A compact combination of two very closely positioned dipolar line sources forms a quadrupolar line source or 2D quadrupole. There are two kinds of quadrupoles – lateral and longitudinal quadrupoles. For a longitudinal quadrupole, the separation between the dipoles is in the direction of their axes. For a lateral quadrupole the separation is perpendicular to the dipole axis. Mono-, di- and quadrupolar line sources are respectively caused by the 2D fluctuations of matter flux, force and stress in the unsteady flow field. For the (porous) FW-H approach, the far-field sound pressure can be calculated through the integration of a distribution of monopoles and dipoles on the control surface, if the control surface encircles all the effective quadrupoles. Therefore, the 2D mono- and dipole are the basic verification cases for the code based on the 2D Fourier-transformed formulation of GUO. Moreover, if the 3D retarded-time formulation of FARASSAT is used to simulate the 2D mono- and dipole, the copy length, L_c , shown in figure 3.1 of page 38, should be used to obtain the effective control surface length in the third direction vertical to the main plane.

The corresponding analytical solutions are presented in appendix A.3. The tested parameters of these sources are :

$$\begin{aligned} r_a &= 0.001, 0.005, \text{ and } 0.01 \text{ (m)} ; \\ U_n &= 0.68, 6.8, \text{ and } 68.0 \text{ (m/s)} ; \\ \omega &= 3\pi, 6\pi, \dots, \text{ and } 24k\pi \text{ (rad/s)} . \end{aligned}$$

The control surface is a circular cylindrical surface with the radius, r_c . The following r_c 's are tested:

$$r_c = 0.5 , 0.6 , 1.2 , 2.4 , \text{ and } 4.8 \text{ (m)} .$$

Actually the surface integrations for the 2D Fourier-transformed formulation of GUO are reduced to curve integrations. The control surface can be regarded as a control circle with radius r_c for these cases. Only by using the code based on the 3D retarded-time formulation of FARASSAT, the control surface is a circular cylindrical surface with the copy length, L_c .

The generatrix curve of the control surface is a circle and discretized with a simple computational grid. The grid points are homogeneously distributed on the circle. Six computational grids with different resolutions are used. The number of grid points on the circle, N , are:

$$N = 4 , 8 , 16 , 32 , 64 \text{ and } 128 .$$

If the copy length in the third direction is required, the panel height is approximately equal to the panel width in the generatrix plane.

For the quantification of the spatial resolution of the grid, there are three characteristic dimensionless quantities, namely the panel angle, $\Delta\theta$, which is proportional to the discontinuity scale of surface directions of the panels; the dimensionless panel diagonal length, $\Delta l/\lambda$, which is nominated with the characteristic wavelength of the sound source, λ ; and the dimensionless radius of the control surface, r_c/λ , which is also nominated with the characteristic wavelength, λ . The definition of the panel angle, $\Delta\theta$, panel diagonal length, Δl , and control surface radius, r_c , are similar to the 3D problem (see figure 4.1). Only two of these three dimensionless values are independent. The $\Delta\theta$ values for the six computational grids are:

$$\begin{aligned} \Delta\theta &= 0.049 , 0.098 , 0.196 , 0.393 , 0.785 \quad (\text{radian}) , \text{ or} \\ &= 2.8125 , 5.625 , 11.25 , 22.5 , 45.0 \quad (\text{degree}) . \end{aligned}$$

With these six grids for the different source frequencies, ω , and different control surface radii, r_c , a wide range of values of $\Delta l/\lambda$ and r_c/λ are tested:

$$\begin{aligned} \Delta l/\lambda &= 0.00103 , 0.00206 , 0.00412 , 0.00824 , 0.0165 , 0.0330 , \\ &\quad 0.0659 , 0.132 , 0.0659 , 0.132 , 0.264 , 0.528 \text{ and } 1.056 . \\ r_c/\lambda &= 0.0053 , 0.0105 , 0.021 , 0.042 , 0.084 , 0.168 , 0.337 , \\ &\quad 0.675 , 1.35 , 2.7 \text{ and } 5.4 . \end{aligned}$$

These value ranges can cover all the possible parameter distributions in the applied cases of this work.

The observation positions chosen for the present verification are at 72 homogeneously distributed points on a circle with a radius of r_0 from the position of the compact source:

$$r_0 = 50.0 , 75.0 , 100.0 \quad (m) .$$

For the verification of the numerical solution based on the 2D Fourier-transformed formulation of GUO, the following process is carried out: at first, the flow information on the control surface is analytically calculated at a special series of source times. The total time interval from the beginning to end of this time series is exactly ten periods of the harmonically fluctuating source. This time series is equidistant with a special step, Δt_0 , between the neighboring times, and this Δt_0 is calculated from the following relationship:

$$\Delta t_0 = \frac{10T_s}{N} , \quad N = 1024$$

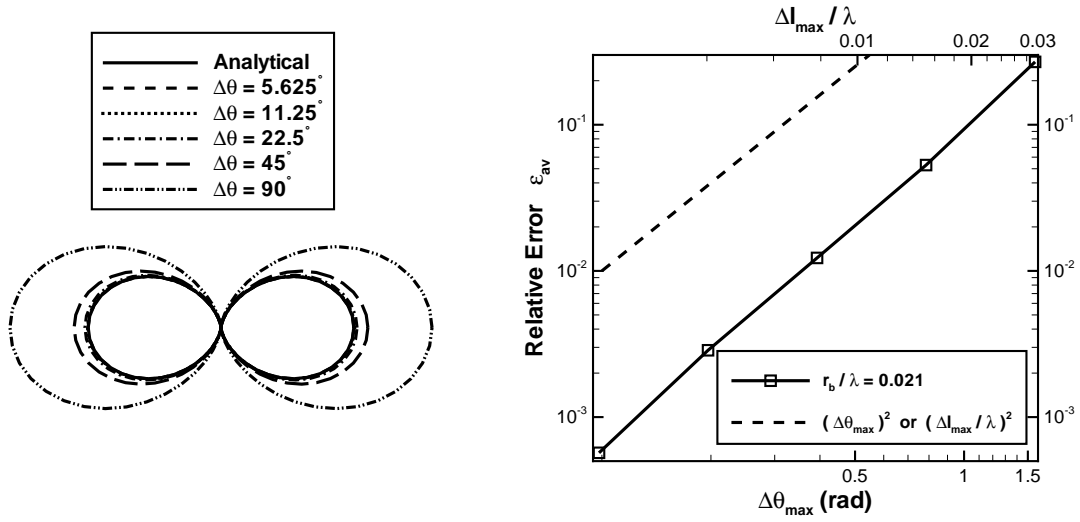
where T_s is the period of the harmonically fluctuating source. With this kind of temporal discretization, the solution of the numerical fast Fourier-transformation calculated by the code is the same as the analytical solution of the continuous FOURIER-transformation, because of the exact truncation of ten periods and exactly resolved frequency of the source. The error calculated through the comparison between the numerical and analytical solutions is a pure quadrature error due to the spatial approximation, which is denoted as the spatial discretization error, $\varepsilon_{av,s}$. Then, if the time step is changed to be a product of a non-round number with Δt_0 , the discretization error of the Fourier-transformation is caused. This error is in fact the temporal discretization error, $\varepsilon_{av,t}$, which can also be calculated by the subtraction of $\varepsilon_{av,s}$ from ε_{av} .

In figure 4.9(a) of page 62, the numerical directivities calculated with different angular resolutions are shown. If $\Delta\theta$ is more than 22° , there are large differences between numerical and analytical solutions. If $\Delta\theta$ is less than 11° , the numerical and analytical solutions are very close.

In figure 4.9(b) of page 62, the numerical relative errors versus $\Delta l/\lambda$, and versus $\Delta\theta$, are shown. The numerical scheme used is based on the midpoint quadrature. The errors versus spatial resolutions, $\Delta l/\lambda$ and $\Delta\theta$, are 2nd order accuracy. Thus, the numerical implementation is verified.

The above details of the numerical errors generate the following conclusions of the verification:

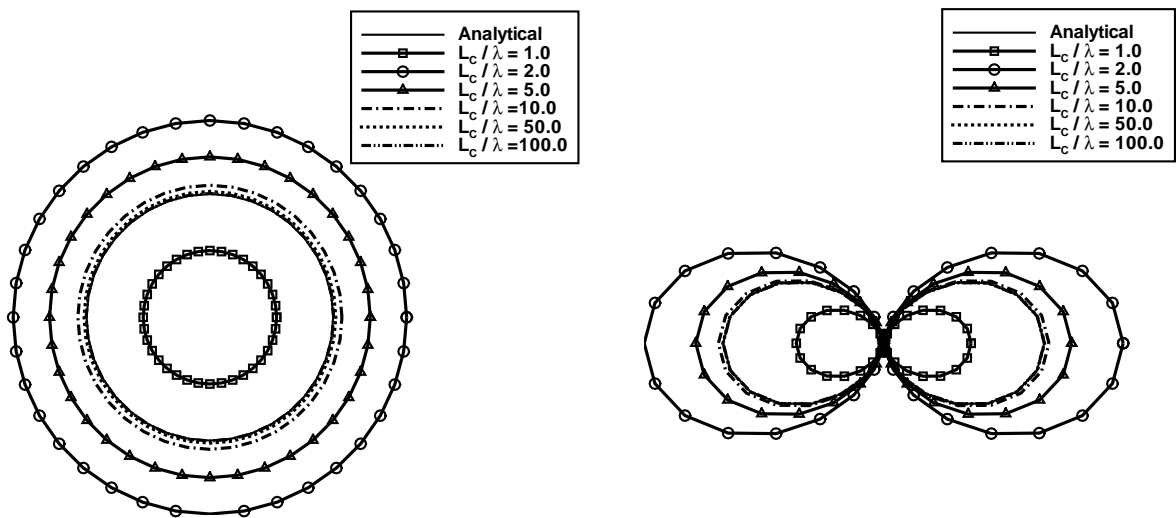
The numerical implementation is correct, because the errors versus spatial resolutions are 2nd order accuracy, just as the accuracy of the midpoint quadrature used.



(a) Numerical Directivity versus Angular Resolution

(b) Numerical Errors due to Spatial Approximation

Figure 4.9: Simulation of 2D-Dipole



(a) 2D-Monopole

(b) 2D-Dipole

Figure 4.10: Simulated Directivity Pattern versus Copy Length

According to the 3D verification results, the midpoint quadrature is good enough for the acoustic integral extension. The 2D verification results confirm the same conclusion as for the 3D cases.

If $\Delta\theta$ is less than 11° , the relative error is less than 0.5%

If the 2D monopole and dipole are simulated with the 3D formulation of FARASSAT, the copy length in the third direction is required. In figure 4.10(a), the simulated directivity patterns generated by a 2D monopole are presented with different copy lengths, L_c . If the copy length is more than 10 times the wavelength of the acoustic source, the numerical and analytical solutions can be very close.

In figure 4.10(b) of page 62, the simulated directivity patterns generated by a 2D dipole are presented with different copy lengths, L_c . If the copy length is more than 10 times the wavelength of the acoustic source, the numerical and analytical solutions are very close, just as with the verification case of the 2D monopole.

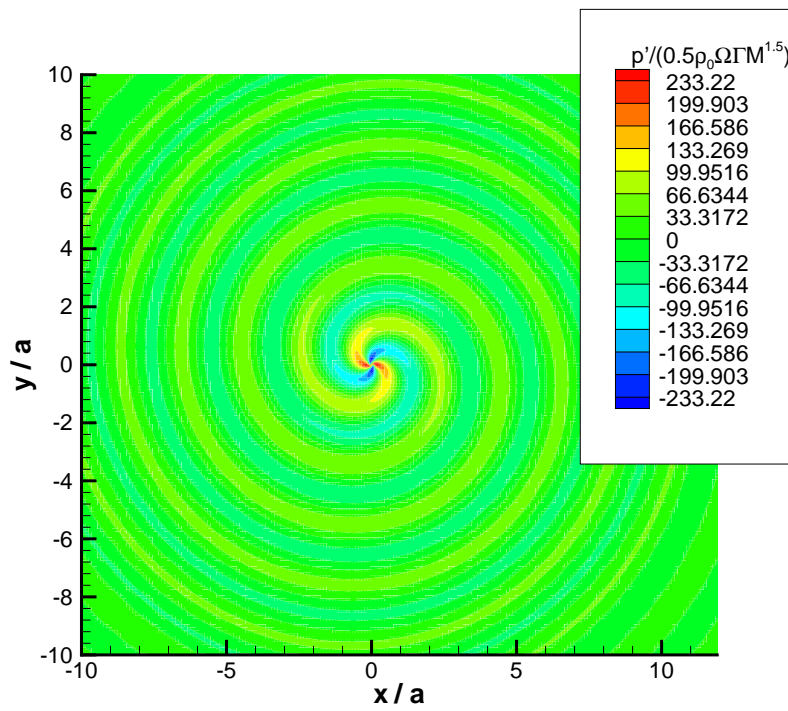
Therefore, a conclusion can be obtained that the copy length, L_c , should be at least 10 times the wavelength of the acoustic source, in order to achieve a correct simulation of 2D phenomena by using a 3D acoustic solver.

4.1.3 Co-rotating Line Vortices

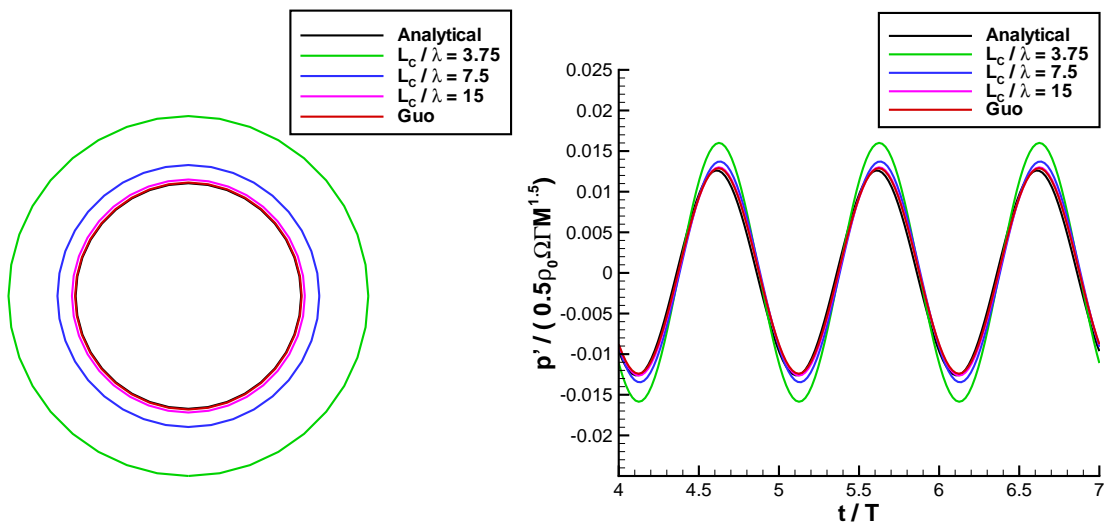
The analytical solutions used for this verification case are shown in appendix A.4. In an viscous infinite 2D medium, a stationary line vortex produces a time-independent velocity and pressure field. But Two such vortices, however, move in each other's velocity fields. Two equally strong and equally oriented vortices rotate with a constant angular velocity around the common center, and produce a fluctuating velocity and pressure field (for a fixed observer). If the velocities are relatively low, this field will be practically incompressible and have an explicit analytical solution. A small fraction of the energy, however, will radiate away as sound from this incompressible near-field. For a physically consistent problem (it is not possible in an non-viscous medium to change the total amount of circulation), a third vortex with double, but opposite, vortex strength is positioned at the common center. By symmetry, this vortex will not move, but, of course, will contribute to the rotating motion of the other two. The pressure field generated by these three vortices is shown in figure 4.11(a) of page 64. The calculations based on this case are carried out for both the verification of the 2D and 3D acoustic solvers:

(1) Verification of 2D Aeroacoustic Solver

Because of the strong singularity at the line vortex center and the incompressible solution only constricted in the dynamic near-field, the control surface should be positioned in the region of r_b/a between 1.2 and 1.8, where 'a' denotes half of the distance between the two



(a) Pressure Fluctuation Field of Co-rotating Vortices



(b) Simulated Directivities of R.M.S. Sound Pressure

(c) Simulated Time-Histories of Sound Pressure

Figure 4.11: The Acoustic Field of Co-Rotating Vortices

co-rotating vortices (see figure A.3 of page 115), and r_b denotes the radius of the control surface. The r_b/a values of 0.5, 0.8, 0.9, 1.1, 1.2, 1.5, 1.8, 2.0, and 2.2 are tested, but only the r_b/a values of 1.2, 1.5 and 1.8 are good enough to produce numeric solutions similar to the analytical ones.

In figures 4.11(b) and 4.11(c) of page 64, the numerical solutions based on the formulation of GUO are similar to the analytical solutions, with respect to both directivity and time-history.

(2) Verification of 3D Aeroacoustic Solver

If the 2D aeroacoustic field of the co-rotating line vortices is simulated with the code based on the 3D formulation of FARASSAT, the copy length, L_c , in the third direction should be used. In figures 4.11(b) and figure 4.11(c) of page 64, the copy length effects are shown. Similar to the 2D monopole and dipole cases, the critical copy length is about $10 \sim 15\lambda$, for a case of $r_b/\lambda = 0.02$ and $r_0/\lambda = 1.75$, where λ denotes the constant wavelength of sound pressure generated by the co-rotating vortices. It can be concluded: if the copy length, L_c , is more than $10 \sim 15\lambda$, the 3D aeroacoustic solver simulates the 2D aeroacoustic field of the co-rotating line vortices very well.

4.1.4 2D Monopole in Flow

The acoustic field generated by a monopolar line source placed in a uniform flow is computed through the three methods of FARASSAT, GUO and LOCARD. The source is located at the origin of the reference frame and the uniform flow is in the +x direction. The complex potential for the monopole is given by DOWLING and FFOWCSEWILLIAMS [17] as:

$$\phi(x, y, t) = A \frac{i}{4\beta} e^{i(\omega t + M k x / \beta^2)} H_0^{(2)} \left(\frac{k}{\beta^2} \sqrt{x^2 + \beta^2 y^2} \right) \quad (4.2)$$

The details of the analytical solution are shown in appendix A.5. For the verification, the following source parameters are used:

$$\begin{aligned} M &= U_0/c_0 = 0.2; \\ \omega &= 4272.5(\text{rad/s}) \\ A &= 0.034(\text{m}^2/\text{s}) \end{aligned} \quad (4.3)$$

Results show that: (1) At the observation direction of 90° , vertical to the flow direction, the simulated sound pressures based on all the three methods are similar; (2) The convective effect is shown the mostly at the observation direction of 0° . At the observation direction of 0° , the method of FARASSAT and GUO make about 5 % relative errors.

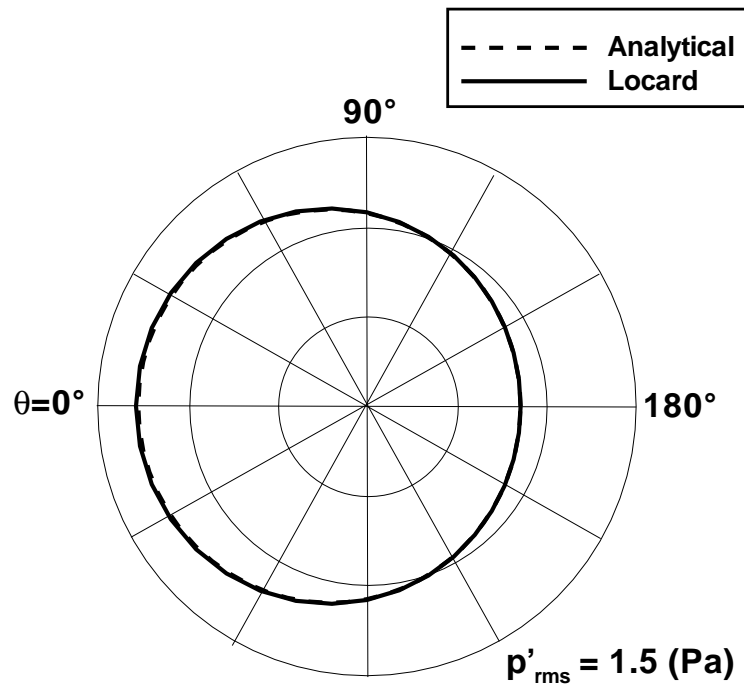


Figure 4.12: Simulated Directivity of 2D Monopole in Uniform Flow at $Ma=0.2$

They underpredict the sound pressure at the 0° , against the flow direction, and overpredict the sound pressure at the 180° , along the flow direction.

In figure 4.12, the directivity simulated by the code based on the formulation of LOCARD is shown. The agreement between the numerical and analytical solutions are very good.

4.2 Validation with DNS Results

The aeroacoustic DNS results of the unsteady flow around a circular cylinder at $Re_D = 150$ by INOUE [38] are used for the validation. Through the comparisons between the DNS and the current simulation based on the hybrid CFD/FW-H approach, the physical-mathematical modeling of the current code can be validated. The dynamic near-field of the current simulation is also compared with the other experimental and numerical results published. It is proven that the code produces a similar dynamical near-field and acoustic far-field as the validation benchmarks. It is confirmed that the governing equation system solved by the current code captures the main physics, although some physical and numerical approximations are required in the modeling.

Before the comparisons between the acoustic far-field calculated by INOUE and the current code, a short summary of the mathematic modeling and numerical schemes of IN-

OUE's code is presented in section 4.2.1. Then, the computational parameters of INOUE's and the current simulation are presented in section 4.2.2. The comparisons of the flow quantities in the dynamic near-field between the current simulation and INOUE's, the other numerical and experimental results published, are shown in section 4.2.3. Finally, the validation results based on the comparison of the acoustic far-field simulated by the current code with the benchmark of INOUE's DNS, are concluded in section 4.2.4.

4.2.1 General Features of DNS

The benchmark of the current validation is the aeroacoustic DNS of INOUE, a direct numerical simulation of the generation and propagation of the sound produced by a two-dimensional stationary circular cylinder in a uniform cross-flow. DNS means that the unsteady compressible Navier-Stokes equations are solved over the entire region from the dynamical near-field to the acoustic far-field with highly accurate numerical schemes both in space and time in order to precisely capture the acoustic pressure fluctuation, which is usually much smaller than the dynamical pressure fluctuation in the near field. Such a DNS of aeroacoustic phenomena requires a large amount of computer resources, even though it is only two-dimensional. But such a study is without additional approximation modeling for solving the basic governing equations; therefore, its results can be used as the validation benchmark for the hybrid CFD/FW-H simulations with the simplifications through the conditions such as low Mach number, compactness of the source region, etc.

In INOUE's DNS, the two-dimensional unsteady compressible Navier-Stokes equations were solved by a finite difference method. For spatial derivatives, a six-order-accurate compact PADE scheme (fourth-order-accurate at the boundaries) proposed by LELE [43] was adopted. The fourth-order RUNGE-KUTTA scheme was used for time-integration. A buffer region was used to damp the pressure waves before the waves reached the outer boundary of the computational domain where the non-reflecting boundary conditions (POINTSOT and LELE [63]) were used. Adiabatic and non-slip conditions were used on the cylinder surface. The grid and domain-size independence was established for the solutions published. Initial flow fields were given by potential flows, except for the boundary layer on the cylinder surface, where a tangent-hyperbolic filter was applied so that the non-slip condition on the cylinder surface and the potential flow condition at the boundary layer outer edge were satisfied. The details of the computational domain, grid and time step will be shown in the next section compared with the corresponding parameters of the current simulation.

The extension and structure of the disturbed flow around the cylinder are highly dependent on the REYNOLDS number, $Re_D = \frac{\rho V_\infty D}{\mu}$, where ρ is the fluid density, μ the viscosity, V_∞ the undisturbed velocity, and D the diameter of the cylinder. In the subsonic cases, the Mach number, $Ma = \frac{V_\infty}{c_\infty}$, where c_∞ is the undisturbed sound speed in the far field, has little influence on the flow field. The solutions at $Re_D = 150$ while $Ma=0.1$,

0.2 and 0.3 are calculated by INOUE et al [38]. The current simulation is compared with that of INOUE et al. at $Re_D = 150$ and $Ma=0.2$.

4.2.2 Computational Parameters

(1) Computational Domains and Grids

The computational domain of the DNS by INOUE et al. is a circle of an O-grid system, which is divided into three regions of different grid spacing: a surface region ($0.5 \leq r \leq 1.0, -\pi \leq \theta \leq \pi$), a sound region ($1.0 \leq r \leq 100, -\pi \leq \theta \leq \pi$), and a buffer region ($100 \leq r \leq 1500, -\pi \leq \theta \leq \pi$). The r is the dimensionless radius nominated with the diameter of the cylinder and with the origin at the center of the cylinder. The grid spacing in the θ -direction is uniform with $\Delta\theta = 0.72^\circ$, namely 503 points per circle.

(a) The surface region:

The grid spacing in the surface region is fine enough to analyze the boundary layer on the cylinder surface. The number of grid points within the boundary layer of the cylinder for $Re_D = 150$ is 16 in the r -direction, while the thickness of the boundary layer is estimated by $\delta \sim \frac{1}{\sqrt{Re}}$ and $\delta \sim 0.08$ for $Re_D = 150$. The minimum spacings are $\Delta r_{min} = 0.005$ adjacent to the cylinder surface. The increment of the spacing is very small when $r \leq 1.0$ and does not exceed 4% in the whole surface region.

(b) The sound region:

The grid spacing is larger than that in the surface region, but still small enough to capture sound pressure waves. The minimum spacings are $\Delta r_{sound} = 0.2$ adjacent to the boundary between the surface and sound regions. The increment of the spacing does not exceed 4 %.

(c) The buffer region:

The grid spacing is prescribed so that the pressure waves damp with increase in distance and become sufficiently small before reaching the outer boundary. The maximum spacings are $\Delta r_{buffer} = 20.0$ adjacent to the outer boundary of the region. The increment of the spacing does not exceed 9 %.

The spacings among the three regions are connected smoothly by using hyperbolic-tangent curves. The total number of grid points is 438113, 871(r -direction) \times 503 (θ -direction), in which 160×503 grid points are distributed in the buffer region. Only the results obtained in the surface and sound regions are used for analysis.

The current computational domain of the dynamical near-field is a rectangle ($-10 \leq x \leq 20, -10 \leq y \leq 10$) of a block structured H-grid system with an O-grid subregion ($0.5 \leq r \leq 5.0, -\pi \leq \theta \leq \pi$) directly around the cylinder. x, y and r are the dimensionless coordinates nominated with the diameter of the cylinder and with the origin at the center of the cylinder. The grid spacings both in the r and θ -directions are non-uniform. The

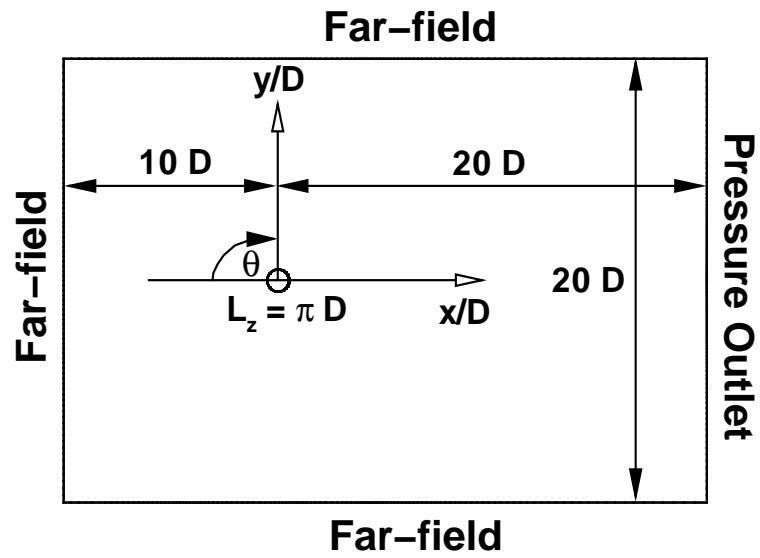


Figure 4.13: Computational Domain, Boundary Conditions and Reference Frame ($Re_D = 150$)

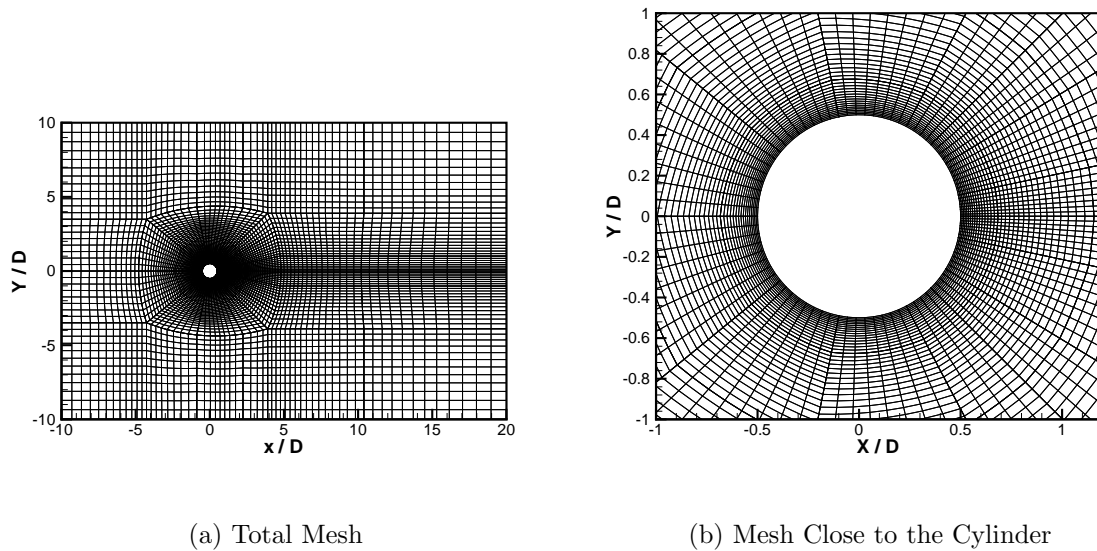


Figure 4.14: Computational Grid for the Case of $Re_D = 150$

geometry of the computational domain and the coordinate system are shown in figure 4.13 of page 69. In the O-grid region, the grid spacing is finer than that outside.

(a) The O-grid region:

The minimum spacings are $\Delta r_{min} = 0.007$ adjacent to the cylinder surface, which are small enough for the dimensionless wall distance, y^+ , being of the order of 1 at $Re_D = 150$ and resolve the boundary of cylinder surface well. The grid spacings are increased in the normal direction of the cylinder wall with a stretching factor of 1.032 inside of the O-grid.

(b) The region outside the O-grid:

Outside of the O-grid, the stretching factor is increased to a maximum of 1.05. This region should connect the inner O-grid region and outer boundary so that there is no small angle of the volume cell and the boundary conditions are accurate enough on the outer boundary of computational domain.

The total amount of hexahedral control volumes of this computational grid in the plane of $(r \times \theta)$ is 17792. The number of grid points along the wake centreline is 93. 77 points are used in the normal direction of the cylinder at $\theta = \pm 90^\circ$, and 97 on the circumference of the cylinder. The computational grid is shown in figure 4.14(a) and figure 4.14(b) of page 69.

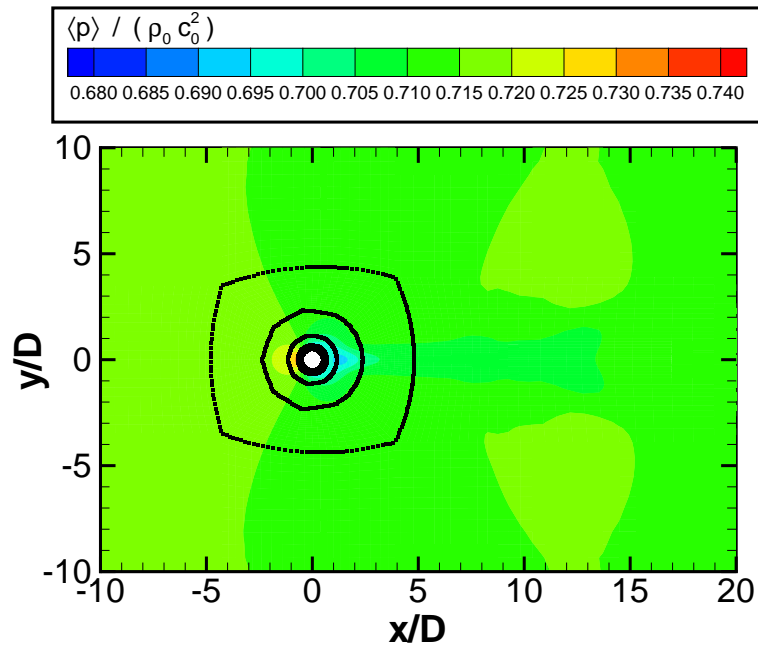
According to the many preliminary tests, the domain and grid independence has been established for the solution published by INOUE et al. The grid independence is also established by the current results. The current computational domain is much smaller than that of INOUE et al. But this is what the author wished to test, how accurate the acoustic far field is simulated by the current hybrid method, with which, only in a small near-field, the unsteady compressible Navier-Stokes equation is solved and then the acoustic far field is extended through a integral method. The influence of the computational domain will be discussed next.

(2) Time steppings

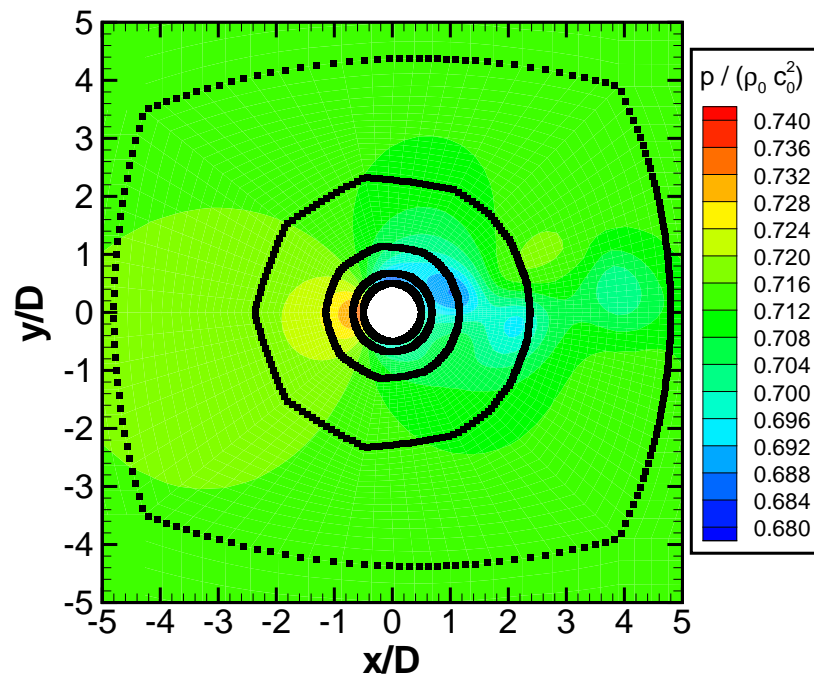
The time step, $\frac{\Delta t U_\infty}{D}$, used by INOUE et al. is 0.002; and 0.00158 by the current simulation, corresponding to a CFL number of 2.2.

(3) Control Surfaces for the Acoustic Extension

Five control surfaces used for the acoustic extension are shown in figure 4.15(a) and figure 4.15(b) of page 71, with the background of the contour picture of the average pressure and instantaneous pressure respectively. The control surface closest to the cylinder is denoted as No.1; then from inner to outer, the control surfaces are denoted as No.2 to No.5.



(a) Control Surfaces in the Total CFD Domain, Background: Mean Pressure Field



(b) Control Surfaces in the Local Field Close to the Cylinder, Background: Instantaneous Pressure Field

Figure 4.15: The Positions of Five Control Surfaces, Background: Pressure Field

4.2.3 Dynamical Near-field

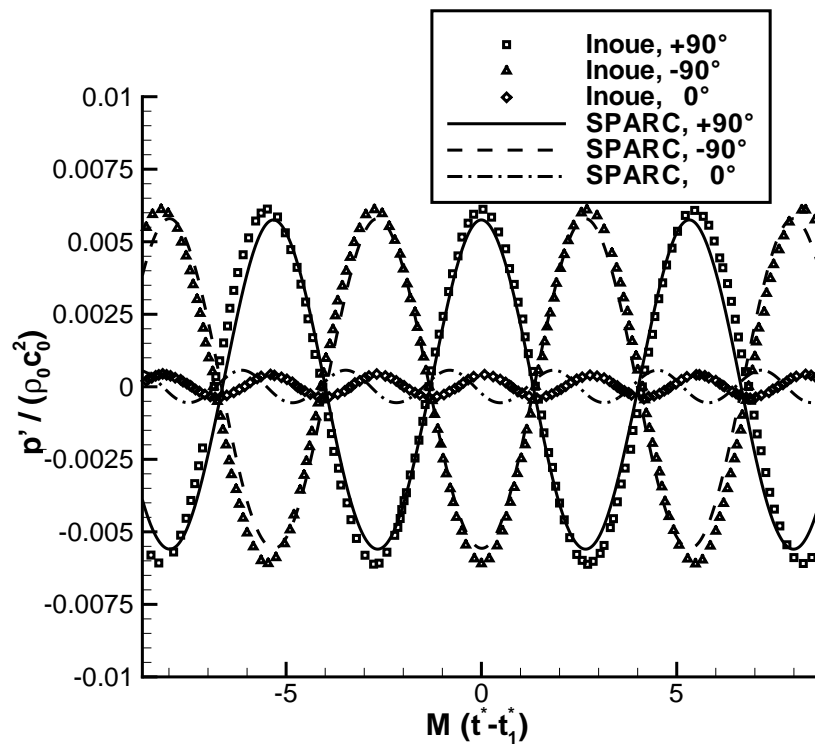
The flow field around the cylinder can be usually divided into four regions: (1) one narrow region of retarded flow before the stagnation point, (2) two boundary layers attached to the surface of the cylinder, (3) two sidewise regions of displaced and accelerated flow above and below the cylinder, (4) one wide downstream region of separated flow called the wake. A particular feature of the flow around a bluff body like a circular cylinder is a succession of transitions in various regions of the flow. The transition may take place in the wake, in the shear layer between the accelerated flow and the wake, and in the boundary layer attached to the cylinder. Depending on the REYNOLDS number, the state of flow may be fully laminar, any one of the above three transitions, or fully turbulent. For the validation example at $Re_D = 150$, the flow state is fully laminar with a periodic wake due to the periodic laminar vortex shedding from the boundary layer of the cylinder. At $Re_D = 150$, the randomness of vortex shedding in the span direction from the surface of cylinder is small. According to experiments, the correlation length of vortex shedding is over $20D$. Such a flow field can be approximately treated two-dimensionally without any three-dimensional disturbances due to the instabilities or transitions.

The numerical near-fields provide not only the inputs for the further acoustic computation, but also the details for the identification of the sound generation mechanisms. The results show that sound pressure waves are generated primitively by vortex shedding from the cylinder into its wake. When a vortex is shed from one side of cylinder, a negative pressure pulse is generated from that side, whereas a positive pressure pulse is generated from the other side; alternate vortex shedding from the upper and lower sides of the cylinder produces negative and positive pulses alternately and thus produces sound pressure waves on both sides. Figures 4.16(a) and 4.16(b) of page 73 show the fluctuations of the surface pressures and forces acting on the cylinder. In the current simulation, the pressure fluctuation distribution on more positions on the whole surface of cylinder is measured and shown in figure 4.16(a). Figure 4.16(c) of page 73 shows the mean pressure coefficient, $\overline{C_p}$, on the cylinder surface. The comparison between the current simulation and INOUE's gives a good agreement.

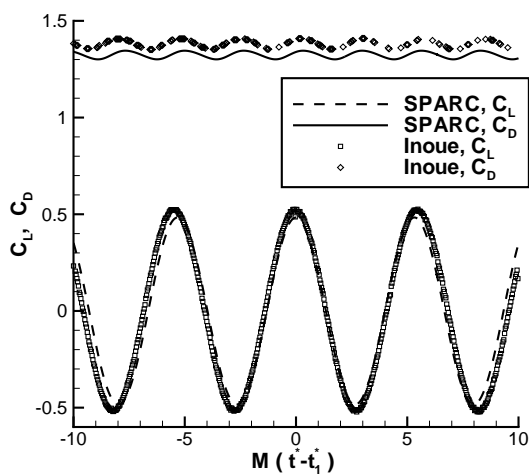
Compared with the DNS, the following inferences can be given:

The amplitude of surface pressure fluctuation at $\theta = \pm 90^\circ$ is much more than that at $\theta = 0^\circ$, and the amplitude of lift coefficient fluctuation is also much more than that of drag coefficient fluctuation in both the current and DNS results. This means that the lift dipole dominates the pressure fluctuation field, and the influence of the drag dipole is negligible. The main sound sources are located about the upper and lower top of the cylinder surface where the vortex sheds away periodically.

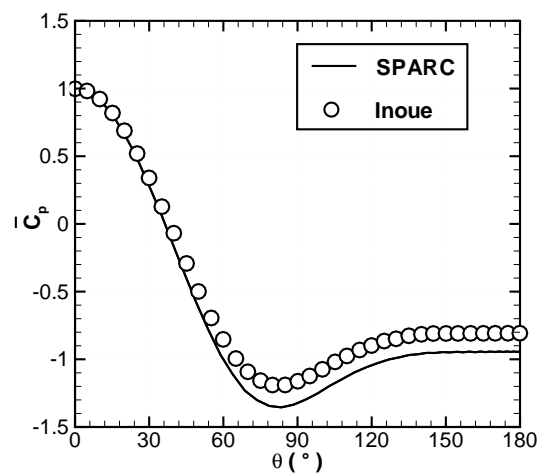
The current numerical results of the fluctuation amplitudes of the surface pressures, lift coefficient and drag coefficient are a little smaller than that of the DNS, but absolute values of the mean pressure coefficients are a little larger. These differences



(a) Surface pressure



(b) Lift and Drag Coefficient



(c) Mean Pressure Coefficient

Figure 4.16: Near-field Quantities of Flow around a Circular Cylinder, $Re_D = 150$.
 ($p' = p - p_\infty$, $M = U_\infty/c_0$, $t^* = U_\infty t/D$)

	St	$-\bar{C}_{pb}$	C_L^{rms}	\bar{C}_D	L_z/D
Present (num.)	0.186	0.850	0.342	1.224	20.0
Posdziech (num., 2001)	0.184	0.848	/	1.313	140.0
Henderson (num.,1995)	0.185	0.885	/	1.333	56.0
Persillon et al. (num.,1998)	0.181	/	0.338	1.268	16.46
Zhang et al. (num.,1995)	0.191	/	0.403	1.418	12.0
Norberg (2002)	0.183 (exp.)	/	0.356 (num.)	/	/
Williamson (exp., 1989)	0.184	0.856	/	/	/

Table 4.2: The Mean Integral Quantities ($Re_D = 150$)

may be due to the blockage effect of the small computational domain used. The investigation results by POSDZIECH and GRUNDMANN [64] show that the extension of the computational domain should at least have a blockage ratio of $L_z/D=70$ for the flow at $Re_D = 200$ to yield domain-independent results. The blockage ratio, L_z/D , in the current simulation is 20, and there are visible blockage effects.

The STROUHAL numbers of the lift and drag fluctuations are measured. St is used here to denote the STROUHAL number of the lift fluctuation and St_D that of the drag fluctuation. For both simulations, $St = 2 \cdot St_D$. The St measured in the current simulation is 0.186 as well as 0.183 from the DNS. The small increment of the current STROUHAL number is also due to the blockage effect.

In order to quantitatively validate the near-field simulation, the other commonly evaluated mean flow quantities, such as the mean base-pressure coefficient, \bar{c}_{pb} , the root mean square lift coefficient, c_L^{rms} , and the mean drag coefficient, \bar{c}_D , are also measured by the current calculation and compared with the other numeric and experimental results (see table 4.2). Besides, the root mean square drag coefficient, $c_d^{rms} = 0.0158$, and the mean separation angle, $\bar{\theta}_s \approx 108.5^\circ$, are also measured by the calculation. The integration time for the averaging, $T^* = \Delta t V_\infty / D$, is about 150. Because of the scattering of the computational parameters, such as the blockage ratio, integration time, etc., and the differences of experimental conditions, such as turbulence inflow, surface roughness, wall blockage, end effect, etc., the measured mean quantities dispersed somewhat. But the comparisons in table 4.2 show a good similarity and give a validated base for the further acoustic simulations, since all the differences can be assigned solid reasons. In the next section, the difference of mean flow quantities will be compared with that of far-field acoustic quantities.

4.2.4 Acoustic Far-field

A well-known phenomenon of the sound generated by flow past a circular cylinder is the so-called Aeolian tone. STROUHAL (1878) found that the pitch of the Aeolian tone was only dependent on flow speed and diameter of the cylinder. RAYLEIGH (1921) suggested the dimensionless constant, fD/V_∞ , as a STROUHAL number. STROUHAL has found fD/V_∞ is about 0.185 for the high REYNOLDS number flow past a circular cylinder. Nowadays the more accurate STROUHAL number for a wide range of REYNOLDS numbers have been measured experimentally and numerically. The STROUHAL number of far-field sound for $Re_D = 150$ is 0.183 measured by the DNS and 0.186 by the current simulation. Compared with the near-field STROUHAL number of the surface pressure, lift and drag fluctuation, the cause of the aerodynamic sound generation can be deduced. The STROUHAL number of the surface pressure and lift fluctuation is the same as that of the far-field sound, whereas the STROUHAL number of the drag fluctuation is exactly doubled. Therefore, the far-field sound generation at $Re_D = 150$ is obviously due to the dominant lift fluctuation caused by the stronger surface pressure fluctuation near the vortex shedding points on the surface of the cylinder. In practice, the tonal sound generated by the flow past a bluff body may be locked to the natural frequency of the solid body to produce a synchronization of vibration. To predict the pitch of this tonal sound is important.

Generally speaking, when a flow passes a bluff body, the radiated sound is the sum of the following three parts: (1)a (dominant) dipolar contribution (surface integration of surface pressure fluctuation), (2)a quadrupolar contribution (volume integration of Lighthill's stress fluctuation) and (3)the scattering by the solid surface (usually small for a compact round contour). The mathematic models for these three parts of sound have been discussed in chapter two. Here, the dominant dipolar contribution due to the lift fluctuation is simulated and plotted in detail for spatial distribution (directivity pattern and distance effect), time history and frequency spectrum. Through the comprehensive comparisons between the current simulation and the DNS, the current code is validated:

Spatial Distribution of Overall Sound Pressure in the Acoustic Far-field

The directivity patterns calculated based on the formulations of FARASSAT, GUO and LOCARD are in good agreement with the DNS result of INOUE (see figures 4.18(a), 4.18(b) and 4.18(c) of page 78). The formulation of LOCARD is somewhat the best with respect to the agreement to the directivity result of INOUE. The distance effect is in very good agreement with $p'_{rms} \sim 1/r^{\frac{1}{2}}$ for the 2D cases; and $p'_{rms} \sim 1/r$ for the 3D cases (see figure 4.17 of page 76). If the copy length, L_c , is large enough, in a wide range of observation distances, the formulation of FARASSAT gives also a 2D cylindrical wave spreading. The comparison of the results based on the methods of FARASSAT, GUO and LOCARD extended from the control surface No. 2 are shown in figure 4.18(d) of page 78.

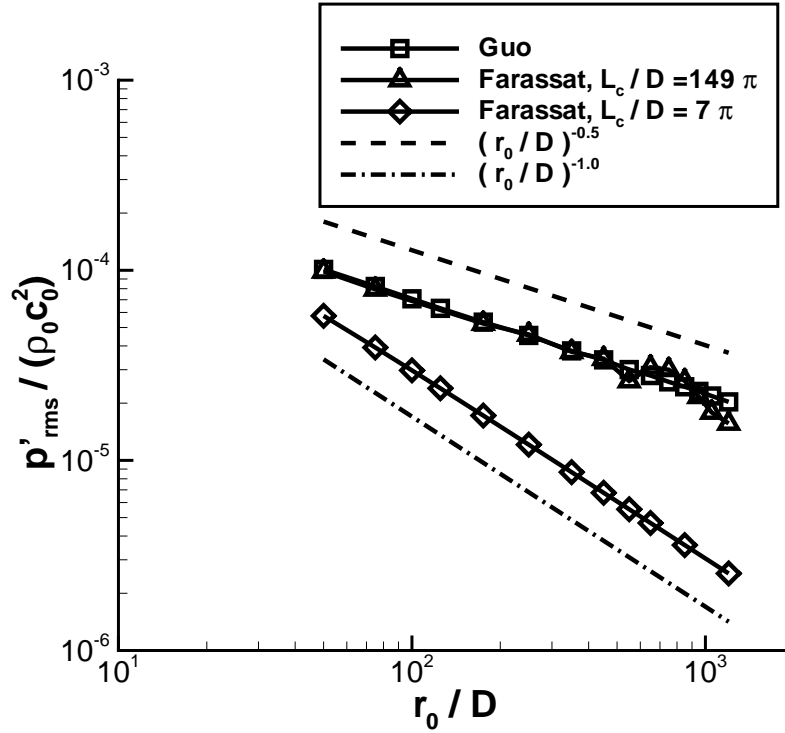


Figure 4.17: Simulated Distance Effect of Sound Pressure, CS No.2, $Re_D = 150$

Time History of Overall Sound Pressure in the Acoustic Far-field

The time history of the acoustic far-field is a simple harmonic fluctuation. The current simulation has a similar amplitude to INOUE's (see figures 4.19(a), 4.19(b) and 4.19(c) of page 79). There is a phase shift in the case of LOCARD, due to the convective effect. The frequency spectrum is a discrete tonal band with the dominant STROUHAL number of 0.186. The comparison of the results based on the three methods of FARASSAT, GUO and LOCARD extended from the control surface No. 2 are shown in figure 4.19(d) of page 79.

The following validations are also made for the acoustic extension from the near-field CFD data to the far-field, based on the porous FW-H integration:

Copy Length

A copy length is required for the code based on the three-dimensional formulation of FARASSAT to use the two-dimensional CFD inputs to calculate the acoustic far-field. If the simulated object is physically two-dimensional, namely two-dimensional flow and acoustic field, the copy length obtained from the previous analytical verification is appropriate to simulate the peak amplitude and fluctuation phase of the far-field sound. The case of the comparison between the current simulation and the DNS is just such a case. But if the simulated object is physically three-dimensional,

an appropriate copy length for the simulation of sound peak amplitude should be among the correlation length of the vortex shedding in the span width, the geometrical length of the cylinder and the copy length obtained from the previous 2D analytical verification. If an improper copy length is used, the simulated peak amplitude of sound pressure may be over or under-predicted. For the relatively simpler case here, namely using 3D acoustic solver to simulate the 2D aeroacoustic phenomena, the problem of the copy length is simply whether the copy length is long enough, or not. Results of the current simulation show that the simulated far-field sound pressures, based on the 3D formulation of FARASSAT, are convergent to that, based on the 2D formulation of GUO, if a sufficient copy length is used (see figures 4.20(a) and 4.20(b) of page 80). The sufficient copy length for this case is also in the range of $10 \sim 15\lambda$, just like in the previous verification examples, where λ is the wavelength of the periodic lift fluctuation on the cylinder surface. Of course, the 2D aeroacoustic solvers are the most appropriate here to simulate the acoustic far-field without the problem of copy length and very efficiently.

Position of Control Surface

The sound computation is highly dependent on the accuracy of the flow field produced by the CFD calculation. The control surface Nos. 4 and 5 which are near the outer boundary of the computational domain, yield too large an over-prediction, because of the strong influence of the boundary conditions and relatively coarser spatial resolution situations. The far-field boundary condition used in the CFD simulation is not really non-reflecting. This seems to give a large influence on the acoustic simulation. But the aeroacoustic simulations, based on the control surfaces No. 1 to No. 3, give a good agreement with the DNS by INOUE (see figures 4.19(a), 4.19(b) and 4.19(c) of page 79).

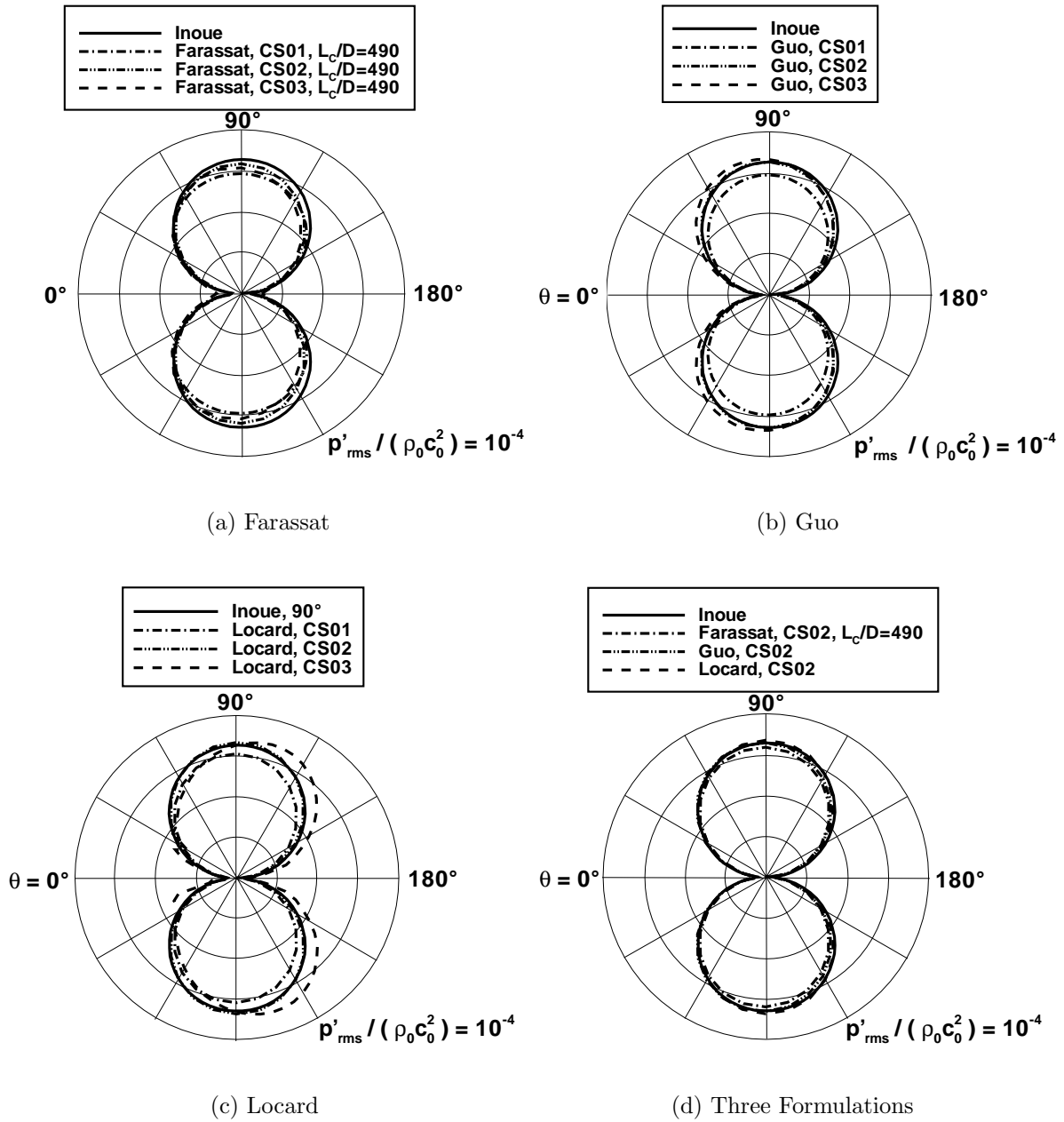


Figure 4.18: Comparisons of Directivity, $r_0/D = 75$

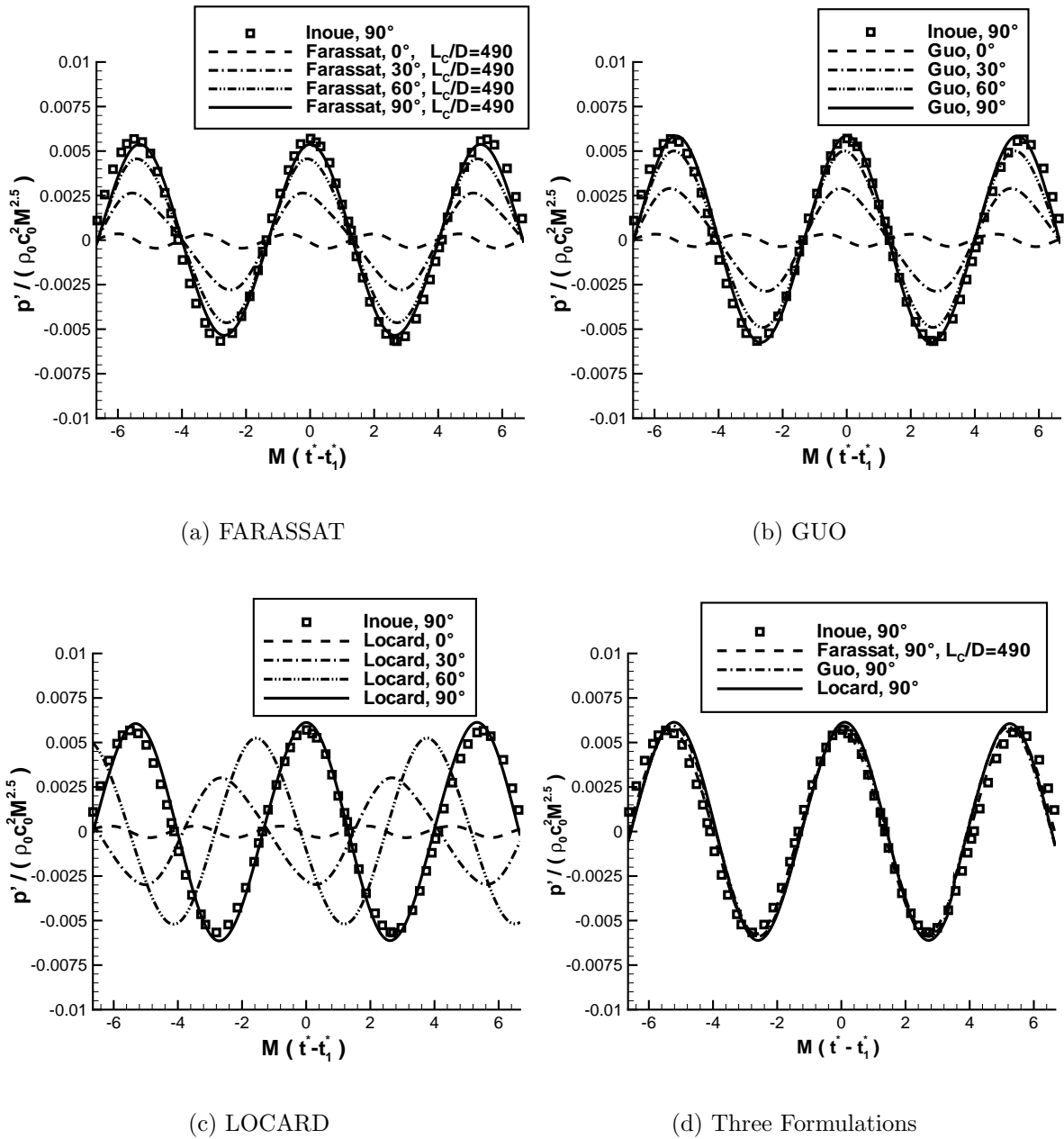
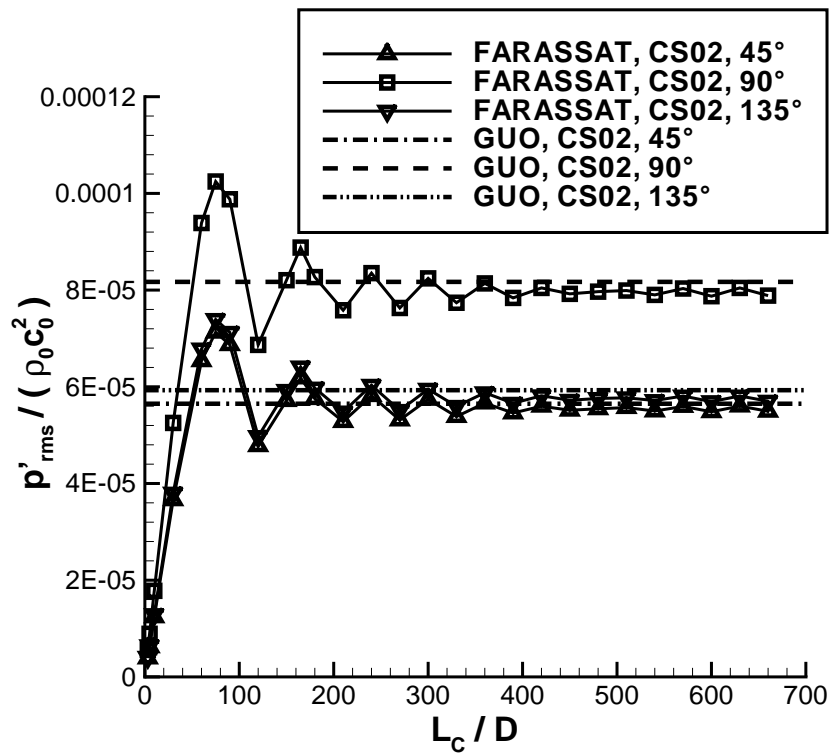
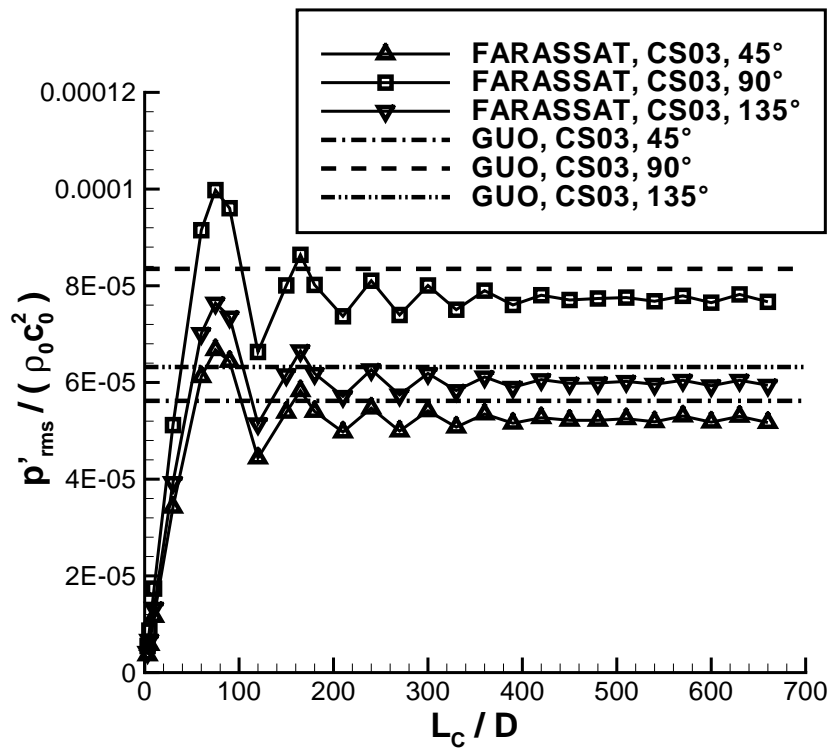


Figure 4.19: Comparisons of Time-History of Sound Pressure, $r_0/D = 100$, CS No. 2. ($p' = p - p_\infty$, $M = U_\infty/c_0$, $t^* = U_\infty t/D$)



(a) CS No. 2



(b) CS No. 3

Figure 4.20: Total Sound Pressure vs Copy Length, $r_0/D = 75$

Chapter 5

Noise from Flow around Cylinder at $Re_D = 3900$

On the basis of the comprehensive verification and validation of the computer program used, the numerical simulation of the acoustic far-field of the flow past a stationary circular cylinder at $Re_D = 3900$ is carried out by means of the hybrid method with the LES and the (porous) FW-H approach. The simulation results show that the acoustic far-field is primitively dominated by the vortex shedding from the cylinder surface. The acoustic far-field is found to possess a field of two dipoles, namely one relatively strong lift dipole and one relatively weak drag dipole. The quadrupole noise is still negligible compared with the noise due to the lift and drag dipoles at $Re_D = 3900$. In contrast to the case of $Re_D = 150$, the vortex shedding is irregular and three dimensional. Thus a broadband stochastic noise field is generated. The whole features of the acoustic far-field, namely the overall sound level, the directivity and the frequency spectrum, are calculated, and compared with the experimental results. The near-field integral quantities are also compared with the DNS results to ensure a good first step of CFD.

5.1 Computational Parameters

In figure 4.13 of page 69, the computational domain for $Re_D = 3900$ is shown, which is the same as for $Re_D = 150$. The boundary conditions are also shown in figure 4.13. At the inflow, and at the boundaries in the normal direction, the laminar far-field boundary conditions are prescribed. For those, the velocity, U_0 , normal to the inflow boundary, and its temperature, T_0 , are prescribed to yield the REYNOLDS number, $Re_D = \rho_0 U_0 D / \mu_0 = 3900$, and the MACH number, $M_0 = U_0 / c_0 = 0.2$. The temperature, T_0 , is also used for an isothermal boundary condition on the cylinder wall. On the cylinder wall, the non-slip velocity condition is applied. At the outflow boundary, the far-field condition with the static pressure, p_0 , of the free stream is prescribed. This boundary condition is known as to be reflective. In the span direction, periodic boundary conditions are used. The span width of the computational domain is set to πD .

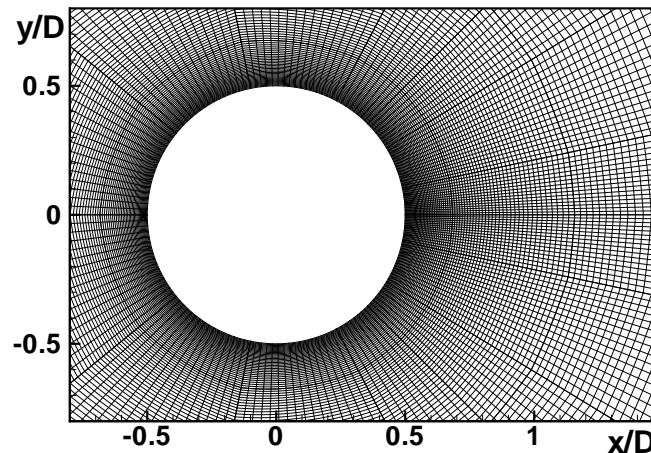


Figure 5.1: Computational Grid Close to the Cylinder ($Re_D = 3900$)

In this computational domain, a block structured H-grid has been used with an O-grid with radius $5D$ around the cylinder. The height of the first cell on the cylinder surface is $3.5 \times 10^{-3}D$, to make the dimensionless distance, y^+ , to be of the order of 1. The grid is stretched in the normal direction of the cylinder wall with a factor of 1.032 inside the O-grid. Part of this grid is shown in figure 5.1. Outside the O-grid, the stretching factor is increased to a maximum of 1.05. The number of grid points along the wake centerline is 185. In the normal direction at $\theta = \pm 90^\circ$, 153 points are used and on the circumference of the cylinder 193. In the span direction, 33 grid points are used. The total amount of hexahedral control volumes is 1138688. The spatial resolution for $Re_D = 3900$ is twice as fine as for $Re_D = 150$, namely 2^3 times the number of grid points are used to discretize the computational domain for $Re_D = 3900$ as for $Re_D = 150$ by using the same geometric topology of blocking.

The code used for the simulation has full multigrid capability. Therefore the computation was started from uniform flow on the coarsest grid level and run there until periodic vortex shedding occurred. This solution was then transferred to the next finer grid level, and the simulation continued. On the finest grid, the simulation was run for ten shedding cycles before time averaging and acoustic source information quantities were begun. The acoustic source information was sampled at a dimensionless time interval of $\Delta t^* = \Delta t U_0 D \approx 0.1056$ in a total temporal space of $T^* \approx 162$. The temporal resolution is fine enough with $\Delta t/T_0 \approx 0.02$. Therefore, the 2rd order temporal discrete schemes are used for the acoustic extension.

The control surfaces used to store the acoustic source informations for $Re_D = 3900$ are

the same as for $Re_D = 150$ (see figures 4.15(b) and figure 4.15(a) of page 71). But the spatial resolution of 192×32 on the control surface is finer. The linear resolutions on the five control surfaces are all fine enough with $\Delta l/\lambda_0 < 0.01$, and the angle resolutions on these control surfaces are also good enough with $\Delta\theta < 3^\circ$. Therefore, the 2nd order spatial and temporal discrete schemes are used for the acoustic extension.

5.2 Dynamical Near-field

The main objective of this work is to simulate the acoustic far-field. Therefore, only the following mean integral quantities are presented in table 5.1 to show the quality of the simulation of the time-averaged flow quantities. More details about the mean integral quantities, mean flow field and turbulence statistics have been published by FRANKE (2002) [29]. All the mean integral quantities, mean flow field and turbulence statistics of the calculation shown in the current work are in good agreement with the DNS.

	St	$-\overline{C}_{pb}$	C_L^{rms}	C_D^{rms}	\overline{C}_D	$\overline{\theta}_s(^{\circ})$	L_r/D	L_z/D
Present	0.209	0.860	0.074	0.029	0.963	88.3	1.57	20.0
DNS by Ma [52]	0.219	0.840	-	-	-	-	1.59	20
DNS by Tremblay [79]	0.220	0.920	-	-	1.03	85.7	1.30	18

Table 5.1: Comparisons of Mean Integral Quantities ($Re_D = 3900$)

In the above table, St denotes the STROUHAL number, $-\overline{C}_{pb}$ denotes the mean back pressure coefficient, C_L^{rms} denotes the root mean square lift coefficient, C_D^{rms} denotes the root mean square drag coefficient, \overline{C}_D denotes the mean drag coefficient $\overline{\theta}_s$ denotes the mean separation angle, L_r/D denotes the mean length of the circulation region, and L_z/D denotes the blockage ratio.

5.3 Acoustic Far-field

The comprehensive features of the acoustic far-field generated by the circular cylinder in the flow at $Re_D = 3900$ and $Ma=0.2$ are calculated, which are the overall sound pressure level, directivity and frequency spectrum. Results show that sound pressure waves are generated primarily by vortex shedding from the cylinder surface into its wake, which are related to the so-called deterministic aeolian tone sound at discrete frequencies, and by the turbulence fluctuations in the wall boundary and wake, which are related to the so-called non-deterministic (stochastic) broad band sound in a wide range of continuous frequencies. Compared with the acoustic far-field generated by the same cylinder in the

flow at $Re_D = 150$ and $Ma=0.2$ discussed in the previous chapter, the dipolar nature of the generated acoustic field is still confirmed, and the lift dipole dominates the total sound pressure distribution, although the drag dipole makes more contributions than at $Re_D = 150$. Due to the turbulence in the wall boundary and wake, a broad frequency band sound field in higher frequencies is generated, which does not exist at $Re_D = 150$. In the following contexts, the details of this acoustic far-field will be presented, and the effects of some necessary conditions, such as the effect of Reynolds number, Mach number, length of cylinder, and observation distance, will be discussed. The numerical results will be compared with the experimental ones to analyze how to use the numeric approach developed in this work for practical usage.

5.3.1 Intensity of Far-field Noise

The intensity of sound pressure is defined as the energy transmitted per unit time and unit area or the power per unit area. Far from a source of sound, the intensity is simply the mean square sound pressure divided by the speed of sound and density of the medium:

$$I = \frac{\overline{p'}^2}{\rho_0 c_0} \quad (5.1)$$

Usually the root mean square sound pressure is calculated in CAA as a measurement of the far-field sound intensity:

$$p'_{rms}(\vec{x}) = \sqrt{\lim_{T \rightarrow \infty} \left(\frac{1}{T} \int_0^T p'^2(\vec{x}, t) dt \right)} \quad (5.2)$$

Since the sound pressure wave generated by the laminar flow around a circular cylinder at $Re_D = 150$ investigated in the previous chapter is harmonic, the integration time, T , is not required to be as large as $T \rightarrow \infty$, if it can be taken as a round number of the period. But the sound pressure wave generated by the turbulent flow around a circular cylinder at $Re_D = 3900$ discussed in this chapter is quasi-periodic but not harmonic, the integration time, T , should be large enough in order to obtain a time-independent $p'_{rms}(\vec{x})$. The near-field source terms are calculated in a dimensionless integration time, T^* , of about 162 in this work, and from this dynamic near-field of $T^* \approx 162$, an acoustic far-field of $T^* \approx 100$ can be calculated. The dimensionless integration time, T^* , is defined as:

$$T^* = \frac{T U_\infty}{D} \quad (5.3)$$

where,

$$T = t_n - t_0 \quad (5.4)$$

U_∞ , D , t_0 and t_n denote the inflow velocity, diameter of the cylinder, beginning time and ending time of sampling respectively.

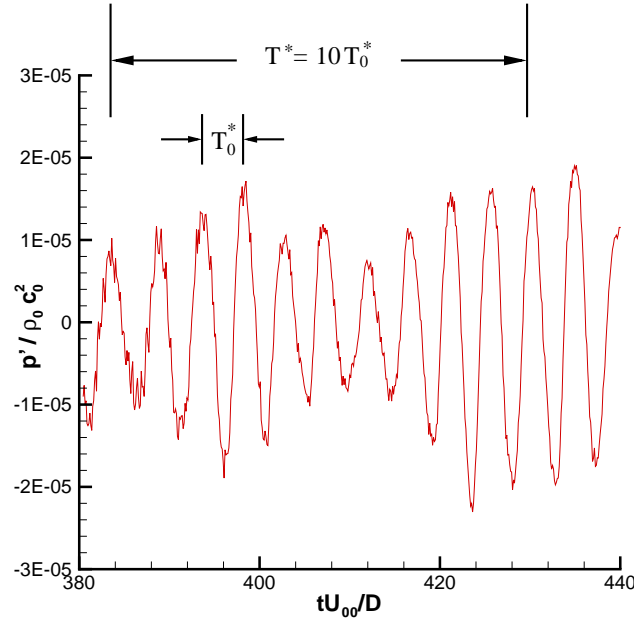


Figure 5.2: A Time-history of Sound Pressure, CS No.2, $\theta = 90^\circ$, $r_0/D = 75$

Results show that the integration time used is already large enough to obtain a relatively time-independent p'_{rms} in this work, but the value of p'_{rms} still fluctuated in a range of $\pm 5\%$ while the sampling times were changed. The following table shows a relationship between the root mean square sound pressure and averaging time intervals with an arbitrary beginning time, t_0 , of sampling:

	$p'_{rms}/\rho_0 c_0^2$, $r_0/D = 250$	
T^*/T_0^*	LES/GUO	LES/FARASSAT, ($L_c/D = 241.9$)
10	7.46341×10^{-6}	6.89153×10^{-6}
15	7.32852×10^{-6}	6.74514×10^{-6}
20	7.49169×10^{-6}	6.92012×10^{-6}

In the above table, T_0^* denotes the dimensionless quasi-period of the sound pressure,

$$T_0^* = \frac{U_\infty}{f_0 D} \quad (5.5)$$

where f_0 is the first harmonic frequency of the dominant lift fluctuation, which makes the sound pressure fluctuation quasi-periodic. Therefore, T^*/T_0^* represents the number of quasi-periods within an averaging interval. An example of the time-history of the sound pressure, $p'(t)$, is shown in figure 5.2, in which the definitions of T^* and T_0^* are also shown.

If a totally time-independent p'_{rms} is required, the dimensionless integration time, T^* , has to be at least 300, according to some published research (see FRANKE(2002) [29]). That

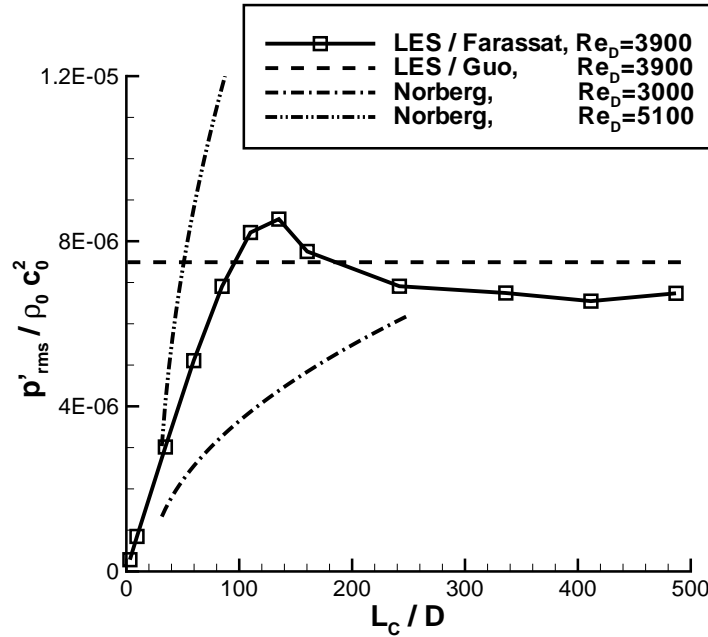


Figure 5.3: Root Mean Sound Pressure vs Copy Length, CS No.2, $\theta = 90^\circ$, $r_0/D = 250$

implies a T^*/T_0^* of about 60. In the results discussed in the following context, T^*/T_0^* will be chosen as 20 to obtain the root mean square sound pressure, p'_{rms} .

Figures 5.3 and 5.4 show the simulated values of p'_{rms} which is measured in the middle plane of the span width. In figure 5.3, the numerical results of p'_{rms} are compared with the values predicted through the empirical formula of NORBERG [11]. There are good agreements between the numerical and experimental results in the range of $30 < L_c/D < 150$. Either the magnitude of p'_{rms} or the increasing rate of p'_{rms} versus L_c/D of the numerical results at $Re_D = 3900$ is between the corresponding values of the empirical results at $Re_D = 3000$ and $Re_D = 5100$. If $L_c/D < 30$, the p'_{rms} is strongly influenced by the end conditions of the cylinder. There is large scattering of the experimental results, and the boundary conditions used in the current numerical calculations are also not suitable. Therefore, no comparison between numerical and experimental results can be made for the condition of $L_c/D < 30$. If $L_c/D > 150$, the numerical p'_{rms} increases no more with an increment of L_c/D . It is mathematically and physically reasonable that the p'_{rms} has no more increment if the length of cylinder increases to more than a critical length, which makes the ends of the cylinder far away from the middle plane of the span width and very small compared to the whole cylinder length, so as to have relatively little influence on the p'_{rms} measured in the middle plane. This critical length is shown by the numerical simulation, but not by the empirical formula which was derived from the experimental data of KEEFE [41], LEEHEY et al. [42] and IIDA et al. [37]. The lengths of the cylinder used in these three experiments are relatively small.

The empirical formula of p'_{rms} used in figure 5.3 is concluded in NORBERG's comprehensive review [11] of the experimental results of a stationary cylinder in cross-flow. This empirical formula is constituted as follows:

$$\frac{p'_{rms}}{\rho_0 c_0^2} = \frac{1}{2\sqrt{2}} C_{s'} M^3 \frac{\sqrt{l^* - \sigma^*}}{r^*} \quad (5.6)$$

$$C_{s'} = C_{L'} S \sqrt{\Lambda^*} \quad (5.7)$$

$$\Lambda^* = \frac{1}{D} \int_0^\infty R_{LL}(s) ds \quad (5.8)$$

$$\sigma^* = \frac{1}{\Lambda^* D} \int_0^\infty s R_{LL}(s) ds \quad (5.9)$$

where D is the diameter of the cylinder and the other dimensionless lengths are scaled by D . $C_{L'}$ is the coefficient of root mean square lift fluctuation defined as:

$$C_{L'} = \frac{L'}{D l \rho_0 U_\infty^2 / 2} \quad (5.10)$$

Λ^* and σ^* denote the dimensionless length and centroid of span width direction correlation of lift coefficient respectively. Based on a systematic review of many experimental results to date, NORBERG concluded the following empirical formulas for predictions of Λ^* and σ^* :

$$\Lambda^* = (1 - \alpha) \Lambda_1^* + \alpha \Lambda_2^* \quad (5.11)$$

$$\sigma^* = \frac{(1 - \alpha) \Lambda_1^{*2} + \alpha \Lambda_2^* \sigma_2^*}{\Lambda^*} \quad (5.12)$$

$$\sigma_2^* = \left(\frac{n}{\pi} \sin \frac{n}{\pi} \right) \frac{\sin(\pi/n)}{\sin(2\pi/n)} \Lambda_2^* \quad (5.13)$$

According to the reviewed experimental results, the coefficients in the above formulae have the following values for $Re_D = 3000$ and $Re_D = 5100$:

	Λ_1^*	Λ_2^*	n	α
$Re_D = 3000$	3	27	3.0	0.61
$Re_D = 5100$	3	22	2.4	0.49

$C_{L'}$ is calculated with the following empirical formula for $1600 < Re_D < 5400$:

$$C_{L'} = 0.045 + 3.0 \left(\log \left(\frac{Re_D}{1600} \right) \right)^{4.6} \quad (5.14)$$

And then the coefficients in formula 5.6 are obtained as:

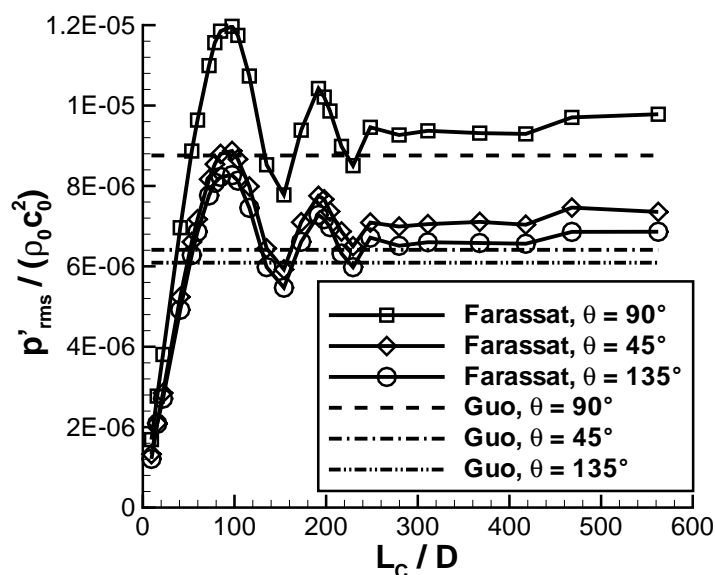


Figure 5.4: Root Mean Sound Pressure vs Copy Length, CS No.2, $\theta = 90^\circ$, $r_0/D = 125$

	C_L	Λ^*	σ^*
$Re_D = 3000$	0.05265	10.61	20.91
$Re_D = 5100$	0.1727	14.58	27.59

In figure 5.4, the relationship between p'_{rms} and numerical copy length in the span direction, L_c/D , in three different observation directions are shown. The p'_{rms} simulated with the 3D formulation of FARASSAT is convergent to that simulated with the 2D formulation of GUO, if L_c/D is more than 250. It means that the efficient 2D FW-H approach can be directly used for the prediction of p'_{rms} generated by flow around a long cylinder with $L_c/D > 250$. But the acoustic simulation with 2D FW-H approach over-predicts the p'_{rms} for the cases of $L_c/D < 80$. If L_c/D is between 80 and 250, the 2D approach may over- or under-predicts the p'_{rms} somewhat.

If $11\pi < L_c/D < 77\pi$, the sound pressure coefficient, $C_{s'}$, defined in equation 5.6 of page 87, is in the range of 0.05 to 0.07 based on the simulated acoustic pressure. That is in good agreement with the experimental results reviewed by NORBERG [11]. The comparisons between the numerically simulated and experimentally measured sound pressure coefficient, $C_{s'}$, are shown in figure 5.5 of page 89.

The distance effect is similar to the situation at $Re_D = 150$, namely $p'_{rms} \sim 1/r^{1/2}$ for the 2D cases; and $p'_{rms} \sim 1/r$ for the 3D cases (see figure 5.6 of page 89). The 2D cases include: the numerical results based on both the formulation of GUO and the formulation

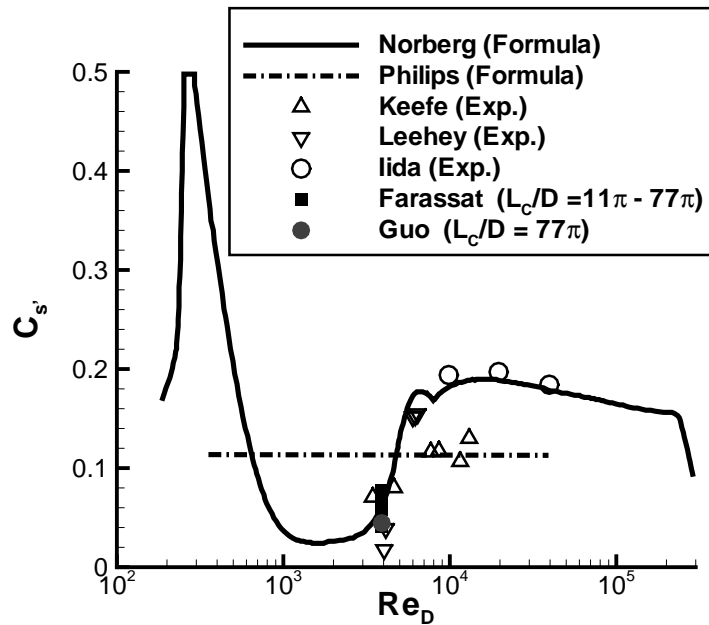


Figure 5.5: Comparisons of $C_{s'}$ between Numerical Simulations and Experimental Measurements, CS No.2, $Re_D = 3900$

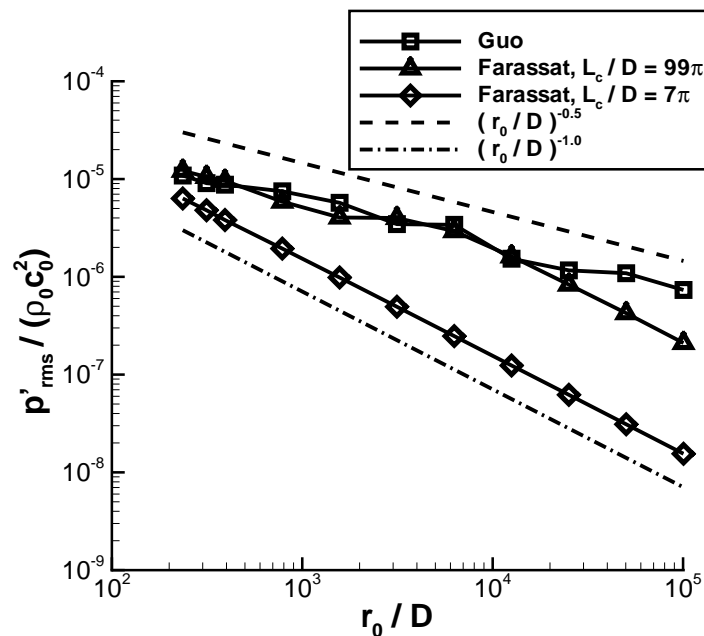


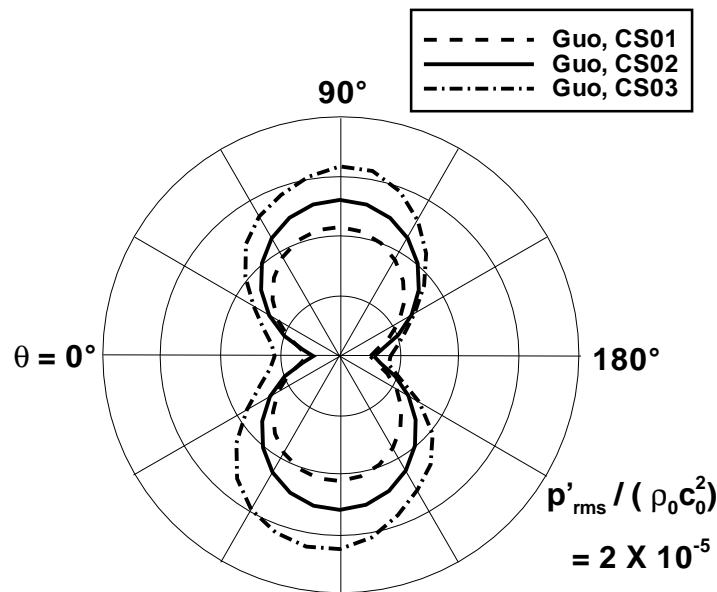
Figure 5.6: Simulated Distance Effect of Sound Pressure, CS No.2, $Re_D = 3900$

of FARASSAT with a sufficient copy length. The 3D cases are the numerical results based on the formulation of FARASSAT with an insufficient copy length. Whether a copy length is sufficient to generate a 2D wave spreading, is not only dependent on the wavelength of the sound pressure, but also dependent on the observation position. More distant is the observation position from the cylinder, more copy length is required to obtain a convergent 2D wave spreading at the observation position.

5.3.2 Directivity of Far-field Noise

In figure 5.8(a) of page 93, the simulated directivities of the acoustic far-field are shown with different copy lengths of the 3D FW-H approach. The forms of the directivity patterns are similar for different copy lengths, but the magnitudes of p'_{rms} change with the copy lengths according to the relationship shown in figure 5.4 of page 88. The forms of the directivity patterns show still a lift-dominant dipolar acoustic far-field, but more influences of drag fluctuations can be seen in the flow direction, namely the horizontal direction in figure 5.8(a) of page 93. In this direction, the magnitude of p'_{rms} is no more as small as the directivity at $Re_D = 150$, because the drag fluctuation at $Re_D = 3900$ is more than that at $Re_D = 150$ due to irregular vortex shedding and turbulent fluctuation behind the cylinder.

In figure 5.7 of page 91, the directivities of the acoustic far-field are presented with different control surfaces. The forms of the directivity patterns are similar for the first and second control surfaces, and the magnitude of p'_{rms} calculated from the second control surface is 10% more than that from the first control surface. The form of the directivity pattern for the third control surface is no longer symmetric and the magnitude of p'_{rms} on this control surface is 5% more than that on the second control surface. There are three main reasons why the magnitude of p'_{rms} calculated from the outer control surface is somewhat more than that from the inner control surface: (1) The outer control surface encloses more quadrupolar volume sources; (2) The outer control surface is under more influences of the numerical outer boundary conditions and less influences of the non-slip inner boundary condition; (3) The spatial resolution on the outer control surface is coarser than that on the inner control surface, especially on the four corners of the control surface. There are still two control surfaces out of the third one. But the directivity patterns based on these two control surfaces are no longer dipolar shapes. The dipolar form of directivity is in agreement with the experimental result, and the non-dipolar form is influenced by the numeric errors, such as the boundary reflection and coarser spatial resolution far away from the cylinder. According to the criterion of the directivity pattern, the acoustic far-field calculated from the second control surface is regarded as the best one for the physical simulation in this work.

Figure 5.7: Directivity vs Control Surface, GUO, $r_0/D = 75$

5.3.3 Frequency Spectrum of Far-field Noise

In figures 5.8(b) and 5.8(c) of page 93, the frequency spectra of sound pressure calculated based on the 3D formulation of FARASSAT with different copy lengths are compared with those based on 2D formulation of GUO. Figure 5.8(b) is for the observation position at $r_0/D = 125$ and $\theta = 90^\circ$, and 5.8(c) for the observation position at $r_0/D = 125$ and $\theta = 0^\circ$. Results show that: (1) If the copy length is sufficient, the spectrum values are similar for the results based on both the 3D and 2D formulations, namely the 3D results are convergent to the 2D results; (2) If the copy length is still less than the critical length, the differences between the spectrum densities of different copy lengths are mainly in the low frequency range. The broad band sound pressure in the high frequency range is little influenced by the copy length. With an insufficient copy length, the 3D aeroacoustic solver may under-predict the far-field sound pressures in the low frequency range, just as the case of $L_C/D = 7\pi$, as well as may over-predict them, just as the case of $L_C/D = 25\pi$ in figures 5.8(b) and 5.8(c); (3) In the high frequency range, all the spectrum densities obey the exponential $-\frac{5}{3}$ rule which is a general feature of the turbulent fluctuation; (4) The spectrum peak value at $f/f_0 = 1.0$ for the observation position at $\theta = 90^\circ$ is under a strong influence of the copy length.

The spectrum peak value of the sound pressure measured at $\theta = 90^\circ$ can be compared with the experimental results of SZEPESSY [74] through the following similarity law:

$$C_{sf} = \frac{[p' / (\rho_0 c_0^2)]^* r^*}{M^3 \sqrt{l^* - \sigma^*}} = Const. \tag{5.15}$$

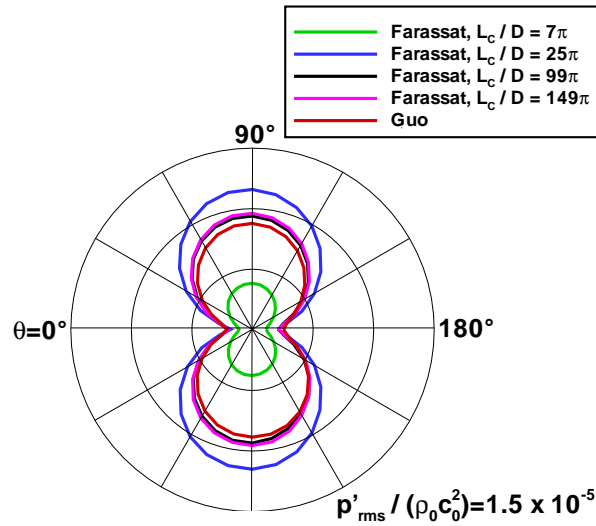
$$[p' / (\rho_0 c_0^2)]^* = \left| \int_{-\infty}^{+\infty} \frac{p'}{\rho_0 c_0^2} e^{-2\pi f t} dt \right| \tag{5.16}$$

where $[p' / (\rho_0 c_0^2)]^*$ is the dimensionless spectrum density of sound pressure, and r^* , l^* and σ^* are dimensionless values scaled with the cylinder radius, D (see equation 5.6). The calculated C_{sf} values are compared in table 5.2. The agreement between the numerical and experimental results is good for an aeroacoustic comparison. If l^* of the numerical simulation is set to 9π , similar as the experimental parameter of SZEPESSY, the calculated C_{sf} is about 50% over-predicted because the copy length is less than the critical length. It is very difficult to carry out such kinds of comparison, if the cylinder length is not long enough. There will be a large scattering due to the end effect of the cylinder both in the experimental and numerical treatments. Through the comprehensive comparisons with respect to overall sound level, directivity and frequency spectrum, it can be concluded that the 2D formulation of the FW-H approach can be used to carry out an efficient aeroacoustic simulation as a preparation of the more computationally expensive 3D approach. The total features of the acoustic far-field calculated with the 2D formulation is comparable with those calculated with the 3D formulation.

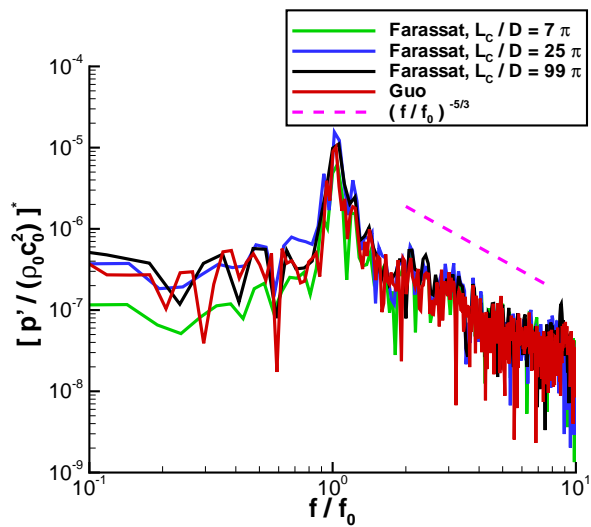
	M	r^*	l^*	σ^*	$[p' / (\rho_0 c_0^2)]^*$	C_{sf}
SZEPESSY	0.022	125	28.75	24.0	1.914×10^{-9}	1.03×10^{-2}
Present (GUO)	0.2	125	assume 99π	24.0	9.901×10^{-6}	9.13×10^{-3}
Present (FARASSAT)	0.2	125	99π	24.0	1.029×10^{-5}	9.49×10^{-3}
Present (FARASSAT)	0.2	125	9π	24.0	2.073×10^{-6}	1.57×10^{-2}

Table 5.2: Comparisons of Spectrum Peak Values ($Re_D = 3900$)

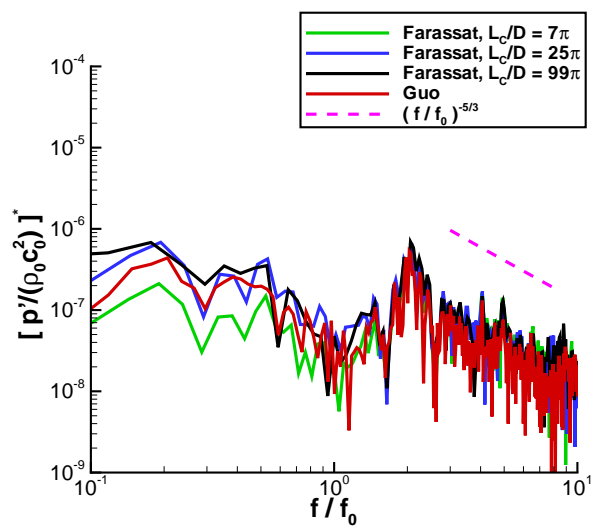
In figure 5.9 and 5.10 of page 94, the frequency spectra at the different observation directions are shown. Along the flow direction, namely $\theta = 0^\circ$ and $= 180^\circ$, the drag dipole dominates the acoustic field with its characteristic frequency of $f/f_0 = 2.0$; In the vertical direction to the flow, namely $\theta = 90^\circ$, the lift dipole dominates the acoustic field with its characteristic frequency of $f/f_0 = 1.0$. Between the parallel and vertical directions to the flow, e.g. $\theta = 30^\circ$ or $\theta = 150^\circ$, two spectrum peaks can be seen, i.e. one peak of $f/f_0 = 1.0$, corresponding to the lift dipole, and another of $f/f_0 = 2.0$, corresponding to the drag dipole. The peak of $f/f_0 = 2.0$ is relative weak, so that it is swamped in the larger peak of $f/f_0 = 1.0$ at the observation position of $\theta = 60^\circ$ or $\theta = 120^\circ$.



(a) Directivity vs Copy Length (L_C)



(b) Frequency Spectrum vs L_C , at $\theta = 90^\circ$



(c) Frequency Spectrum vs L_C , at $\theta = 0^\circ$

Figure 5.8: The Simulated Acoustic Far-field of Flow around a Circular Cylinder at $Re_D = 3900$, CS No.2, $r_0/D = 125$. ($[p' / (\rho_0 c_0^2)]^* = \left| \int_{-\infty}^{+\infty} \frac{p'}{\rho_0 c_0^2} e^{-2\pi f t} dt \right|$)

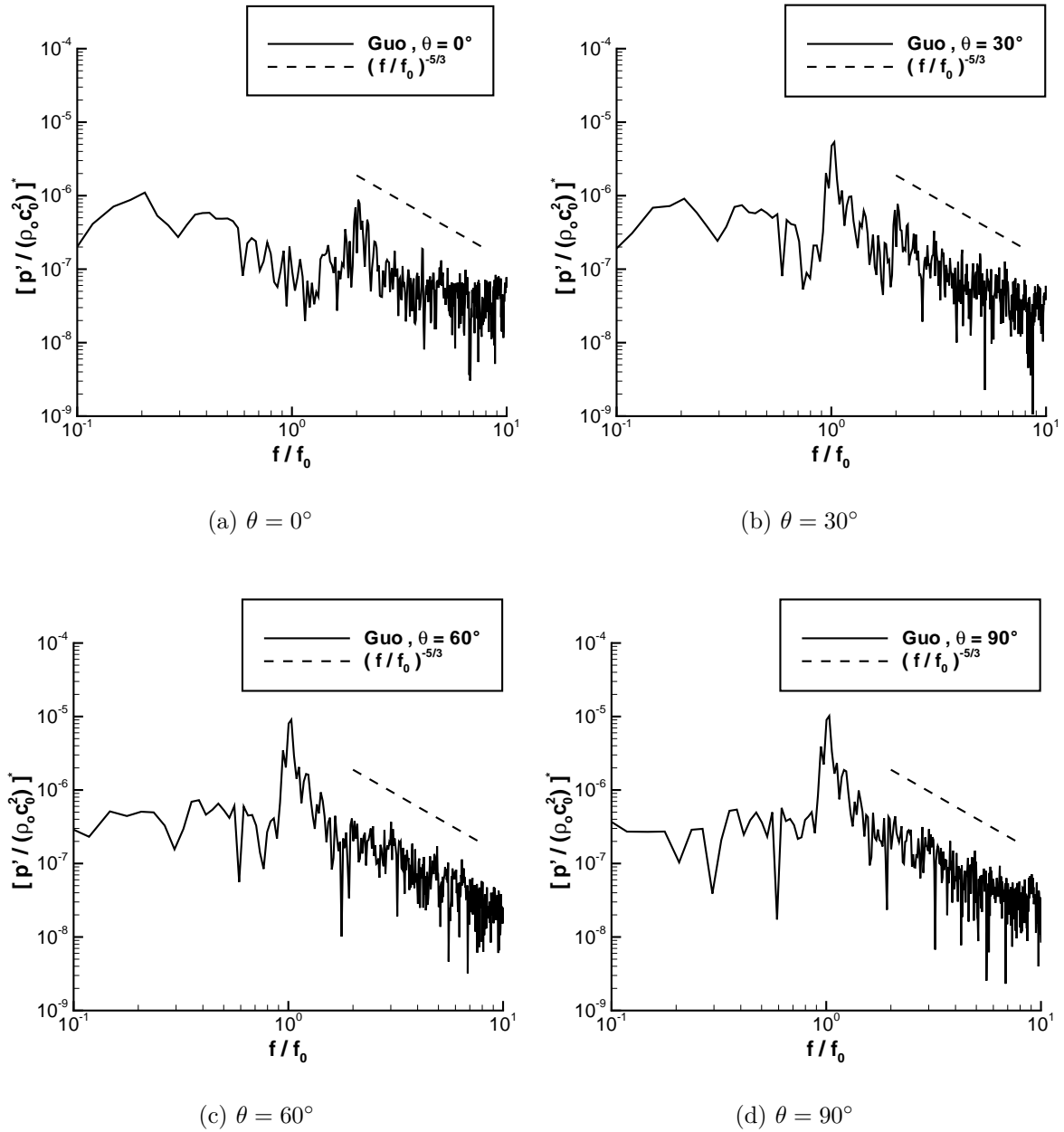


Figure 5.9: Frequency Spectrum of Sound Pressure at Different Observation Direction ($Re_D=3900$, GUO, CS02, $r_0/D=125$)

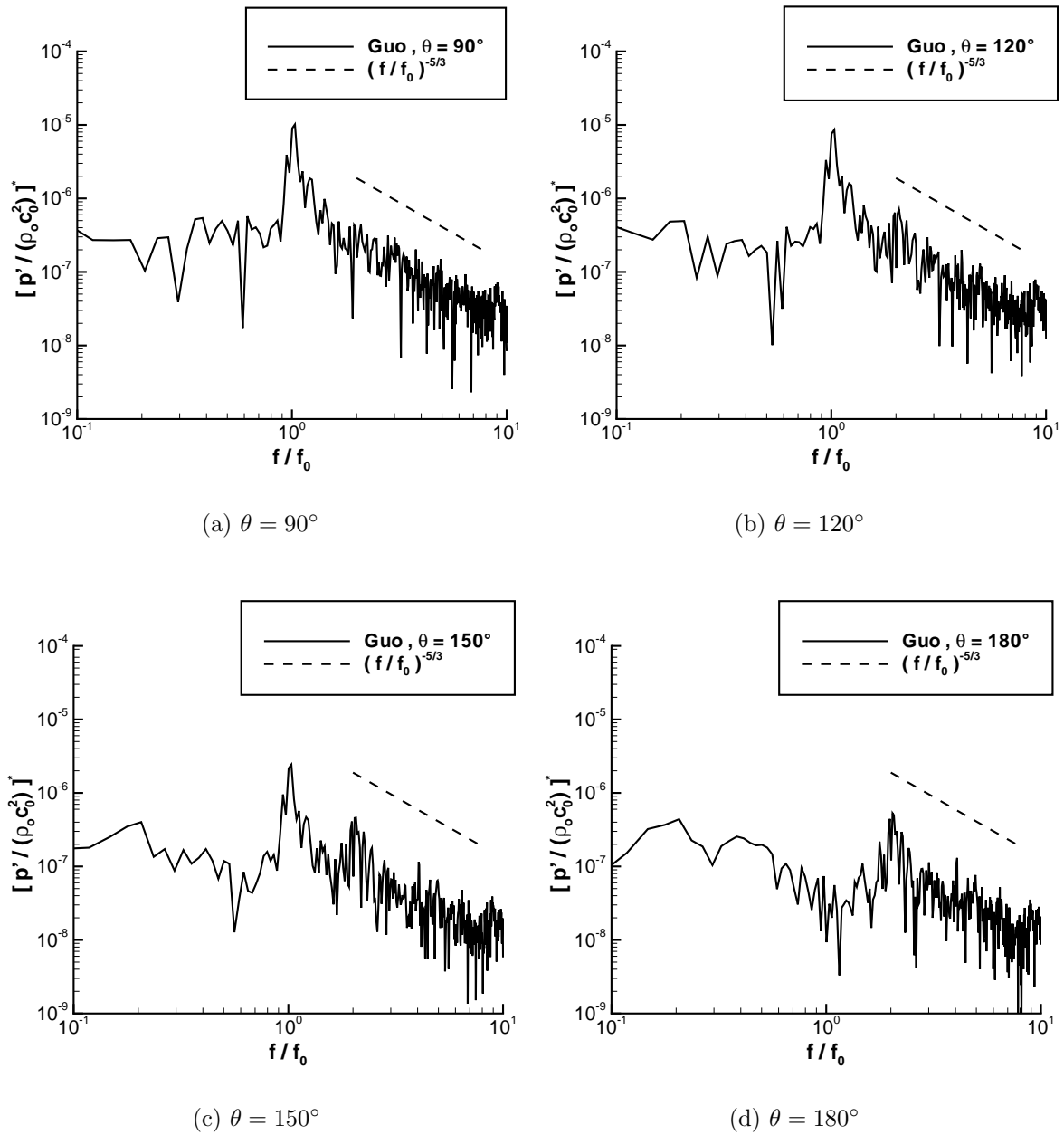


Figure 5.10: Frequency Spectra of Sound Pressure at Different Observation Directions ($Re_D=3900$, GUO, CS No. 2, $r_0/D=125$)

Chapter 6

Conclusions and Outlook

The capability of the computer program implemented with three different integral extension formulations of the (porous) FW-H approach is investigated, with comprehensive verification and validation examples. The computer program is verified with the analytical solution of an acoustic 3D mono-, di- or quadrupole, as well as an acoustic 2D mono- or dipole to confirm its ability for simulating acoustic propagation in a static unbounded medium. It is also verified with the analytical solution of an acoustic monopole in subsonic uniform flow to confirm its ability for simulating acoustic propagation in a uniformly moving medium. The analytical solution of the so-called dancing line-vortices is used to verify the ability of the code for simulating sound generation by an unsteady flow with a control surface in the non-linear flow region.

Except for the case of the acoustic 2D monopole in a subsonic flow, the numerical solutions calculated by all three formulations, namely the formulations of FARASSAT [20], GUO [32], and LOCARD [49], give good agreement with the analytical solutions at a high level of accuracy, namely with a very small relative error of 0.1% under the optimal computational parameters. In the case of the acoustic 2D monopole in the subsonic uniform flow, the numerical simulations based on the formulation of LOCARD can give a good agreement with the corresponding analytical solutions at a high accuracy under the optimal computational parameters. The numerical simulations based on the formulations of FARASSAT and GUO neglect convection effects due to the free-space GREEN's function used, and thus are only in good agreement with the analytical solution in the normal direction to the flow.

In the validation example, compared with the acoustic DNS of a stationary cylinder in cross-flow at $Re_D = 150$ and $Ma = 0.2$, the current numerical solutions based on the three inner control surfaces are in good agreements with the DNS, concerning whole features of the acoustic far-field, namely overall sound pressure, temporal history and spatial directivity; although, in the first step of the hybrid simulation, namely in the near-field CFD, no particular treatments for the acoustic computation are used, namely no particular boundary conditions, no particular high order discrete schemes, no very large computa-

tional domain, and so on. Although these three control surfaces of the computation are set in the highly non-linear region, the near-field pseudo-pressure fluctuations are effectively filtered out in the second step of the simulation, and all the physical features of the acoustic far-field are well simulated. The current simulation is much cheaper with respect to the computational costs than the acoustic DNS, but it gives also a similar prediction to the DNS.

The current numerical solutions based on the two outer control surfaces are not similar to the DNS. The directivity is present not with the dipolar feature, and the sound pressure is much over-predicted. It seems that the pseudo-sound pressure, namely the local pressure fluctuation in the near-field, were not filtered out by the aeroacoustic solver. This may be due to the following causes: (1)The computational domain is not large enough; (2)The outer boundary condition is not non-reflecting; (3)The spatial resolution in the outer region is not fine enough.

Through the verification and validation examples, the computational parameters, such as the position of the control surface, copy length in the span direction, spatial and temporal resolutions, and accuracies of numerical interpolation, derivation and integration, are investigated in detail for an optimal balance between accuracy and efficiency. It is necessary to chose these computational parameters carefully, because three-dimensional unsteady aeroacoustic computation presents a serious challenge to the computer capacity of calculation speed and storage space. It is suggested that:

The control surface is required to be large enough to enclose all the main dynamical sources, but as small as possible; and far enough to the outer boundary, if it is not a non-reflecting one. The geometrical form of the control surface is preferred to be round and smooth.

If an open cylindrical control surface is used, this control surface should be long enough in the span direction to obtain a convergent surface integration for a convergent acoustic far-field simulated. This critical copy length is about 10 times the wavelength of the sound pressure generated, $(L_C/\lambda)_{crit} \sim 10$, when $D/\lambda < 3\%$ and $r_0/\lambda < 50$ (where L_C is the length of the cylindrical control surface after copying, D is the radius of the control surface, r_0 is the distance of the observation position to the center point of the cylinder, and λ is the wavelength of the sound pressure generated). If the length of the cylindrical control surface is less than the critical copy length, no open control surface is valid for an accurate aeroacoustic simulation.

The simulated acoustic far-field is usually not so sensitive to the linear resolution of the control surface, because the sound wavelength is usually much more than the scale of flow structure and $\Delta l/\lambda$ (Δl denotes the linear resolution of the control surface, and λ denotes the sound wavelength) is very likely to be under 0.2. If $\Delta l/\lambda$ is under 0.2, the relative numerical error due to spatial resolution can already be

under 5%; for a $\Delta l/\lambda$ of under 0.02, that error is even under 0.5%. But the angular resolution should be paid more attention to, to ensure that it is not more than 6° , namely not less than about 60 panels per circle or 1800 panels per sphere. If the two criteria of $\Delta l/\lambda < 0.02$ and $\Delta\theta < 6^\circ$ are fulfilled, the relative numerical error due to the spatial resolution for the integral extension from the near-field CFD data to the acoustic far-field can be under 0.5%;

Two major factors, namely the requirements of the temporal numerical approximations (the interpolation of the retarded-time and the temporal derivation of source terms) and the cut-off frequency for the spectral analysis, decide the requirement of temporal resolution. If $\Delta t/T$ is smaller than 0.02 for the 2nd order temporal interpolation and derivation, namely one pseudo-period 50 points, or $\Delta t/T$ is smaller than 0.07 for the 4th order corresponding numerical approximation, the relative error due to the temporal numerical approximation can be under 0.5% in the corresponding aeroacoustic simulation. The cut-off frequency, f_{off} , can be calculated with $f_{off} = 1/(2\Delta t)$;

It is suggested to use the 2nd order midpoint quadrature, because the more accurate but computationally more expensive 4th order SIMPSON's quadrature brings very limited benefits, if the spatial resolution is not too coarse. The 4th order SIMPSON's quadrature is only about 2nd order accuracy for the vector surface integration required in the current work. But it is suggested to adopt the 4th order numerical temporal interpolation and derivation schemes when $\Delta t/T$ is more than 0.02. If $\Delta t/T$ is less than 0.02, the 2nd order numerical approximation can already give a good result.

If the above optimal parameters are not reached, the error estimation can be given with the relationships between the parameters and numerical errors shown in this work.

An efficient way to estimate the acoustic far-field generated by a flow around a solid structure is successfully tested, namely using the 2D Fourier transformed approaches of the (porous) FW-H method instead of 3D approaches, and using LES instead of DNS. The 2D Fourier transformed approaches use the CFD data averaged in the span direction as an input. The calculation cases of the circular cylinder in the cross-flow at $Re_D = 150$ or 3900 ($Ma = 0.2$), show that the whole features of the acoustic far-field, namely total sound pressure, directivity and frequency spectrum, can be well simulated by this efficient way. The simulated directivity and spectral distribution patterns are similar, when using either the 2D or the 3D FW-H approaches. The absolute magnitudes of the overall sound level and the spectral density can be relatively revised by using the relationship between the copy length and the sound pressure level shown in the current work. The current simulated acoustic far-field from a laminar flow around a cylinder gives a good agreement with the aeroacoustic DNS of INOUE [38]. That from a turbulent flow around a cylinder, calculated by means of the LES of dynamic near-field with a periodic condition in

the span direction and the integral extensions to acoustic far-field, gives a good agreement with the experimental data of NORBERG [11] and SZEPESSY [74], although the acoustic effect of the SGS stress was neglected in the calculation. The source information on the control surface of the 3D formulation of the acoustic integral extension is calculated through copying in the span direction; and that of the 2D formulation is calculated through averaging in the span direction.

The possible improvements for the numerical simulation based on the hybrid CFD / (porous) FW-H approach are considered. It may be very helpful to enlarge the computational domain and to adopt non-reflecting boundary conditions. For high REYNOLDS number flow, the SGS stress effect may play a role in the acoustic far-field, which should be also calculated. Through a correlation analysis between the simulated acoustic far-field and the dynamic near-field, the aeroacoustic sources can be somewhat located.

Bibliography

- [1] J. Alken. Experimentelle und numerische Untersuchungen zur Umstroemung einer komplexen Geometrie. *PhD Thesis, Universitaet Siegen*, 2003.
- [2] H. M. Atassi, M. Dusey, and C. M. Davis. Acoustic Radiation from a Thin Airfoil in Nonuniform Subsonic Flows. *AIAA Journal*, 31(1):12 – 19, January 1993.
- [3] H. M. Atassi, S. Subramaniam, and J. R. Scott. Acoustic Radiation from Lifting Airfoils in Compressible Subsonic Flow. *AIAA Paper*, 90-3911, 1990.
- [4] C. Bailly, P. Lafon, and S. Candel. A Stochastic Approach to Compute Noise Generation and Radiation of Free Turbulence. *AIAA Paper*, 95-092, 1995.
- [5] T. F. Balsa. The Acoustic Field of Sources in Shear Flow with Application to Jet Noise: Convective Amplification. *J. Fluid Mech.*, 79(1):33 – 47, 1977.
- [6] W. Bechara, C. Bailly, and P. Lafon. Stochastic Approach to Noise Modelling for Free Turbulence Flows. *AIAA Journal*, 32(3):455 – 463, 1994.
- [7] C. H. Berman and J. I. Ramos. Simultaneous Computation of Jet Turbulence and Noise. *AIAA Paper*, 89-1091, 1989.
- [8] K. S. Brentner. An Efficient and Robust Method for Predicting Helicopter High-Speed Impulsive Noise. *Journal of Sound and Vibration*, 203(1):87 – 100, 1997.
- [9] K. S. Brentner and F. Farassat. Helicopter Noise Prediction: The Current Status and Future Direction. *Journal of Sound and Vibration*, 170(1):79 – 96, 1994.
- [10] K. S. Brentner and F. Farassat. Analytical Comparison of the Acoustic Analogy and Kirchhoff Formulation for Moving Surfaces. *AIAA Journal*, 36(8):1379 – 1386, 1998.
- [11] C. Norberg. Fluctuating Lift on a Circular Cylinder: Review and New Measurements. *Journal of Fluids and Structures*, 17:57 – 96, 2003.
- [12] T. Colonius, S. K. Lele, and P. Moin. Sound Generation in a Mixing Layer. *J. Fluid Mech.*, 330:375 – 409, 1997.

- [13] D. Crighton. Computational Aeroacoustics for Low Mach Number Flows. *Computational Aeroacoustics (Editors: J. Hardin and M. Hussaini)*, Springer:50 – 68, 1993.
- [14] N. Curle. The Influence of Solid Boundaries upon Aerodynamic Sound. *Proc. Roy. Soc. A*, 231:505 – 513, 1955.
- [15] K. Debatin. Lokalisation aeroakustischer Quellen in scherschichtdominanten Strömungen. *PhD Thesis, University of Karlsruhe(TH)*, 1999.
- [16] P. di Francescantonio. A New Boundary Integral Formulation for the Prediction of Sound Radiation. *Journal of Sound and Vibration*, 202(4):491 – 509, 1997.
- [17] A. P. Dowling and J. E. Ffowcs-Williams. Sound and Sources of Sound. *Westgate Hoewood Publishing*, pages 207 – 208, 1983.
- [18] R. Ewert. A Hybrid Computational Aeroacoustics Method to Simulate Airframe Noise. *PhD Thesis, RWTH Aachen*, 2003.
- [19] F. Farassat. Discontinuities in Aerodynamics and Aeroacoustics: The Concept and Applications of Generalized Derivatives. *Journal of Sound and Vibration*, 55(2):165 – 193, 1977.
- [20] F. Farassat. Linear Acoustic Formulae for Calculation of Rotating Blade Noise. *AIAA Journal*, 19(9):1122 – 1130, 1981.
- [21] F. Farassat. Prediction of Advanced Propeller Noise in the Time Domain. *AIAA Journal*, 24(4):578 – 584, 1984.
- [22] F. Farassat and K. S. Brentner. The Uses and Abuses of the Acoustic Analogy in Helicopter Rotor Noise Prediction. *Journal of American Helicopter Society*, 33:29 – 36, 1988.
- [23] F. Farassat and K. S. Brentner. Supersonic Quadrupole Noise Theory for High-Speed Helicopter Rotors. *Journal of Sound and Vibration*, 3:481 – 500, 1998.
- [24] F. Farassat and K. S. Brentner. The Acoustic Analogy and the Prediction of the Noise of Rotating Blades. *Theoretical and Computational Fluid Dynamics*, 10:155 – 170, 1998.
- [25] F. Farassat and M. Farris. Verification and Analysis of Formulation 4 Of Langley for the Study of Noise from High Speed Surfaces. *AIAA Paper*, 99-1881, 1999.
- [26] F. Farassat and M. K. Myers. Extension of Kirchhoffs Formula to Radiation from Moving Surfaces. *Journal of Sound and Vibration*, 123(3):451 – 460, 1988.

- [27] F. Farassat and G. P. Succi. The Prediction of Helicopter Rotor Discrete Frequency Noise. *Vertica*, 7(4):309 – 320, 1983.
- [28] J. Franke. Untersuchungen zur Grobstruktursimulation kompressibler Stroemungen mit der Volumenfiltermethode auf Bewegten Gittern. *PhD Thesis, Universitaet Karlsruhe (TH)*, 1998.
- [29] J. Franke and W. Frank. Large Eddy Simulation of the Flow past a Circular Cylinder at $Re=3900$. *Journal of Wind Engineering*, 90:1191 – 1206, 2002.
- [30] C. Fureby and G. Tabor. Mathematical and Physical Constraints on Large-eddy Simulations. *Theoret. Comput. Fluid Dynamics*, 9(2):85 – 102, 1997.
- [31] X. Gloerfelt, C. Bailly, and D. Juve. Direct Computation of the Noise Radiated by a Subsonic Cavity Flow and Application of Integral Methods. *Journal of Sound and Vibration*, 266:116 – 146, 2003.
- [32] Y. P. Guo. Application of the Ffowcs Williams/Hawkings Equation to Two-Dimensional Problems. *J. Fluid Mech.*, 403:201 – 221, 2000.
- [33] M. S. Howe. Contributions to the Theory of Aerodynamic Sound, with Application to Excess Jet Noise and the Theory of the Flute. *J. Fluid Mech.*, 71(4):625 – 673, 1975.
- [34] M. S. Howe. The Generation of Sound by Aerodynamic Sources in an Inhomogeneous Steady Flow. *J. Fluid Mech.*, 67(3):567 – 610, 1975.
- [35] S. Ianniello. Algorithm to Integrate the Ffowcs Williams-Hawkings Equation on Supersonic Rotating Domain. *AIAA Journal*, 37(9):1040 – 1047, 1999.
- [36] S. Ianniello. Quadrupole Noise Predictions Through the Ffowcs Williams-Hawkings Equation. *AIAA Journal*, 37(9):1048 – 1054, September 1999.
- [37] A. Iida and T. Otaguro. Prediction of Aerodynamic Sound Spectra from a Circular Cylinder. *Proceedings of the 5th Triennial International Symposium on Fluid Control, Measurement and Visualization, Hayama, Japan*, pages 126 – 131, 1997.
- [38] O. Inoue and N. Hatakeyama. Sound Generation by a Two-Dimensional Circular Cylinder in a Uniform Flow. *J. Fluid Mech.*, 471:285 – 314, 2002.
- [39] A. Jameson, W. Schmidt, and E. Turkel. Numerical Solution of the Euler Equations by Finite volume Methods Using Runge-Kutta Time-stepping Schemes. *AIAA Paper*, 81-1259, 1981.
- [40] G. Kalizin, N. Kalizin, and A. Wilde. A Factorization Scheme for RANS Turbulence Models and SNGR Predictions of Trailing Edge Noise. *AIAA Paper*, 2000-1982, 2000.

- [41] R. T. Keefe. An Investigation of the Fluctuating Forces Acting on a Stationary Circular Cylinder in a Subsonic Stream and of the Associated Sound Field. *The Journal of the Acoustical Society of America*, 34:171 – 1714, 1962.
- [42] P. Leehey and C. Hanson. Aelian Tones Associated with Resonated Vibration. *Journal of Sound and Vibration*, 13:465 –483, 1971.
- [43] S. Lele. Compact Finite Difference Schemes with Spectral-like Resolution. *J. Comput. Phys.*, 103:16 – 42, 1992.
- [44] S. Lele. Computational Aeroacoustics, a Review. *AIAA Paper*, 97-0018, 1997.
- [45] M. Lesieur and P. Comte. Favre Filtering and Macro-Temperature in Large-Eddy Simulations of Compressible Turbulence. *C. R. Acad. Sci. Paris, serie II B*, 329:363 – 368, 2001.
- [46] M. J. Lighthill. On Sound Generated Aerodynamically, I. General Theory. *Philosophical Transactions of the Royal Society, Series A*, 211:587 –654, 1952.
- [47] M. J. Lighthill. On Sound Generated Aerodynamically, II. Turbulence as a Source of Sound. *Philosophical Transactions of the Royal Society, Series A*, 222:1 – 32, 1954.
- [48] G. Lilley. On the Noise from Jets. *In AGARD CP-131*, Pages:13.1 –13.12, 1974.
- [49] D. P. Locard. An Efficient, Two-dimensional Implementation of the FFOWCS WILLIAMS and HAWKINGS Equation. *Journal of Sound and Vibration*, 229(4):897 –911, 2000.
- [50] A. Lyrantzis. Integral Methods in Computational Aeroacoustics - From the (CFD) Near-Field to the (Acoustic) Far-Field. *6th CEAS - ASC Workshop "From CFD to CAA" Athens Greece*, November 2002.
- [51] A. S. Lyrantzis. Review: The Use of Kirchhoff's Method in Computational Aeroacoustics. *Journal of Fluids Engineering*, 116:665 – 676, 1994.
- [52] X. Ma and G. Karamanos. Dynamics and Low-dimensionality of a Turbulent Wake. *J. Fluid Mech.*, 410:29 – 65, 2000.
- [53] F. Magagnato. KAPPA - Karlsruhe Parallel Program for Aerodynamics. *TASK Quarterly - Scientific Bulletin of Academic Computer Centre in Gdansk*, 2(2):215 – 270, 1998.
- [54] E. Manoha, G. Elias, B. Troff, and P. Sagaut. Towards the Use of Boundary Element Method in Computational Aeroacoustics. *AIAA Paper*, 99-1980, 1999.
- [55] E. Manoha, B. Troff, and P. sagaut. Trailing Edge Noise Prediction Using Large Eddy Simulation and Acoustic Analogy. *AIAA Journal*, 38(4):575 – 583, 2000.

- [56] L. Martinelli. Calculations of Viscous Flows with a Multigrid Method. *PhD Thesis, Princeton University*, 1987.
- [57] W. Möhring. On Vortex Sound at Low Mach Number. *J. Fluid Mech.*, 85(4):685 – 691, 1978.
- [58] I. Pantle. Stroemungsakustik auf der Basis akustischer Analogie mit LES und URANS. *PhD Thesis, University of Karlsruhe(TH)*, 2002.
- [59] I. Pantle, F. Magagnato, and M. Gabi. Geräuschverhalten von Strömungsmaschinen: Verfahrensentwicklung auf CFD-Basis. *VDI Berichte*, 1591, 2001.
- [60] I. Pantle, F. Magagnato, and M. Gabi. Numerical Aeroacoustics Using a Combined CFD-/Ffowcs-Williams Hawkins Method. *The 9th International Symposium on Transport Phenomena and Dynamics of Rotating Machinery, Honolulu, Hawaii, February 2002*.
- [61] O. M. Philips. On the Generation of Sound by Supersonic Turbulent Shear Layers. *J. Fluid Mech.*, 9:1 – 28, 1960.
- [62] A. R. Pilon and A. S. Lyrntzis. Integral Methods for Computational Aeroacoustics. *AIAA Paper*, 97-0020, 1997.
- [63] T. Pointsot and S. Lele. Boundary Conditions for Direct Simulation of Compressible Viscous Flows. *J. Comput. Phys.*, 101:104 – 129, 1992.
- [64] O. Posdziech and R. Grundmann. Numerical Simulation of the Flow around an Infinitely Long Circular Cylinder in the Transition Regime. *Theoretical and Computational Fluid Dynamics*, 15:121 – 141, 2001.
- [65] A. Powell. Theory of Vortex Sound. *The Journal of the Acoustical Society of America*, 36(1):177 – 195, January 1964.
- [66] A. Powell. Why Do Vortices Generate Sound? *Journal of Vibration and Acoustics*, 117:252 – 260, June 1995.
- [67] P. J. Roache. Quantification of Uncertainty in Computational Fluid Dynamics. *Annu. Rev. Fluid Mech.*, 29:123 –160, 1997.
- [68] C. L. Rumsey, R. T. Biedron, F. Farassat, and P. L. Spence. Ducted-Fan Engine Acoustic Predictions Using a Navier-Stokes Code. *Journal of Sound and Vibration*, 213(4):643 – 664, 1998.
- [69] B. A. Singer, K. S. Brentner, D. P. Lockard, and G. M. Lilley. Simulation of Acoustic Scattering from a Trailing Edge. *AIAA Paper*, 99-0231, 1999.

- [70] B. A. Singer, D. P. Lockard, and K. S. Brentner. Computational Aeroacoustic Analysis of Slat Trailing-Edge Flow. *AIAA Journal*, 38(9):1558 – 1564, 2000.
- [71] J. Smagorinsky. General Circulation Experiments with the Primitive Equations (I) the Basic Experiment. *Monthly Weather Review*, 91(3):99 – 164, 1963.
- [72] E. T. Spyropoulos and B. S. Holmes. Computation of the Airframe Noise of a Wing-Flap Configuration. *AIAA Paper*, 99-1801, 1999.
- [73] S. Sarkar and M. Hussaini. Computation of the Acoustic Radiation from Bounded Homogeneous Flows. *Computational Aeroacoustics (Editors: J. Hardin and M. Hussaini)*, Springer:335 – 349, 1993.
- [74] S. Szepessy. ALESSIA - Validation Report. *Internal Communication*, 2002.
- [75] C. K. W. Tam. Computational Aeroacoustics: Issues and Methods. *AIAA Journal*, 33(10):1788 – 1796, 1995.
- [76] C. K. W. Tam. On the Failure of Acoustic Analogy Theory to Identify the Correct Noise Source. *AIAA Paper*, 2001-2117, 2001.
- [77] C. K. W. Tam. Further Consideration of the Limitations and Validity of the Analogy Theory. *AIAA Paper*, 2002-2425, 2002.
- [78] C. K. W. Tam. Computational Aeroacoustics: An Overview of Computational Challenges and Applications. *International Journal of Computational Fluid Dynamics*, 18(6):547 – 567, 2004.
- [79] F. Tremblay, M. Manhart, and R. Friedrich. DNS of Flow around a Circular Cylinder at a Subcritical Reynolds Number with Cartesian Grids. *Proceedings of the Eighth European Turbulence Conference, Barcelona, Spain*, pages 659 – 662, June 2002.
- [80] S. Wagner, R. Bareiss, and G. Guidati. Wind Turbine Noise. *Springer*, 1996.
- [81] M. Wang and P. Moin. Computation of Trailing-Edge Flow and Noise Using Large-Eddy Simulation. *AIAA Journal*, 38(12):2201 – 2209, 2000.
- [82] J. E. Ffowcs Williams and D. L. Hawkings. Sound Generation by Turbulence and Surfaces in Arbitrary Motion. *Philosophical Transactions of the Royal Society, Series A*, 264:321 – 342, 1969.
- [83] Y. Xue and A. S. Lyrintzis. Rotating Kirchhoff Method for Three-Dimensional Transonic Blade-Vortex Interaction Hover Noise. *AIAA Journal*, 32(7):1350 – 1359, 1994.
- [84] X. Zhang. Computation of Sound Radiation of an Exhaust Duck. *6th CEAS-ASC Workshop "From CFD to CAA"*, Athen Greece, Nov., 2002.

Appendix A

Analytical Solutions for the Verifications

A.1 Governing Equation

Some unsteady non-viscous irrotational homentropic flows of an ideal gas are chosen as the verification examples.

Under the condition of irrotational flow, the velocity potential, Φ , exists:

$$\nabla \times \vec{u} = 0 \quad (\text{A.1})$$

$$\vec{u} = \nabla \Phi \quad (\text{A.2})$$

With the velocity potential the compressible continuity equation can be written as:

$$\frac{\partial \rho}{\partial t} + \nabla \Phi \cdot \nabla \rho + \rho \nabla^2 \Phi = 0 \quad (\text{A.3})$$

where ρ is the fluid density.

The momentum equation of the non-viscous flow can also be expressed in CROCCO's form:

$$\frac{\partial \vec{u}}{\partial t} + \frac{1}{2} \nabla (\vec{u} \cdot \vec{u}) = -(\nabla \times \vec{u}) \times \vec{u} - \frac{1}{\rho} \nabla p \quad (\text{A.4})$$

where p is the static pressure.

For the irrotational potential flow, the above equation A.4 can be transformed into:

$$\nabla Q = -\frac{1}{\rho} \nabla p \quad (\text{A.5})$$

where the auxiliary quantity, Q , is defined as:

$$Q = \frac{\partial \Phi}{\partial t} + \frac{1}{2} |\nabla \Phi|^2 \quad (\text{A.6})$$

The integration of the above equation A.5 from the local position to the undisturbed far-field yields:

$$Q_0 - Q = - \int_p^{p_0} \frac{dp}{\rho} \quad (\text{A.7})$$

The flow is homentropic and the medium is an ideal gas, hence:

$$\frac{p}{p_0} = \left(\frac{\rho}{\rho_0} \right)^\gamma \quad (\text{A.8})$$

where p_0 and ρ_0 are the static pressure and density in the undisturbed far field.

Assuming, in the undisturbed far-field, the velocity potential, $\Phi \equiv 0$, equation A.7 can be transformed into:

$$Q = \frac{\gamma}{\gamma - 1} \frac{p_0}{\rho_0} - \frac{\gamma}{\gamma - 1} \frac{p}{\rho} \quad (\text{A.9})$$

Introducing the sound speed equation in the homentropic ideal gas:

$$c^2 = \gamma \frac{p}{\rho} \quad (\text{A.10})$$

Equation A.9 can be presented as:

$$Q = \frac{c_0^2}{\gamma - 1} - \frac{c^2}{\gamma - 1} \quad (\text{A.11})$$

where c is the local sound speed, and c_0 is the sound speed in the undisturbed far-field, which is usually a constant. Equation A.11 is a formation of BERNOULLI's equation for the non-viscous and irrotational fluid field, which is often used to derive the analytical solution of aeroacoustic problems.

Through the operations of $\frac{\partial}{\partial t}$ and ∇ on the two sides of equation A.11, $\frac{1}{\rho} \frac{\partial \rho}{\partial t}$ and $\frac{1}{\rho} \nabla \rho$ can be calculated with Q and c :

$$\frac{\partial Q}{\partial t} = - \frac{c^2}{\rho} \frac{\partial \rho}{\partial t} \quad (\text{A.12})$$

$$\nabla Q = - \frac{c^2}{\rho} \nabla \rho \quad (\text{A.13})$$

Using equations A.12, A.13 and A.9, the terms of the density, ρ , in the continuity equation A.3 can be substituted with the terms of Q and c_0 . Hence:

$$\left[c_0^2 - (\gamma - 1) Q \right] \nabla^2 \Phi = \frac{\partial Q}{\partial t} + \nabla \Phi \cdot \nabla Q \quad (\text{A.14})$$

In equation A.14 there is only one unknown – the velocity potential, Φ . This is a closed equation. If the unsteady velocity potential, Φ , in this equation can be calculated under

certain initial and boundary conditions, the unsteady distributions of pressure and density can also be calculated through the following relationships:

$$p = p_0 \left(1 - \frac{\gamma - 1}{\gamma} \frac{\rho_0}{p_0} Q \right)^{\frac{\gamma}{\gamma - 1}} \quad (\text{A.15})$$

$$\rho \approx \gamma \frac{p}{c_0^2} \quad (\text{A.16})$$

where an approximation is made that the thermal conducts are negligible. The local sound speed is approximately equal to the sound speed in the undisturbed far-field.

At the observation position in the far-field, equation A.15 can be usually simplified as:

$$p - p_0 \approx \rho_0 \frac{\partial \Phi}{\partial t} \quad (\text{A.17})$$

because the acoustic fluctuations in the far-field are so small that the first term of the Taylor development of the perturbation against the mean value is already accurate enough.

Therefore, equation A.14 is the key to solve the problem. But this equation is still a non-linear equation which is difficult to solve. Fortunately, for the subsonic flow, the non-linear terms produce only the near-field pressure fluctuations, namely pseudo-sound, which cannot propagate to the far-field. Through dimensional and multiscale analysis, this equation can be linearized, then the analytical solutions can be derived for both the near and far field. The dimensionless form of equation A.14 is required. The dimensionless variables are introduced as the following:

$$\begin{aligned} x_i^* &:= \frac{x_i}{L}, \quad t^* := \frac{tU_0}{L}, \\ \Phi^* &:= \frac{\Phi}{U_0 L}, \quad Q^* := \frac{Q}{U_0}, \\ M_a &:= \frac{U_0}{c_0} \end{aligned} \quad (\text{A.18})$$

where L and U_0 are the characteristic length and velocity of the fluid field. Then the dimensionless form can be written as:

$$\left(1 - (\gamma - 1)M_a^2 Q^* \right) \nabla^{*2} \phi^* = M_a^2 \left(\frac{\partial Q^*}{\partial t^*} + \nabla^* \phi^* \cdot \nabla^* Q^* \right) \quad (\text{A.19})$$

In the following parts of this chapter, equation A.19 will be solved under the different boundary conditions to derive the appropriate analytical solutions for the verification examples.

A.2 3D Mono-, Di- and Quadrupole

In Figure A.1(a) of page 110, the simulated 3D monopolar source is sketched. The source is a sphere with radius, a , which is pulsating in the radial direction with a velocity of $U_n \cos(\omega t)$. One way to simulate a 3D dipolar source is to consider this source as a superposition of two nearby 3D monopolar sources. In Figure A.1(b) of page 110, the simulated 3D dipolar source is sketched. The source is a superposition of two nearby spheres with radius, a , one of which is pulsating in the radial direction with a velocity of $U_n \cos(\omega t)$ and the other of which, $-U_n \cos(\omega t)$. The distance between the centers of two monopolar sources is d . Similarly, a quadrupolar source is equivalent to two nearby dipoles or four nearby monopolar sources. In Figure A.1(c) of page 110, the simulated lateral quadrupolar source is sketched. The source is a superposition of four nearby spheres with radius, a , each of which is pulsating in the radial direction with a equal velocity magnitude of $|U_n \cos(\omega t)|$ and an opposite phase compared with the directly adjacent sphere. The distance between the centers of directly adjacent spheres is also d .

According to the aeroacoustic analogy theory, the compact aerodynamical sound source region can be treated as a distribution of point monopoles, dipoles and quadrupoles. The analytical solutions of 3D mono-, di-, and quadrupoles are shown as follows:

One Fluctuating Spherical Surface (3D Monopolar Source):

The particle velocity field is:

$$u(\vec{y}, t) = u_r(r, t) \frac{y_1}{r} \quad (\text{A.20})$$

$$v(\vec{y}, t) = u_r(r, t) \frac{y_2}{r} \quad (\text{A.21})$$

$$w(\vec{y}, t) = u_r(r, t) \frac{y_3}{r} \quad (\text{A.22})$$

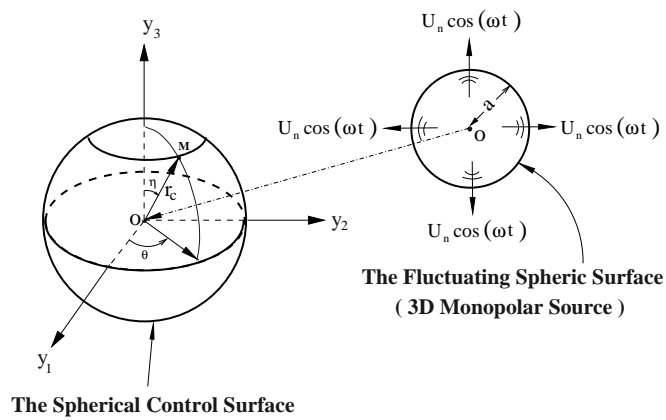
The sound pressure field is:

$$p'(\vec{y}, t) = \frac{Q\rho_\infty\omega}{4\pi r} \frac{1}{\sqrt{1+(ka)^2}} \cos[\omega t - k(r-a) + \varphi_0] \quad (\text{A.23})$$

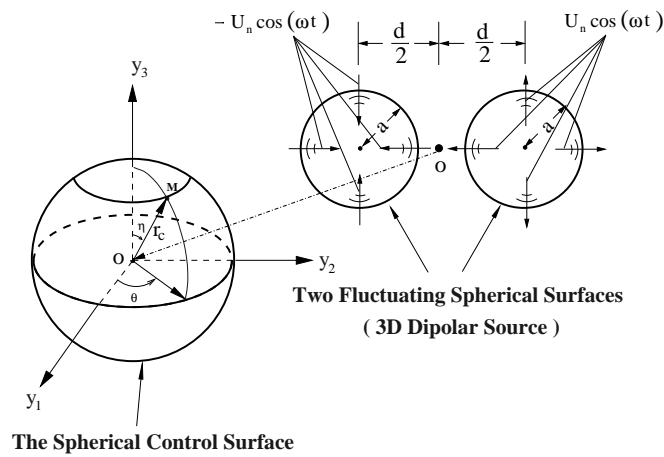
And in the above equations:

$$u_r(r, t) = \frac{1}{\sqrt{1+(ka)^2}} \left\{ \frac{kQ}{4\pi r} \cos[\omega t - k(r-a) + \varphi_0] + \frac{Q}{4\pi r^2} \sin[\omega t - k(r-a) + \varphi_0] \right\} \quad (\text{A.24})$$

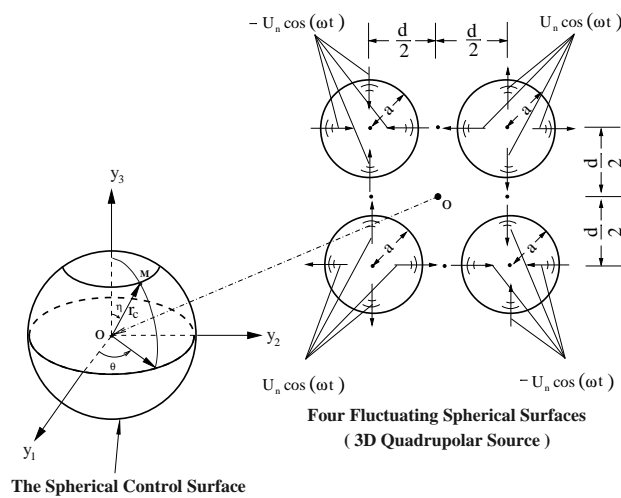
$$Q = 4\pi a^2 U_n \quad , \quad \varphi_0 = \arctan\left(\frac{1}{ka}\right) \quad , \quad r = \sqrt{y_1^2 + y_2^2 + y_3^2} \quad (\text{A.25})$$



(a) 3D Monopolar Source and Control Surface



(b) 3D Dipolar Source and Control Surface



(c) 3D Quadrupolar Source and Control Surface

Figure A.1: 3D Simple Sources and Control Surfaces

Two Fluctuating Spherical Surfaces (3D Dipolar Source):

The particle velocity field is:

$$u(\vec{y}, t) = -u_r(r_1, t) \frac{y_1 + 0.5d}{r_1} + u_r(r_2, t) \frac{y_1 - 0.5d}{r_2} \quad (\text{A.26})$$

$$v(\vec{y}, t) = -u_r(r_1, t) \frac{y_2}{r_1} + u_r(r_2, t) \frac{y_2}{r_2} \quad (\text{A.27})$$

$$w(\vec{y}, t) = -u_r(r_1, t) \frac{y_3}{r_1} + u_r(r_2, t) \frac{y_3}{r_2} \quad (\text{A.28})$$

The sound pressure field is:

$$\begin{aligned} p'(\vec{y}, t) &= -\frac{Q\rho_0\omega}{4\pi r_1} \frac{1}{\sqrt{1+(ka)^2}} \cos[\omega t - k(r_1 - a) + \varphi_0] \\ &\quad + \frac{Q\rho_0\omega}{4\pi r_2} \frac{1}{\sqrt{1+(ka)^2}} \cos[\omega t - k(r_2 - a) + \varphi_0] \end{aligned} \quad (\text{A.29})$$

And in the above equations:

$$r_1 = \sqrt{(y_1 + 0.5d)^2 + y_2^2 + y_3^2}, \quad r_2 = \sqrt{(y_1 - 0.5d)^2 + y_2^2 + y_3^2} \quad (\text{A.30})$$

Four Fluctuating Spherical Surfaces (3D Quadrupolar Source):

The particle velocity field is:

$$\begin{aligned} u(\vec{y}, t) &= -u_r(r_1, t) \frac{y_1 + 0.5d}{r_1} + u_r(r_2, t) \frac{y_1 - 0.5d}{r_2} \\ &\quad - u_r(r_3, t) \frac{y_1 - 0.5d}{r_3} + u_r(r_4, t) \frac{y_1 + 0.5d}{r_4} \end{aligned} \quad (\text{A.31})$$

$$\begin{aligned} v(\vec{y}, t) &= -u_r(r_1, t) \frac{y_2 - 0.5d}{r_1} + u_r(r_2, t) \frac{y_2 - 0.5d}{r_2} \\ &\quad - u_r(r_3, t) \frac{y_2 + 0.5d}{r_3} + u_r(r_4, t) \frac{y_2 + 0.5d}{r_4} \end{aligned} \quad (\text{A.32})$$

$$\begin{aligned} w(\vec{y}, t) &= -u_r(r_1, t) \frac{y_3}{r_1} + u_r(r_2, t) \frac{y_3}{r_2} \\ &\quad - u_r(r_3, t) \frac{y_3}{r_3} + u_r(r_4, t) \frac{y_3}{r_4} \end{aligned} \quad (\text{A.33})$$

The sound pressure field is:

$$\begin{aligned}
p'(\vec{y}, t) = & -\frac{Q\rho_0\omega}{4\pi r_1} \frac{1}{\sqrt{1+(ka)^2}} \cos[\omega t - k(r_1 - a) + \varphi_0] \\
& + \frac{Q\rho_0\omega}{4\pi r_2} \frac{1}{\sqrt{1+(ka)^2}} \cos[\omega t - k(r_2 - a) + \varphi_0] \\
& - \frac{Q\rho_0\omega}{4\pi r_3} \frac{1}{\sqrt{1+(ka)^2}} \cos[\omega t - k(r_3 - a) + \varphi_0] \\
& + \frac{Q\rho_0\omega}{4\pi r_4} \frac{1}{\sqrt{1+(ka)^2}} \cos[\omega t - k(r_4 - a) + \varphi_0]
\end{aligned} \tag{A.34}$$

And in the above equations:

$$\begin{aligned}
r_1 &= \sqrt{(y_1 + 0.5d)^2 + (y_2 - 0.5d)^2 + y_3^2} \\
r_2 &= \sqrt{(y_1 - 0.5d)^2 + (y_2 - 0.5d)^2 + y_3^2} \\
r_3 &= \sqrt{(y_1 - 0.5d)^2 + (y_2 + 0.5d)^2 + y_3^2} \\
r_4 &= \sqrt{(y_1 + 0.5d)^2 + (y_2 + 0.5d)^2 + y_3^2}
\end{aligned} \tag{A.35}$$

A.3 2D Mono- and Dipole

In figure A.2(a) of page 113, the simulated 2D monopolar source is sketched. The source is a circular cylinder with radius, a , which is pulsating in the radial direction with a velocity of $U_n \cos(\omega t)$. In figure A.2(b) of page 113, the simulated 2D dipolar source is sketched. The source is a circular cylinder with radius, a , which is oscillating with the entirety of the body in the x-direction with a velocity of $U_n \cos(\omega t)$.

One Fluctuating Cylindrical Surface (2D Monopolar Source):

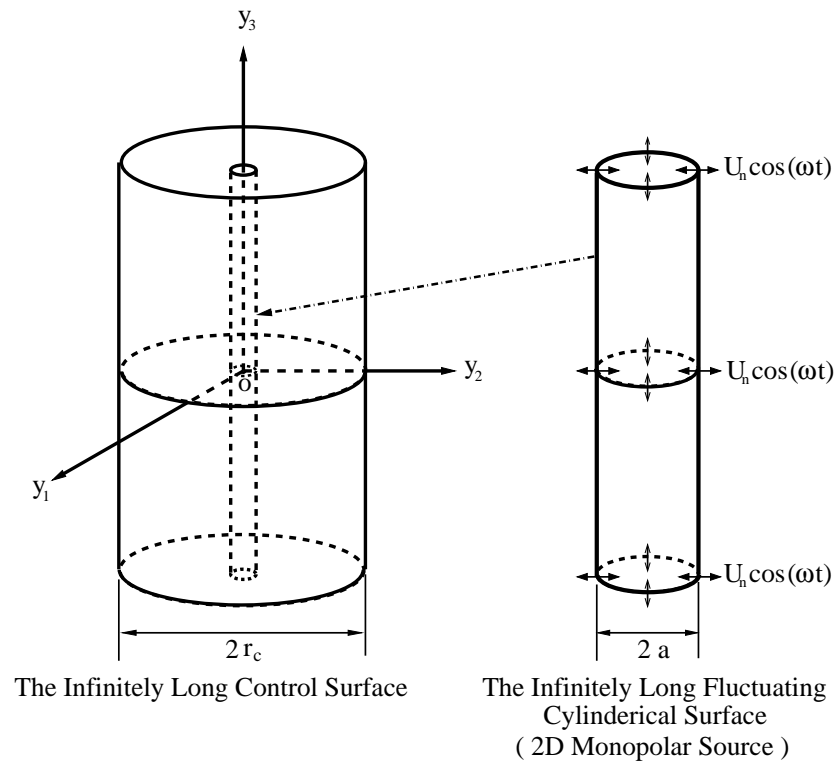
The particle velocity field is :

$$u(\vec{y}, t) = u_r(r, t) \frac{y_1}{r} \tag{A.36}$$

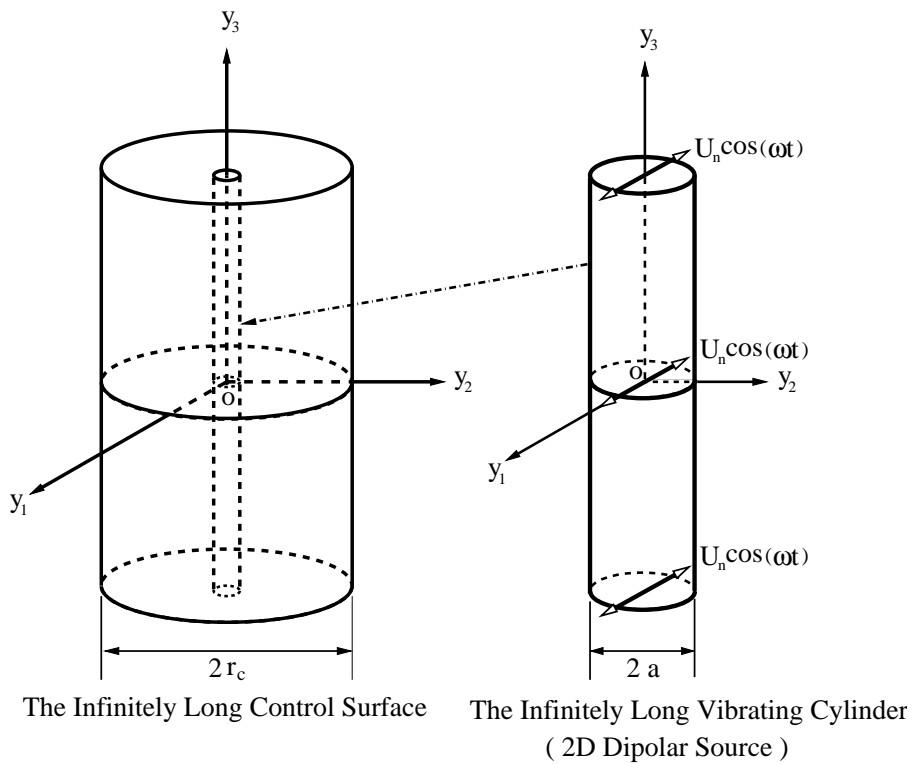
$$v(\vec{y}, t) = u_r(r, t) \frac{y_2}{r} \tag{A.37}$$

The sound pressure field is :

$$p'(\vec{y}, t) = \rho_\infty c_\infty \frac{U_n}{H_1^{(2)}(ka)} H_0^{(2)}(kr) \exp \left[i \left(\omega t + \frac{\pi}{2} \right) \right] \tag{A.38}$$



(a) 2D Monopolar Source and Control Surface



(b) 2D Dipolar Source and Control Surface

Figure A.2: 2D Simple Sources and Control Surfaces

And in the above equations :

$$u_r(r, t) = \frac{U_n}{H_1^{(2)}(ka)} H_1^{(2)}(kr) \exp(i\omega t) \quad (\text{A.39})$$

$$r = \sqrt{y_1^2 + y_2^2} \quad (\text{A.40})$$

The term $H_0^{(2)}$ denotes the zeroth-order second type of HANKEL function, and $H_1^{(2)}$ denotes the first-order second type of HANKEL function.

One Oscillating Cylinder (2D Dipolar Source):

The particle velocity field is :

$$u(\vec{y}, t) = u_r(r, t) \frac{y_1}{r} + u_\theta(r, t) \frac{y_2}{r} \quad (\text{A.41})$$

$$v(\vec{y}, t) = u_r(r, t) \frac{y_2}{r} - u_\theta(r, t) \frac{y_1}{r} \quad (\text{A.42})$$

The sound pressure field is :

$$p'(\vec{y}, t) = \rho_\infty c_\infty \frac{U_n \exp\left[i\left(\omega t - \frac{\pi}{2}\right)\right]}{H_0^{(2)}(ka) - \frac{1}{ka} H_1^{(2)}(ka)} H_1^{(2)}(kr) \frac{y_1}{r} \quad (\text{A.43})$$

And in the above equations :

$$u_r(r, t) = \frac{U_n \exp(i\omega t)}{H_0^{(2)}(ka) - \frac{1}{ka} H_1^{(2)}(ka)} \left[H_0^{(2)}(kr) - \frac{1}{kr} H_1^{(2)}(kr) \right] \frac{y_1}{r} \quad (\text{A.44})$$

$$u_\theta(r, t) = -\frac{U_n \exp(i\omega t)}{H_0^{(2)}(ka) - \frac{1}{ka} H_1^{(2)}(ka)} \frac{1}{kr} H_1^{(2)}(kr) \frac{y_2}{r} \quad (\text{A.45})$$

$$r = \sqrt{y_1^2 + y_2^2} \quad (\text{A.46})$$

The term $H_0^{(2)}$ denotes the zeroth-order second type of HANKEL function, and $H_1^{(2)}$ denotes the first-order second type of HANKEL function.

A.4 Co-rotating Line Vortices

In figure A.3, the simulated aeroacoustic source of co-rotating line vortices is sketched. The sound field of these co-rotating line vortices is used to verify the aeroacoustic solver, to check if the code allows the true sound propagation to the far field and correctly filters out

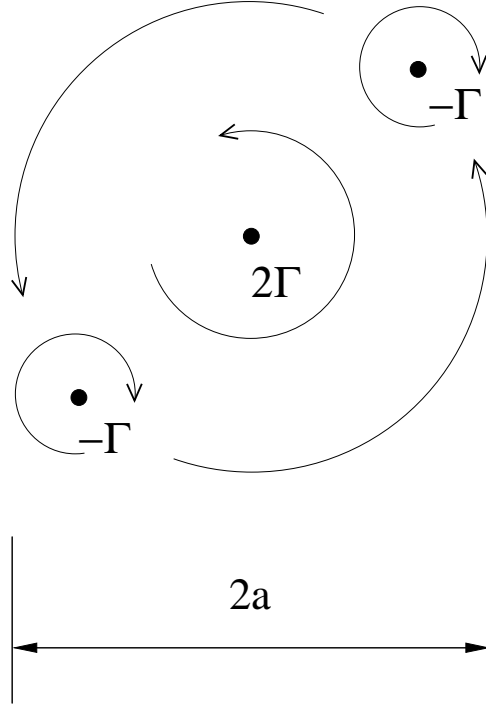


Figure A.3: Co-rotating Vortices

the part of the dynamical fluctuation which does not radiate as true sound to the far field.

The analytical dimensionless solutions of the dynamical near-field ($\sqrt{y_1^2 + y_2^2} \sim a$) of the co-rotating vortices are:

$$u^* = -\frac{\sin \theta^* + r^{*2} \sin(\frac{3t^*}{2\pi} - 3\theta^*)}{\pi r^* [r^{*4} + 1 - 2r^{*2} \cos(\frac{3t^*}{2\pi} - 2\theta^*)]} \quad (\text{A.47})$$

$$v^* = \frac{\cos \theta^* - r^{*2} \cos(\frac{3t^*}{2\pi} - 3\theta^*)}{\pi r^* [r^{*4} + 1 - 2r^{*2} \cos(\frac{3t^*}{2\pi} - 2\theta^*)]} \quad (\text{A.48})$$

$$u^* = \frac{a}{\Gamma} u, \quad v^* = \frac{a}{\Gamma} v \quad (\text{A.49})$$

$$r^* = \frac{r}{a}, \quad t^* = \frac{t\Gamma}{a^2}, \quad \theta^* = \theta \quad (\text{A.50})$$

The asymptotic solution of the acoustic far-field ($\sqrt{y_1^2 + y_2^2} \sim a^2 c_0 / \Gamma$) of the co-rotating vortices is:

$$p'(\vec{x}, t) = -\frac{\rho_\infty \Omega \Gamma M^{3/2}}{2} \left(\frac{a}{\pi r}\right)^{1/2} \sin \left[\Omega \left(t - \frac{r}{c_\infty} \right) - 2\theta + \frac{\pi}{4} \right] \quad (\text{A.51})$$

$$\Omega = \frac{3\Gamma}{2\pi a^2} \quad (\text{A.52})$$

$$M = \frac{\Omega a}{2c_\infty} \quad (\text{A.53})$$

A.5 2D Monopole in Flow

A monopolar line source, placed in a uniform flow, is located at the origin of the reference frame; and the uniform flow is in the +x direction. The complex potential for this 2D monopole is given by DOWLING and FLOWCS-WILLIAMS [17] as:

$$\phi(x, y, t) = A \frac{i}{4\beta} e^{i(\omega t + M k x / \beta^2)} H_0^{(2)} \left(\frac{k}{\beta^2} \sqrt{x^2 + \beta^2 y^2} \right) \quad (\text{A.54})$$

where $\beta = \sqrt{1 - M^2}$ and $M = U_0/c_0$. The particle velocities, pressure and density fluctuations needed in the FW-H approach are obtained from the real parts of $p' = p - p_0 = -\rho_0 \left(\frac{\partial \phi}{\partial t} + U_0 \frac{\partial \phi}{\partial x} \right)$, $u = U_0 + \frac{\partial \phi}{\partial x}$, $v = \frac{\partial \phi}{\partial y}$, and $p - p_0 = c_0^2 (\rho - \rho_0)$. U_0 is the velocity of the mean flow.

Therefore:

$$u = U_0 - \text{Re} \left\{ \left[\frac{M}{\beta} H_0^{(2)}(r_\beta) + i \frac{x}{r_\beta} H_1^{(2)}(r_\beta) \right] \cdot \frac{Ak}{4\beta^2} e^{i(\omega t + M k x / \beta^2)} \right\} \quad (\text{A.55})$$

$$v = -\text{Re} \left\{ i \frac{y}{r_\beta} H_1^{(2)}(r_\beta) \frac{Ak}{4} e^{i(\omega t + M k x / \beta^2)} \right\} \quad (\text{A.56})$$

$$p - p_0 = \text{Re} \left\{ \left[\frac{1}{\beta} H_0^{(2)}(r_\beta) + i \frac{Mx}{r_\beta} H_1^{(2)}(r_\beta) \right] \cdot \frac{\rho_0 c_0 Ak}{4\beta^2} e^{i(\omega t + M k x / \beta^2)} \right\} \quad (\text{A.57})$$

$$r_\beta = x^2 + \beta^2 y^2 \quad (\text{A.58})$$

where $H_k^{(n)}$ denotes a HANKEL function of the nth kind and the kth order.